

Medical Physics Unit  
McGill University

Monte Carlo modeling of the Varian TrueBeam linear  
accelerator, with chamber effects included in determination  
of the source parameters

M.Sc. Thesis  
Kyle O'Grady

*A Thesis submitted to the Faculty of Graduate Studies and Research in partial fulfillment of  
the requirements for the degree of Master of Science in Medical Radiation Physics*

April 2016

# Contents

<b>Abstract</b>	<b>ix</b>
<b>Résumé</b>	<b>x</b>
<b>Acknowledgements</b>	<b>xi</b>
<b>Chapter 1</b>	<b>1</b>
<b>Introduction</b> .....	<b>1</b>
1.1 Radiotherapy.....	1
1.2 Monte Carlo in radiotherapy .....	2
1.2.1 Constructing a Monte Carlo beam model .....	3
1.2.2 Phase spaces .....	4
1.3 Varian’s TrueBeam phase space solution .....	5
1.4 Disadvantages of TrueBeam phase spaces.....	6
1.5 TrueBeam models: FakeBeam and FalseBEAM.....	10
1.5.1 FakeBeam.....	11
1.5.2 FalseBEAM.....	13
1.6 Thesis outline .....	13
<b>Chapter 2</b>	<b>15</b>
<b>Detector effects in linear accelerator Monte Carlo simulations</b> .....	<b>15</b>
2.1 <i>egs_chamber</i> simulations.....	17
2.1.1 Variance reduction techniques in <i>egs_chamber</i> .....	17
2.1.2 Depth dose and profile calculations .....	18
2.2 Ionization chamber perturbations.....	19
2.2.1 Chamber material perturbations.....	19
2.2.2 Volume averaging perturbations.....	22
2.3 Diode and synthetic diamond detector perturbation effects .....	24
2.4 Summary of Chapter 2.....	24
<b>Chapter 3</b>	<b>26</b>
<b>Commissioning the source parameters of a Varian CL21EX Monte Carlo beam model</b> .....	<b>26</b>
3.1 Ionization chamber measurements.....	27

3.2 BEAMnrc simulations .....	30
3.2.1 Variance reduction techniques in BEAMnrc .....	31
3.2.2 Incident electron energy.....	31
3.2.3 Spot size .....	33
3.2.4 Angular spread.....	35
3.2.5 Validation of the tuned 6 MV CL21EX model using air-filled ionization chambers...	39
3.3 The final tuned 6 MV CL21EX model.....	43
<b>Chapter 4</b>	<b>44</b>
<b>Materials and methods for modeling the Varian TrueBeam.....</b>	<b>44</b>
4.1 FakeBeam: reproducing the work by Rodriguez et al. in BEAMnrc .....	44
4.2 Analyzing phase spaces with BEAMDP .....	46
4.3 FalseBEAM.....	46
4.3.1 Dose to water calculations including detector models.....	48
4.3.2 Water tank measurements for 6 MV FFF .....	49
<b>Chapter 5</b>	<b>51</b>
<b>Results from Varian TrueBeam models.....</b>	<b>51</b>
5.1 FakeBeam.....	51
5.2 FalseBEAM: phase space matching.....	56
5.3 FalseBEAM: dose to water calculations .....	60
5.3.1 Agreement of the untuned FalseBEAM model with TrueBeam representative data	60
5.3.2 FalseBEAM model tuning simulations benchmarked by PTW.....	61
microDiamond measurements .....	61
5.3.3 Validation of tuned FalseBEAM with in-house CC13 measurements .....	66
5.3.4 The final tuned FalseBEAM model .....	70
<b>Chapter 6</b>	<b>72</b>
<b>Conclusion .....</b>	<b>72</b>

# List of figures

Figure 1.1: The effect of varying a) FWHM of the focal spot size and b) the incident electron energy on profiles of a 40 x 40 cm <sup>2</sup> . Reproduced from Faddegon et al. with permission [5].	3
Figure 1.2: Illustration of the components of a typical Varian linear accelerator treatment head in photon beam mode. Phase space planes for simulating patient-dependent and patient-independent structures are also represented. Reproduced from Chetty et al. with permission [2].	5
Figure 1.3: Varian IAEA phase space plane	7
Figure 1.4: Varian VirtuaLinac interface. Printed with Varian's permission.	7
Figure 1.5: a) Unnormalized and b) normalized fluence profiles comparing TrueBeam phase spaces released by Varian (generic) and generated on the VirtuaLinac with the same source parameters. The VirtuaLinac phase space was generated with a newer Geant4 version and physics list, as recommended by Varian. Phase spaces were scored above the linac jaws.	8
Figure 1.6: BEAMnrc/DOSXYZnrc simulation components	10
Figure 1.7: PENELOPE Varian Clinac series model. Reproduced from the PRIMO user manual with permission [31].	11
Figure 1.8: FakeBeam bronze 6 MV FFF filter in centimetres. Reproduced from Rodriguez et al. with permission [30].	11
Figure 1.9: Rodriguez et al.'s comparison of measurements (dots) to Monte Carlo calculated FakeBeam and TrueBeam phase space (lines) PDDs. The percent difference is relative to the maximum dose. Statistical uncertainties are in the range of 0.3 to 0.8%. Reproduced from Rodriguez et al. with permission [30].	12
Figure 1.10: Rodriguez et al.'s comparison of measurements (dots) to Monte Carlo calculated FakeBeam and TrueBeam phase space (lines) profiles at 5 cm depth. The percent difference curves of FakeBeam (black) and TrueBeam (gray) are relative to the maximum dose. Statistical uncertainties are in the range of 0.3 to 0.8%. Reproduced from Rodriguez et al. with permission [30].	12
Figure 2.1: Chamber model cross sections created in egs_view of a) the PTW microLion liquid ionization chamber, b) the Exradin A1SL air-filled ionization chamber, and c) the Exradin A12 air-filled ionization chamber. The nominal cavity radius, $r_{cav}$ , is included for each chamber. All displayed component dimensions in this figure were modified to protect the confidentiality of the chamber designs. The chamber stem of the Exradin models is not displayed in the figure, but was included in the A1SL and A12 models.	16
Figure 2.2: BEAMnrc/egs_chamber shared library simulation	17
Figure 2.3: Exradin A12 at 1 cm depth with an air/water XCSE shell	19
Figure 2.4: Correlated sampling was used to calculate dose ratio profiles comparing a full ionization chamber model to the same chamber model with all components made up of water. Cavity geometries were identical to exclude the volume averaging effect. The A1SL chamber component dimensions in this figure were modified to protect the	

confidentiality of the chamber design. The chamber stem is not displayed in the figure, but was included in the A1SL model. ....	20
Figure 2.5: Dose ratio profile of a 5 x 5 cm <sup>2</sup> 18 MV beam using the PTW microLion liquid ion chamber demonstrating the chamber material perturbation effect .....	21
Figure 2.6: Dose ratio profile of a 5 x 5 cm <sup>2</sup> 18 MV beam using the Exradin A1SL air-filled ion chamber demonstrating the chamber material perturbation effect.....	21
Figure 2.7: Correlated sampling was used to calculate dose ratio profiles comparing a full ionization chamber model to a 0.3 x 0.3 x 1.0 mm <sup>3</sup> water voxel. The chamber component dimensions of the PTW microLion in this figure were modified to protect the confidentiality of the chamber design.....	22
Figure 2.8: Volume averaging effect of the Exradin A12 farmer chamber profile scanned length-wise shows significant blurring of the penumbra when compared to a 0.3 mm long water voxel. ....	23
Figure 2.9: Volume averaging effect of the PTW microLion liquid ion chamber profile compared to a 0.3 mm long water voxel.....	23
Figure 3.1: Comparisons of microLion data obtained with +400 V and +800 V potentials before and after ion recombination corrections in an 18 MV beam for a),b) 10 x 10 cm <sup>2</sup> PDDs and c),d) 30 x 30 cm <sup>2</sup> profiles at 10 cm depth .....	29
Figure 3.2: PDD comparison between the default and tuned energies of 6.3 MeV and 5.9 MeV, respectively, for a)-b) 5 x 5 cm <sup>2</sup> , c)-d) 10 x 10 cm <sup>2</sup> and e)-f) 30 x 30 cm <sup>2</sup> fields...	32
Figure 3.3: Cross-plane 5 x 5 cm <sup>2</sup> microLion measured and microLion calculated profile comparisons at 10 cm depth for a) default and b) tuned spot sizes along x.....	34
Figure 3.4: In-plane 5 x 5 cm <sup>2</sup> microLion measured and microLion calculated profile comparisons at 10 cm depth for a) default and b) tuned spot sizes along y.....	34
Figure 3.5: In-plane 30 x 30 cm <sup>2</sup> microLion measured and microLion calculated profile comparisons at 10 cm depth for a) default and b) tuned angular spread.....	37
Figure 3.6: Cross-plane 30 x 30 cm <sup>2</sup> microLion measured and microLion calculated profile comparisons at 10 cm depth for a) default and b) tuned angular spread.....	37
Figure 3.7: Comparison between calculated and measured 5 x 5 cm <sup>2</sup> PDDs for the a) Exradin A1SL and b) Exradin A12 air-filled ionization chambers.....	39
Figure 3.8: Comparison between calculated and measured 5 x 5 cm <sup>2</sup> a)-b) cross-plane and c)-d) in-plane profiles for the Exradin A1SL and Exradin A12 air-filled ionization chambers. ....	40
Figure 3.9: Comparison between calculated and measured 30 x 30 cm <sup>2</sup> a) cross-plane and b) in-plane profiles for the Exradin A1SL air-filled ionization chamber. ....	42
Figure 5.1: An egs_chamber CC13 simulation of a 10 x 10 cm <sup>2</sup> profile at 10 cm depth, using the BEAMnrc FakeBeam model. Differences in fluence between implementations of FakeBeam propagates to a discrepancy in dose to water. ....	52
Figure 5.2: Comparison of a) unnormalized and b) normalized phase space fluence above the jaws between the EGSnrc and PENELOPE implementations of FakeBeam, in addition to the generic Varian TrueBeam Geant4 phase space.....	52
Figure 5.3: Comparison of phase space fluence above the jaws between the PENELOPE FakeBeam model simulated using the recommended detailed transport parameters C1=C2=0.001 and the less detailed C1=C2=0.1 in the target, plotted alongside the BEAMnrc implementation of FakeBeam.....	53

Figure 5.4: Comparison of phase space fluence above the jaws between the BEAMnrc FakeBeam model simulated with default transport parameters and in single-scattering mode, plotted alongside the PENELOPE implementation of FakeBeam with transport parameters $C1=C2=0.001$ .....	54
Figure 5.5: Comparison of radial dose profiles at 1.5 cm depth for as PENELOPE transport parameters C1 and C2 were varied, and for various EGSnrc transport parameters. IF stands for interaction forcing. PENELOPE simulation data was reproduced from the work by Rodriguez et al. [37] with permission. ....	56
Figure 5.6: FalseBEAM model in BEAMnrc. The dimensions in the figure are no to scale....	57
Figure 5.7: FalseBEAM vs. TrueBeam comparison of phase space a) unnormalized and b) normalized fluence, relative to approximately 3 cm radial off-axis distance, above the jaws. ....	58
Figure 5.8: FalseBEAM vs. TrueBeam comparison of normalized phase space spectra, relative to the maximum fluence, above the jaws from 0 MeV to 6 MeV. The dimensions in the FalseBEAM figure are not to scale. ....	58
Figure 5.9: FalseBEAM vs. TrueBeam comparison of normalized phase space spectra, relative to the fluence at 1 MeV, above the jaws from 0 MeV to 1 MeV. The dimensions in the FalseBEAM figure are not to scale. ....	59
Figure 5.10: Comparison between a calculated and measured 10 x 10 cm <sup>2</sup> a) PDD and b) profile at 10 cm depth using the FalseBEAM model for the IBA CC13 TrueBeam representative data. ....	60
Figure 5.11: PDD comparison for 5 x 5 cm <sup>2</sup> fields with a tuned FalseBEAM incident electron energy of 5.8 MeV against microDiamond measurements. A microDiamond model was including in the dose to water calculation. ....	61
Figure 5.12: PDD comparison for a) 10 x 10 cm <sup>2</sup> and b) 30 x 30 cm <sup>2</sup> fields with a tuned FalseBEAM incident electron energy of 5.8 MeV against microDiamond measurements. A microDiamond model was including in the dose to water calculation. ....	62
Figure 5.13: Tuned comparison of a) cross-plane and b) in-plane 5 x 5 cm <sup>2</sup> microDiamond measured and microDiamond calculated profiles at 10 cm depth for FalseBEAM with a tuned spot size FWHM of (1.31 mm, 1.21 mm). ....	62
Figure 5.14: Tuned comparison of a) cross-plane and b) in-plane 30 x 30 cm <sup>2</sup> microDiamond measured and microDiamond calculated profiles at 10 cm depth for FalseBEAM with a tuned angular spread.....	64
Figure 5.15: 5 x 5 cm <sup>2</sup> PDD comparison of measured CC13 data with a tuned FalseBEAM simulation that includes a CC13 model. ....	66
Figure 5.16: 5 x 5 cm <sup>2</sup> a) cross-plane and b) in-plane profile comparison at 10 cm depth of measured CC13 data with a tuned FalseBEAM simulation that includes a CC13 model.....	67
Figure 5.17: 30 x 30 cm <sup>2</sup> a) cross-plane and b) in-plane profile comparison at 10 cm depth of measured CC13 data with a tuned FalseBEAM simulation that includes a CC13 model...68	68

# List of tables

Table 1: The maximum percent local difference in each region of 5 x 5 cm <sup>2</sup> profiles at 10 cm depth, with a default spot size of (0.05 cm, 0 cm) and tuned spot size (0.125 cm, 0.10 cm).....	36
Table 2: The average absolute local percent difference in each region of 5 x 5 cm <sup>2</sup> profiles at 10 cm depth, with a default spot size of (0.05 cm, 0 cm) and tuned spot size (0.125 cm, 0.10 cm).....	36
Table 3: Distance-to-agreement in the penumbra region (90% to 20% off-axis ratio) of 5 x 5 cm <sup>2</sup> profiles at 10 cm depth, with a default spot size of (0.05 cm, 0 cm) and tuned spot size (0.125 cm, 0.10 cm). ....	36
Table 4: The maximum percent local difference in each region of 30 x 30 cm <sup>2</sup> profiles at 10 cm depth, with a default and tuned angular spread of 0.0° and 0.15°, respectively. ....	38
Table 5: The average absolute local percent difference in each region of 30 x 30 cm <sup>2</sup> profiles at 10 cm depth, with a default and tuned angular spread of 0.0° and 0.15°, respectively. ....	38
Table 6: Distance-to-agreement from 90% to 20% off-axis ratio of 30 x 30 cm <sup>2</sup> profiles at 10 cm depth, with a default and tuned angular spread of 0.0° and 0.15°, respectively. ....	38
Table 7: The maximum percent local difference in each region of 5 x 5 cm <sup>2</sup> profiles at 10 cm depth for the Exradin A1SL and Exradin A12 air-filled ionization chambers. ....	40
Table 8: The average absolute local percent difference in each region of 5 x 5 cm <sup>2</sup> profiles at 10 cm depth for the Exradin A1SL and Exradin A12 air-filled ionization chambers. ....	41
Table 9: Distance-to-agreement in the penumbra region (90% to 20% off-axis ratio) of 5 x 5 cm <sup>2</sup> and 30 x 30 cm <sup>2</sup> profiles at 10 cm depth for the Exradin A1SL and Exradin A12 air-filled ionization chambers.....	41
Table 10: The maximum percent local difference in each region of 30 x 30 cm <sup>2</sup> profiles at 10 cm depth for the Exradin A1SL air-filled ionization chamber.....	42
Table 11: The average absolute local percent difference in each region of 30 x 30 cm <sup>2</sup> profiles at 10 cm depth for the Exradin A1SL air-filled ionization chamber.....	42
Table 12: The maximum percent local difference in each region of 5 x 5 cm <sup>2</sup> profiles at 10 cm depth for the PTW microDiamond detector.....	63
Table 13: The mean absolute percent local difference in each region of 5 x 5 cm <sup>2</sup> profiles at 10 cm depth for the PTW microDiamond detector.....	63
Table 14: Distance-to-agreement in the penumbra region (90% to 20% off-axis ratio) of 5 x 5 cm <sup>2</sup> profiles at 10 cm depth for the PTW microDiamond detector.....	63
Table 15: The maximum percent local difference in each region of 30 x 30 cm <sup>2</sup> profiles at 10 cm depth for the PTW microDiamond detector.....	65
Table 16: The mean absolute local percent difference in each region of 30 x 30 cm <sup>2</sup> profiles at 10 cm depth for the PTW microDiamond detector.....	65
Table 17: Distance-to- agreement in the penumbra region (60% to 20% off-axis ratio) of 30 x 30 cm <sup>2</sup> profiles at 10 cm depth for the PTW microDiamond detector.....	65

Table 18: The maximum percent local difference in each region of 5 x 5 cm <sup>2</sup> profiles at 10 cm depth for the IBA CC13 air-filled ionization chamber.....	67
Table 19: The mean absolute local percent difference in each region of 5 x 5 cm <sup>2</sup> profiles at 10 cm depth for the IBA CC13 air-filled ionization chamber.....	67
Table 20: Distance-to-agreement in the penumbra region (90% to 20% off-axis ratio) of 5 x 5 cm <sup>2</sup> profiles at 10 cm depth for the IBA CC13 air-filled ionization chamber.....	68
Table 21: The maximum percent local difference in each region of 30 x 30 cm <sup>2</sup> profiles at 10 cm depth for the IBA CC13 ionization chamber. ....	69
Table 22: The mean absolute local percent difference in each region of 30 x 30 cm <sup>2</sup> profiles at 10 cm depth for the IBA CC13 ionization chamber.....	69
Table 23: Distance-to- agreement in the penumbra region (60% to 20% off-axis ratio) of 30 x 30 cm <sup>2</sup> profiles at 10 cm depth for the IBA CC13 ionization chamber.....	69

# Abstract

Varian has opted not to provide the physical details of their TrueBeam linear accelerator, which has historically been provided to researchers under non-disclosure agreements to construct accurate Monte Carlo beam models. One compromise has been to release Monte Carlo calculated phase space data above the linac jaws, with source parameters tuned to TrueBeam representative beam data. In addition, Varian has also developed a cloud-based VirtuaLinac web interface that allows for the generation of phase space data with customizable source parameters on a pay-as-you-go basis, without knowing the geometric details within the Geant4 model. The main disadvantages of Varian phase space sources are the efficiency and cost when compared to a full BEAMnrc/EGSnrc Monte Carlo beam model. Phase space sources can have massive storage requirements, their network and hard drive use can drastically slow down simulations, and the cost is not insignificant for detailed tuning of VirtuaLinac source parameters to in-house measurements.

FalseBEAM, an independent TrueBeam model for 6 MV flattening filter free (FFF) photon beams, has been constructed by modifying a previously commissioned 6 MV model of the Varian Clinac 21EX in BEAMnrc. Geometric dimensions and materials were matched in a trial and error approach to the photon/electron fluence and spectra of Varian phase space files. Once the in-house model phase space matched that of the Varian phase space with identical source parameters, the source parameters were tuned to match in-house water tank measurements obtained with the PTW microDiamond detector. In addition, a BEAMnrc implementation of a published PENELOPE TrueBeam model, FakeBeam, was investigated. Detector models were included in all dose to water simulations to include the effects of volume averaging and the non-water equivalence of the detector materials, which allowed for more accurate selection of beam model source parameters.

# Résumé

Varian a choisi de ne pas partager les détails physiques de leur accélérateur linéaire *TrueBeam*, qui étaient fournis traditionnellement aux chercheurs sous les ententes de non-divulgaration pour construire les modèles de faisceau précis en Monte Carlo. Un compromis a été de fournir les données de l'espace de phase au-dessus des mâchoires de l'accélérateur linéaire, calculées en Monte Carlo avec des paramètres de source accordés sur la base de données représentatives de *TrueBeam*. De plus, Varian a également développé une interface Web en nuage, le *Varian VirtuaLinac*, qui permet de produire des données de l'espace de phase avec des paramètres de source personnalisables en fonction de l'utilisation, sans connaître les détails géométriques du modèle Geant4. Les principaux désavantages des sources de l'espace de phase de Varian sont l'efficacité et le prix en comparaison avec un modèle de faisceau BEAMnrc/EGSnrc complet simulé en Monte Carlo. Les sources de l'espace de phase peuvent avoir des exigences de mémorisation massives, leur utilisation du réseau et disque dur peut ralentir des simulations de façon radicale, et le coût pour personnaliser les paramètres de source du VirtuaLinac aux mesures interne est non négligeable.

FalseBEAM, un modèle TrueBeam indépendant pour les faisceaux de photons 6 MV sans filtre d'aplatissement, a été construit en modifiant un modèle Varian Clinac 21EX pour 6 MV en BEAMnrc. Les dimensions géométriques et les matériaux ont été appariés avec une approche d'essai-et-erreur à la fluence et au spectre des photons/électrons des espaces de phase de Varian. Lorsque le modèle interne a été apparié à l'espace de phase de Varian avec les paramètres de source identiques, les paramètres de source ont été ajustés aux mesures internes d'une cuve d'eau, qui ont été obtenus avec un détecteur PTW microDiamond. En plus, une implémentation BEAMnrc d'un modèle PENELOPE de TrueBeam publié, FakeBeam, était investiguée. Les modèles de détecteur étaient inclus pour toutes les simulations de calcul de dose dans l'eau, afin d'inclure les effets de moyennage de volume et le fait que les matériaux du détecteur ne sont pas équivalents à l'eau. Cela a permis d'augmenter l'exactitude de la sélection des paramètres de sources dans le modèle de faisceau.

# Acknowledgements

I cannot thank Dr. Stephen Davis enough as my primary supervisor. His endless knowledge, experience, and support were invaluable to my progress in this work. Since starting a summer project in 2013, I was not only blessed to have him as my supervisor, but also as my professional mentor. For that I am extremely lucky, and I will always feel indebted. I am also indebted to Dr. Jan Seuntjens, my second supervisor; his insight into difficult problems was vital to this work and I am especially grateful for the initial opportunity in the McGill Medical Physics Unit as a summer student. This cannot be mentioned without thanking Dr. Eduardo Franco for introducing me to Dr. Seuntjens, which led to this wonderful opportunity.

Special thanks to Dr. Lorenzo Brualla, Dr. Miguel Rodriguez, and Dr. Josep Sempau for sharing their FakeBeam geometry and PENELOPE simulation data, and for fascinating discussions. Thank you to Dr. Frédéric Tessier for his Exradin A1SL and A12 models, and the NRC of Canada for answering questions regarding EGSnrc. Many thanks to Dr. Pavlos Papaconstadopoulos for his PTW microLion and microDiamond models, for his Monte Carlo lessons, and for many fruitful discussions. Questions pertaining to Varian TrueBeam phase spaces and the Varian VirtuaLinac were graciously answered by Dr. Daren Sawkey of Varian Medical Systems. The CalculQuébec clusters Guillimin, Briarée and Cottos were used for all computations. I would like to thank Dr. Shirin Enger for useful discussions on phase spaces and for her support in my search for a residency. Many thanks to Dr. Emilie Soisson for her professional support and her work recalculating lung plans in Monte Carlo. Special thanks to Robert Maglieri for helpful discussions and for paving the path to Varian CL21EX modeling. Thanks to Bhavan Siva and Joe Larkin for useful discussions. Many thanks to Margery Knewstubb and Tatjana Nisic for all administrative matters. Thank you to Dominique Guillet for the Microsoft Kinect tutorial. Merci à Véronique Fortier d'avoir corrigé mon résumé.

I cannot forget to mention my brilliant colleagues in the McGill MPU, it has been a true pleasure to work with all of you. Special thanks to my family, particularly my parents and my aunt Mary for her wonderful cooking. Finally, thanks to my friends for dealing with my disappearing act during the coursework and for all of their support. You know who you are.

# Chapter 1

## Introduction

### 1.1 Radiotherapy

Radiotherapy is a common treatment method for cancer where the patient's tumour is exposed to ionizing radiation [1]. It can be combined with surgery or chemotherapy, or it can be used on its own [2]. The goal of radiotherapy is to deposit as much ionizing radiation into cancerous tissue as possible while minimizing exposure to healthy tissue [2].

Currently, the most common delivery of ionizing radiation is in the form *external beam radiotherapy* (EBRT), where the source of radiation is delivered from outside of the patient [2]. EBRT typically uses a linear accelerator, or linac, to deliver dose to the tumour [1]. EBRT generally requires a computerized treatment plan to ensure accurate delivery to the desired target and to ensure adequate sparing of any organs at risk (OAR) [3].

Typically, a patient will be scanned at a computed tomography (CT) simulator once radiotherapy has been prescribed to obtain a three-dimensional (3D) image for definition of the target and OAR [1]. The CT simulator differs from a diagnostic CT scan in that the scanning table is flat in order to reproduce the flat couch used with the linac and the bore is larger to include accessories and for more flexibility in a patient's treatment positioning [1].

In the treatment planning stage, the target and OAR are delineated on the 3D image [3]. An arrangement of beams is selected in the treatment planning system to maximize dose coverage to the targets and minimize that to the OAR. A

deterministic dose calculation algorithm, such as convolution-superposition, simulates this process [3].

Varian linear accelerators (Palo Alto, CA) are often accompanied by the Varian Eclipse™ treatment planning system, which uses the AAA convolution-superposition algorithm. It is imperative for dose calculation algorithms to have high accuracy in order to adequately deliver the desired dose distribution to the patient [4].

## 1.2 Monte Carlo in radiotherapy

Monte Carlo dose calculations have been used in medical physics for the past 60 years [5]. Monte Carlo codes simulate the transport of particles (e.g. photons and electrons) through matter using known probability distributions that accurately model the random trajectory of individual particles for a given interaction in a particular material [6]. While convolution-superposition algorithms such as Eclipse AAA are considered accurate, Monte Carlo algorithms have been shown in many studies to be more accurate for clinical radiotherapy dose calculations when the number of incident particles is sufficient to achieve the desired uncertainty in dose, particularly in heterogeneous tissues or small fields [7]. Effects near the boundary of low density tissues have additionally been observed in-house by Dr. Emilie Soisson after recalculating over 70 lung plans using Monte Carlo [8].

Monte Carlo differs from convolution-superposition in that it transports particles stochastically as opposed to deterministically. Historically, it has not been considered feasible for clinical use due to its long computation times. However, this has changed in recent years with fast Monte Carlo algorithms now available in some treatment planning systems for clinical use, such as the Brainlab iPlan (Munich, Germany), CyberKnife MultiPlan (Accuray, Inc., Sunnyvale, CA), and Elekta Monaco (Stockholm, Sweden) treatment planning systems [9]. Conventional Monte Carlo codes, such as EGSnrc or PENELOPE, remain the gold standard [10,11].

### 1.2.1 Constructing a Monte Carlo beam model

In order to create an accurate Monte Carlo beam model of a linac, such as the Varian TrueBeam™, the user requires precise geometrical and material information from the vendor. In a Monte Carlo beam model, all components interacting with a beam must be included for an accurate simulation. Faddegon et al. showed for photon beams that the mean energy and focal spot size of the incident electron beam striking the target are key parameters, in addition to the geometrical and material composition of the exit window, target, flattening filter, and primary collimator [12].

Assuming that the vendor supplies the developer the correct linac information, the most important free parameters in the simulation that can be adjusted to one's in-house water tank measurements are the incident electron energy, focal spot size, and angular spread. The spot size was found by Sheikh-Bagheri and Rogers to have a large effect on off-axis ratios; the relative intensity of the central axis was found to increase with the width of the spot size [13]. In addition, they found that the incident electron energy had a large effect on both off-axis ratios and percentage depth dose curves (PDDs). Figure 1.1 demonstrates the effects of varying the incident electron energy and spot size on profiles, computed by Tzedakis et al. [14] and AlMBERG et al. [15], respectively.

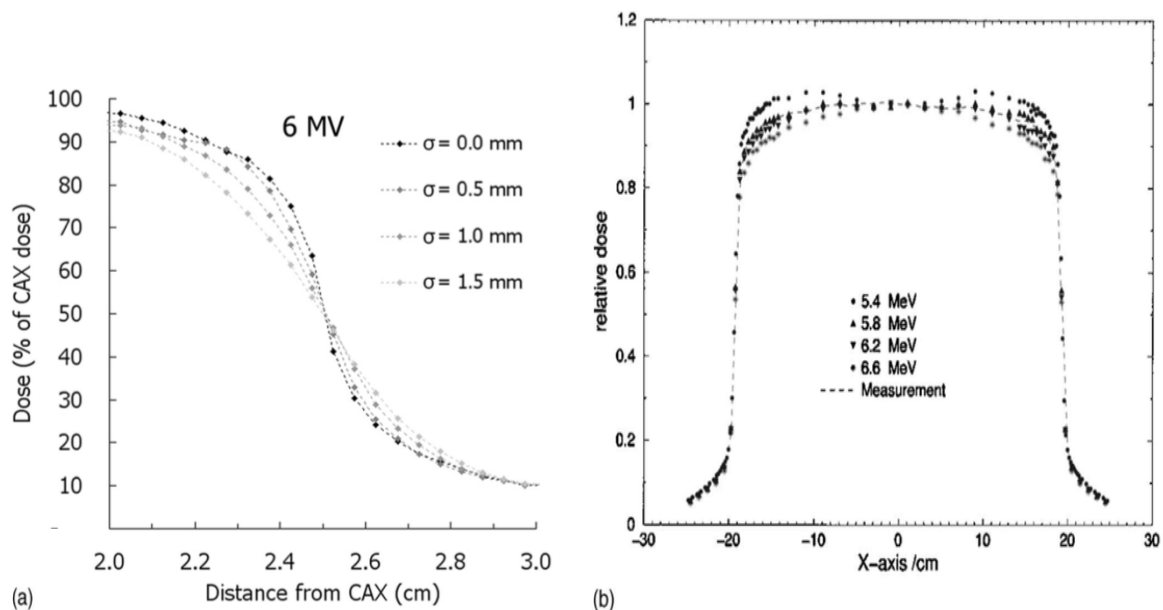


Figure 1.1: The effect of varying a) the sigma of the focal spot size on  $5 \times 5$  cm<sup>2</sup> profiles and b) the incident electron energy on  $40 \times 40$  cm<sup>2</sup> profiles. Reproduced from a) AlMBERG et al. [15] and b) Faddegon et al. with permission [14].

With the spot size having a large effect in the penumbra region of the beam profile, it is desirable to have high accuracy in this region. The penumbra region of beam profiles is highly susceptible to detector effects while measurements are obtained in a water tank [16]. Detector effects are a collective term for the non-water equivalence of the detector materials and the volume averaging effect due to the finite size of the detector's collecting volume [16]. If detector models are included in the simulation, their effects will also be included and not affect the benchmarking process of the beam model's source parameters, particularly the choice of spot size that is tuned to match the measured profile penumbra. Detector effects will be discussed further in Chapter 2.

According to recent AAPM practice guidelines [17], a treatment planning system (TPS) is recommended to achieve certain agreement in dose to water against measured water tank data. High-dose, low-gradient regions in PDDs and profiles should be within 2% local percent difference, penumbra should match within 3 mm distance-to-agreement, and the profile umbra up to 5 cm from the field edge should be within 3% of the maximum dose [17]. Example guidelines proposed in the AAPM TG-53 report suggested that agreement in the build-up region of 20% local percent difference would be considered acceptable, however this should not be considered a clinical goal [3].

### 1.2.2 Phase spaces

Efficiency is vital in a Monte Carlo simulation to obtain accurate results in a reasonable timeframe. In some cases, efficiency can be improved with the use of phase spaces [7]. A phase space stores particle information such the energy, position, and momentum, of any particle passing a user-defined plane into a phase space file. One can use phase spaces to increase efficiency by simulating the *patient-independent* part of a simulation, e.g., the target to a plane above the jaws, and scoring a phase space above the *patient-dependent* part, e.g., jaws, MLCs (Figure 1.) [7]. The user can then import this file into any patient-dependent part of a simulation, for any number of patients, which saves the computational time required to transport particles in the patient-independent portion.

The size of phase space files increase as the number of particles stored within it increase. More particles in a phase space are desirable to increase the accuracy of simulations. However, as phase space files becomes too large, the speed of the simulation is eventually limited by the network and hard drive speeds of the system, reducing efficiency [7]. Advances in network and hard drive speeds are slow relative to increases in CPU speeds, which carry out the Monte Carlo calculations [7]. In some cases, it can be more efficient to simulate the full model, i.e., include the patient-independent components, than to import a phase space and simulate only the patient-dependent structures.

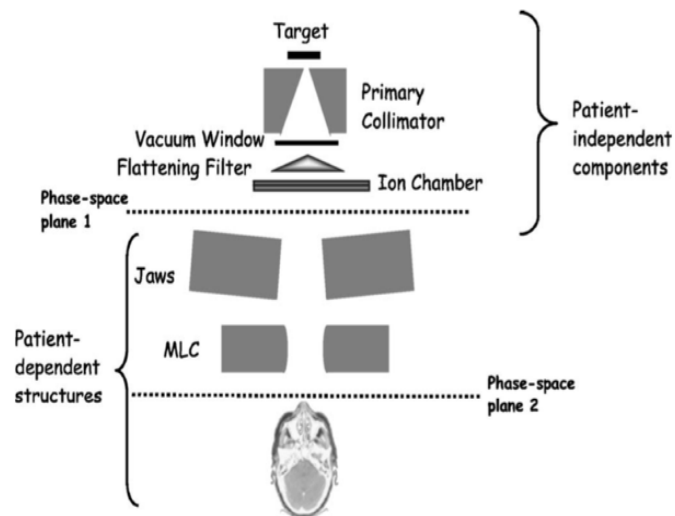


Figure 1.2: Illustration of the components of a typical Varian linear accelerator treatment head in photon beam mode. Phase space planes for simulating patient-dependent and patient-independent structures are also represented. Reproduced from Chetty et al. with permission [7].

### 1.3 Varian's TrueBeam phase space solution

Creating an accurate beam model in Monte Carlo requires the geometric and material details of the linear accelerator. In the past, this information was shared by manufacturers under non-disclosure agreements with institutions conducting research. Varian will no longer provide this information for the Varian TrueBeam. As outlined in their 2013 Monte Carlo newsletter [18], some of their reasons for this are: i) their wish to retain intellectual property, ii) non-disclosure agreements were not respected in the past, iii) high upkeep (~2000 emails) requesting further information with no revenue generated in exchange, and

iv) they no longer wish to be responsible for the quality of geometrical and dimensional information.

The quality of information distributed by Varian is vital to achieve optimal accuracy in a beam model, and mistakes have occurred in the past. An error in the distributed primary collimator dimensions of the Varian Clinac series was admitted by Varian after Chibani and Ma observed that increasing the entrance and exit radii of the primary collimator by 2 mm led to better agreement in the build-up region [19].

To accommodate the needs of the Monte Carlo community, Varian has compromised by releasing International Atomic Energy Agency (IAEA) formatted phase space data with the upper components of the TrueBeam simulated in Geant4, a general purpose Monte Carlo code [20,21]. The phase space plane is located above the jaws (Figure 1.). The source parameters of their model were tuned to match the Varian representative beam data for Eclipse [22,23], using a fixed spot size based on measurements [24]. In addition, Varian has created the VirtuaLinac, a cloud interface allowing institutions to generate phase space data with adjustable source parameters and certain customizable geometrical components (Figure 1.) [25]. While the VirtuaLinac interface is freely provided by Varian, the user must rent compute nodes on a pay-as-you-go basis through Amazon Web Services to perform the calculations. The larger the desired phase space, the greater the required simulation time and therefore, the greater the cost.

## 1.4 Disadvantages of TrueBeam phase spaces

There are a number of disadvantages to Varian's phase space compromise. Primarily, the Geant4 TrueBeam model used to generate the generic phase space data and used in VirtuaLinac simulations is a "black box." External institutions will no longer have the chance to detect errors in the beam model, such as the previously discussed example with the primary collimator radii detected by Chibani and Ma [19]. In addition, the cost to tune a model to in-house water tank data is not negligible. When including detector models in the calculation to include the effects of volume averaging and the non-water equivalence of the detector materials, the cost to tune a model following the procedure followed by Almberg [15] (discussed in Chapter 3) is at least 400 USD per energy.<sup>1</sup> The cost could

<sup>1</sup>Phase spaces must be at least 40 GB for accurate simulations using detector models. The cost of generating a 40 GB VirtuaLinac phase space (100  $\mu\text{m}$  range cut, brem splitting set to 100) is approximately 40 USD. At least 10 phase spaces are needed to tune the incident electron energy, spot size, and angular spread.

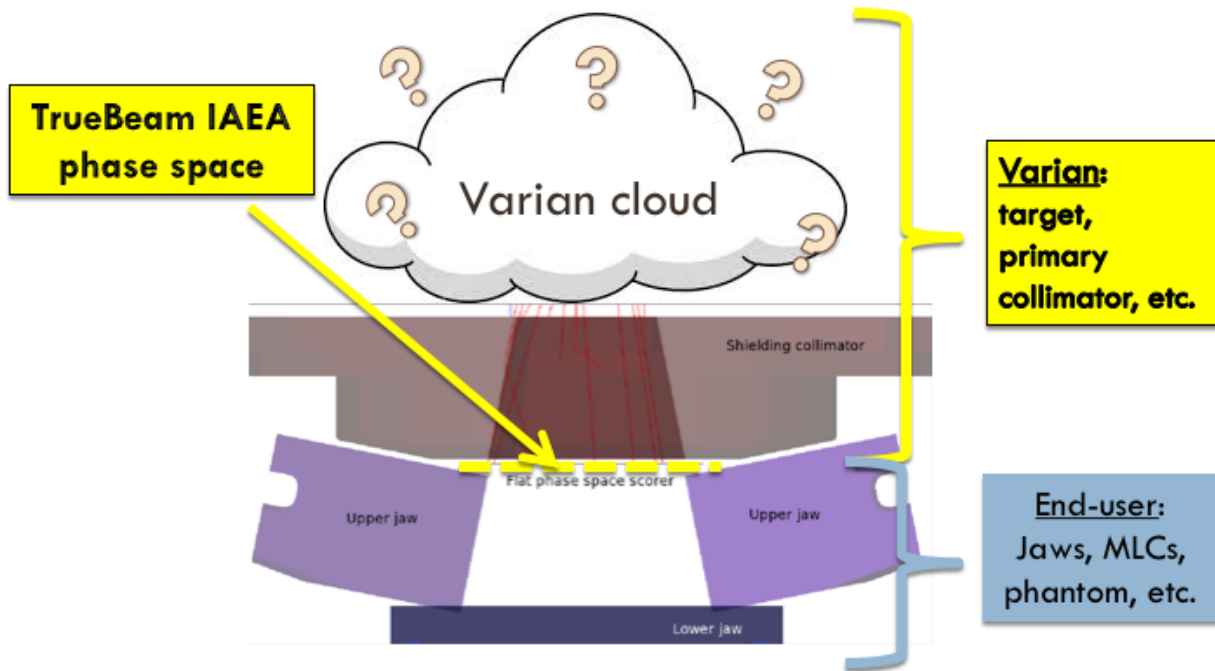


Figure 1.3: Varian IAEA phase space plane.

Welcome to Varian's VirtualLinac

Copyright © 2013-2015 Varian Medical Systems

**VARIAN** medical systems | A partner for life

Platform: TrueBeam		Beam type: X-rays	
<b>Physics</b> Code: Geant4 Version: 10.1.patch1 Physics list: QGSP_BIC_EMZ Range cut: 100 μm Brem splitting: 1		<b>X-rays</b> Target: LowEnergy, MediumEnergy, HighEnergy, Imaging, Custom Flattening filter: 6x FF position offset: X 0 Y 0 Z 0 mm Rel. FF density:	
<b>Incident Beam</b> Energy: 5.9 MeV Energy spread: 0.051 MeV Spot size X: 0.6645 mm Spot size Y: 0.7274 mm Spot position X: 0 mm Spot position Y: 0 mm Beam angle X: 0 deg Beam angle Y: 0 deg Angular divergence X: 0.0572957 deg Angular divergence Y: 0.0572957 deg Phase space input		<b>General</b> Write phase space file: <input checked="" type="checkbox"/> Phase space position: 733 mm BEAMnrc format: <input checked="" type="checkbox"/> Record leakage: <input type="checkbox"/> Simulate phantom: <input checked="" type="checkbox"/> Phantom size: X 500 Y 500 Z 400 mm Phantom voxels: X 50 Y 50 Z 40 Splitting factor: 1 # of incident electrons: 100000 Random number seed: 1 Comment: Output file name: testing	
		<b>Beam shaping</b> Simulate jaws: <input checked="" type="checkbox"/> Jaw Y1: -20 cm Jaw Y2: 20 cm Jaw X1: -20 cm Jaw X2: 20 cm Collimator rotation: 0 deg Simulate head shielding: <input checked="" type="checkbox"/>	

Run

[Home](#) [Files](#) [Usage](#) [Readme](#) [Contact](#)

Figure 1.4: Varian VirtualLinac interface. Printed with Varian's permission.

be lowered by improving the efficiency of the VirtuaLinac, such as by implementing the more efficient directional bremsstrahlung splitting (DBS) variance reduction technique over the currently used uniform bremsstrahlung splitting (UBS) [26]. In DBS, bremsstrahlung photons are only split if they are directed into a field of interest. This improved photon fluence efficiency by a factor of 20 over UBS in BEAMnrc for a simulated 6 MV 10 x 10 cm<sup>2</sup> field [26].

With the VirtuaLinac constantly being updated to newer versions that include updated versions of Geant4, institutions will be forced to validate their phase space data on

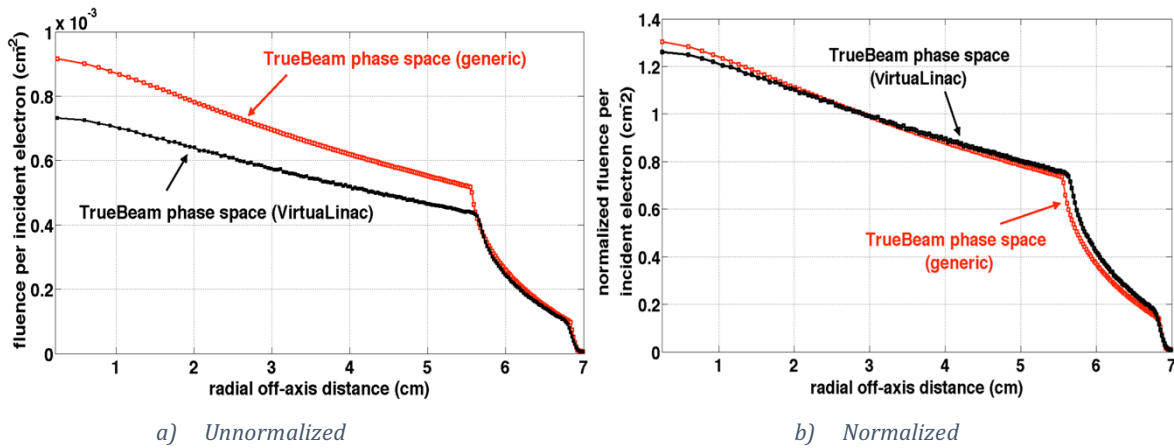


Figure 1.5: a) Unnormalized and b) normalized fluence profiles comparing TrueBeam phase spaces released by Varian (generic) and generated on the VirtuaLinac with the same source parameters. The VirtuaLinac phase space was generated with a newer Geant4 version and physics list, as recommended by Varian. The normalization point was selected arbitrarily approximately 3 cm radially off-axis. Phase spaces were scored above the linac jaws.

an ongoing basis. The 6 MV FFF radial fluence profiles shown in Figure 1.5 demonstrate noticeable differences between the generic TrueBeam phase space released by Varian and phase space data generated on the VirtuaLinac (version 1.1.8) with the same source parameters. The changes made with the phase space generated with the VirtuaLinac are a newer recommended Geant4 version (geant4-10-01-patch-01) and physics list (QGSP\_BIC\_EMZ) compared to the generic phase space data Geant4 version (geant4-09-04-patch-02) and physics list (QGSP\_BIC\_EMY). In Geant4, physics lists contain a set of models that govern physical interactions in Monte Carlo calculations [4]. Several validated Geant4 reference physics lists have been released, with the choice of physics list dependent on the application [4]. The unnormalized difference in particle fluence per incident electron is explained by the changed bremsstrahlung cross sections in the newer version of Geant4 [27].

Phase spaces also present a number of problems in Monte Carlo simulations. When using phase space sources in Monte Carlo simulations, particle recycling is an effective tool to reduce the uncertainty in dose calculations [28]. However, one disadvantage of phase spaces is that there is a limit to the uncertainty achievable using recycling that is proportional to its size. This is known as the latent uncertainty of the phase space [29]. As particle recycling is increased, the uncertainty in dose will decrease as [28]

$$s^2 = \sigma_0^2 + \frac{\sigma^2}{N_r}, \quad (1.1)$$

where  $s$  is the uncertainty in dose,  $\sigma_0$  is the latent uncertainty,  $\sigma_0^2 + \sigma^2$  is the variance with no particle recycling, and  $N_r$  is the number of times the particle was recycled.

In order to achieve adequate statistical uncertainty in dose, massive phase space files are often required, imposing substantial storage requirements onto the user. Approximately 500 GB of phase space data have been released by Varian for seven photon and eight electron beam modes to achieve reasonable agreement for most field sizes [18]. Tuning an energy with the VirtualLinac using the methods of this work requires several terabytes of storage.

Massive phase space files impose a penalty in terms of simulation time [7]. Intuitively, one would expect that using phase space sources beginning above the jaws to be faster than running a full model that begins at the target. This is not the case in practice when importing large phase spaces, due to network and hard drive speeds being slow relative to CPU speeds.

In addition, it is not straightforward to implement phase space sources for simulation in the EGSnrc system when using a shared library source. In EGSnrc, the particle transport in the linac is controlled by BEAMnrc [30], with transport in the phantom controlled by other user codes in the system. When running a shared library simulation, the user code operating the second part of the simulation (e.g., a phantom simulation in DOSXYZnrc [31]) demands particles on the fly from the exit plane of the BEAMnrc simulation (Figure 1.6). When using TrueBeam phase spaces above the jaws in the BEAMnrc input and when running a shared library, EGSnrc was currently observed in this work to incorrectly partition the particles in the phase space when parallelized. Accurate parallelization, i.e., dividing a simulation over multiple processor cores to improve simulation speed, is an important aspect of complex Monte Carlo simulations that require low statistical uncertainties. Instead of partitioning the phase space in equal parts for each parallel simulation, the same part is used by each parallel

run. This results in one small portion of the phase space being recycled multiple times, greatly increasing the latent variance.

The current impractical solution to this problem is to separate the two components of the simulation entirely, by simulating to a second phase space plane above the surface of the water. The second user code will then import the second phase space as a source into the simulation. This method negatively impacts simulation efficiency for two reasons. Primarily, there can be a delay period of days before simulations begin on the CalculQuébec clusters used in this work, and this waiting period must now occur twice when separating simulations into two parts. Additionally, the large phase space files now need to be imported twice, which decreases simulation efficiency.

## 1.5 TrueBeam models: FakeBeam and FalseBEAM

To resolve the problems stemming from Varian phase spaces, two alternative approaches were investigated to model the TrueBeam for the 6 MV flattening filter free (FFF) beam. Both solutions involved modifying Varian Clinac 2100 series Monte Carlo models, since large similarities have been observed in Varian's Monte Carlo data packages between the Varian Clinac 2100 series and the Varian TrueBeam for the jaws and components downstream from them [32]. The first solution was to implement a BEAMnrc version of an existing beam model

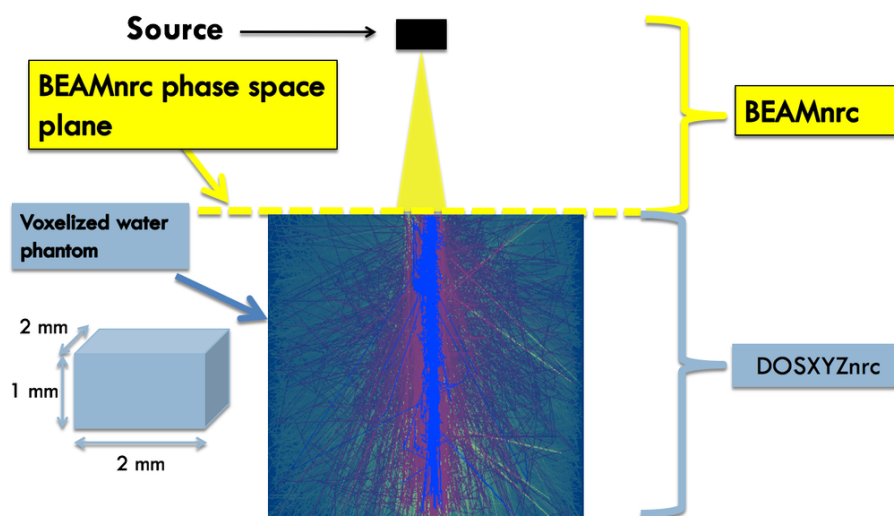


Figure 1.6: BEAMnrc/DOSXYZnrc simulation components.

of the TrueBeam, known as FakeBeam [32]. FakeBeam was modeled in the PENELOPE Monte Carlo code [11]. The second TrueBeam model, called FalseBEAM, was created by matching TrueBeam phase space data provided by Varian.

### 1.5.1 FakeBeam

Rodriguez et al. found that the TrueBeam could be modeled for the 6 MV FFF and 10 MV FFF beams by replacing the flattening filter of a Varian Clinac model (Figure 1.7) with a fictitious thin bronze and tantalum filter, respectively. The dimensions of the filters were tuned in a trial and error approach to optimize agreement in dose to water. The bronze filter used by FakeBeam for the 6 MV FFF beam is shown in Figure 1.8. FakeBeam was shown to achieve excellent agreement with measurements for dose to water calculations [32]. A comparison of dose to water in a voxelized phantom between FakeBeam and TrueBeam phase space sources from Varian is shown for PDDs and profiles of various field sizes in Figure 1.9 and Figure 1.10, respectively. It should be noted that the percent differences are relative to the maximum dose, which lowers the magnitude compared to a local percent difference. In many ways, it appears that the FakeBeam model achieves better agreement in PDDs and profiles than when a TrueBeam phase space from Varian was used, with the exception of the PDD

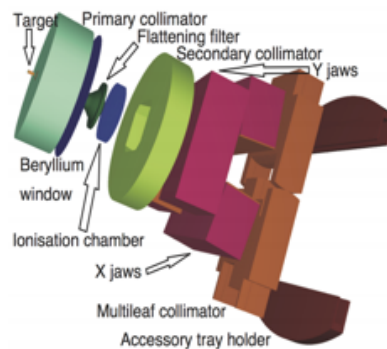


Figure 1.7: PENELOPE Varian Clinac series model. Reproduced from the PRIMO user manual with permission [33].

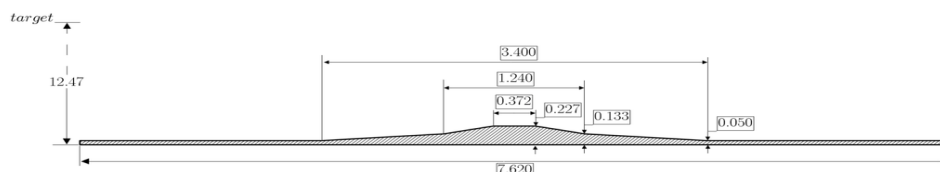


Figure 1.8: FakeBeam bronze 6 MV FFF filter in centimetres. Reproduced from Rodriguez et al. with permission [32].

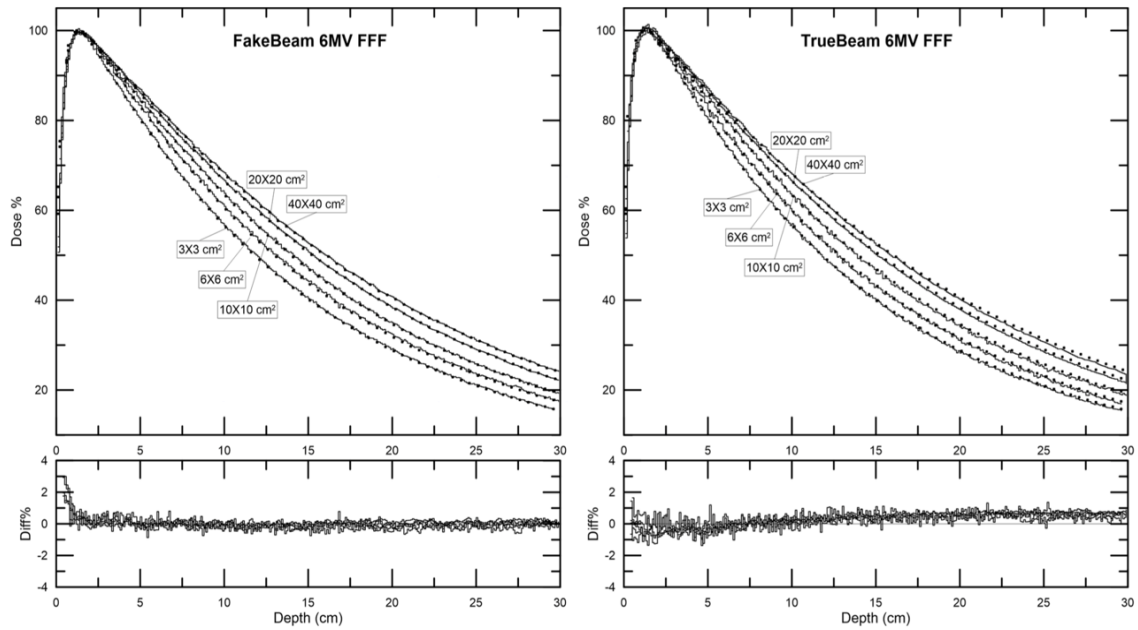


Figure 1.9: Rodriguez et al.'s comparison of measurements (dots) to Monte Carlo calculated FakeBeam and TrueBeam phase space (lines) PDDs. The percent difference is relative to the maximum dose. Statistical uncertainties are in the range of 0.3 to 0.8%.  
Reproduced from Rodriguez et al. with permission [32].

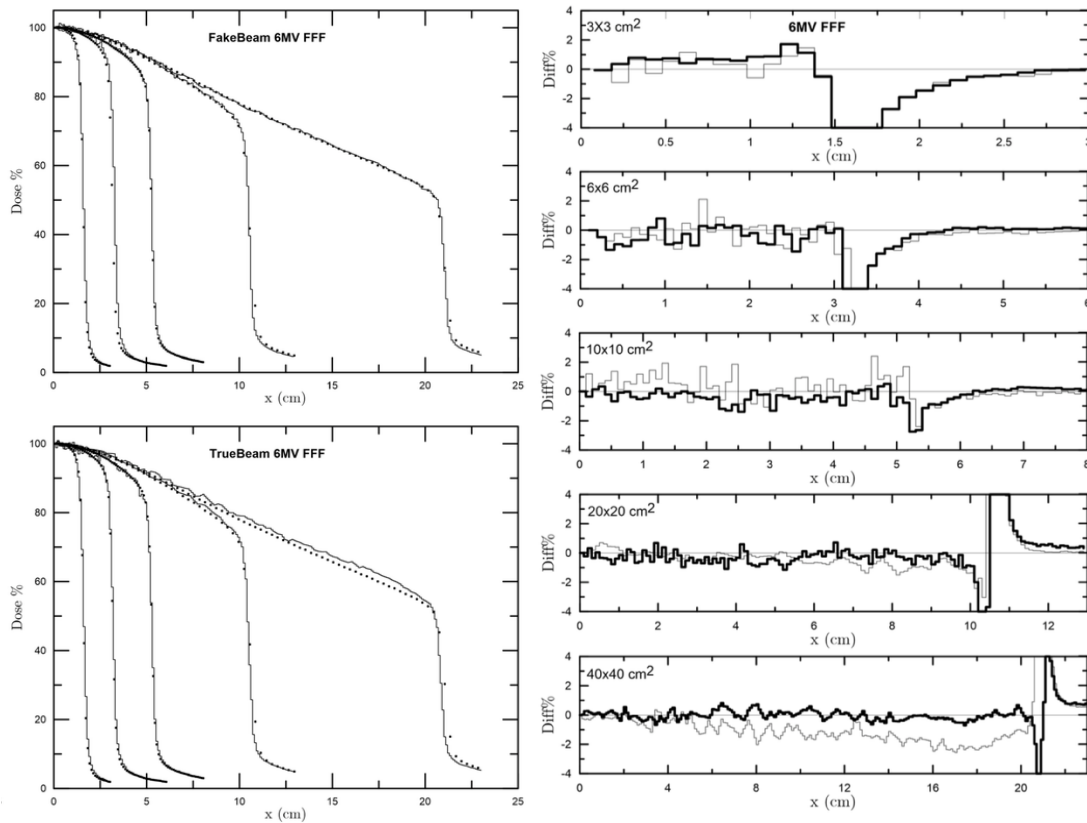


Figure 1.10: Rodriguez et al.'s comparison of measurements (dots) to Monte Carlo calculated FakeBeam and TrueBeam phase space (lines) profiles at 5 cm depth. The percent difference curves of FakeBeam (black) and TrueBeam (gray) are relative to the maximum dose. Statistical uncertainties are in the range of 0.3 to 0.8%.  
Reproduced from Rodriguez et al. with permission [32].

build-up region. The calculations are compared to measured Varian TrueBeam representative data using the IBA Dosimetry CC13 ionization chamber (Schwarzenbruck, Germany) for all PDDs and profiles, with the exception of the 3 x 3 cm<sup>2</sup> PDD and 3 x 3 cm<sup>2</sup>, 6 x 6 cm<sup>2</sup>, and 10 x 10 cm<sup>2</sup> profiles, where the IBA PFD diode was used. An implementation of FakeBeam was investigated in BEAMnrc for the 6 MV FFF beam, in order to maintain compatibility with the McGill Monte Carlo Treatment Planning System (MMCTP).

### **1.5.2 FalseBEAM**

The second in-house solution, FalseBEAM, was created by reproducing the fluence and spectra of TrueBeam phase space data for the 6 MV FFF beam by modifying the geometries and materials of an existing CL21EX model, while using the same source parameters used in the Varian TrueBeam Monte Carlo model. If the phase space data above the jaws from the in-house model can reproduce the TrueBeam phase space data distributed by Varian, then there should be no need to use the data from Varian. Once FalseBEAM was matched to the Varian phase space data, it was validated in dose to water calculations with the TrueBeam representative data. Finally, the source parameters were tuned to match in-house water tank measurements.

## **1.6 Thesis outline**

In this work, a Varian Clinac series model was modified to create an accurate Monte Carlo beam model of the Varian TrueBeam. This was done in two ways: i) by reproducing an existing PENELOPE TrueBeam model, called FakeBeam, in BEAMnrc, and ii) by modifying the CL21EX geometrical and material parameters to match TrueBeam phase space data provided by Varian with identical source parameters (FalseBEAM).

Chapter 2 discusses the Monte Carlo detector models used for commissioning the source parameters of the CL21EX model and for calculating dose to water in the final TrueBeam model. It will also demonstrate detector effects in dose to water profiles. In Chapter 3, the procedure for tuning the source parameters of a beam model is discussed, specifically for the 6 MV CL21EX model used as a basis for FalseBEAM. Tuning processes

included the chamber effects discussed in Chapter 2, which allowed for higher dosimetric accuracy in profile penumbrae after tuning the beam model spot size.

Chapter 4 discusses the methods used to create the TrueBeam models and the water tank measurements used to benchmark the source parameters of FalseBEAM, following the methods outlined in Chapter 3. The results of these simulations are discussed in Chapter 5.

## Chapter 2

# Detector effects in linear accelerator

## Monte Carlo simulations

As discussed in section 1.2.1, effects caused by the presence of detectors in water tank scans perturb measurements that attempt to measure dose to a point in water. These detector effects occur due to the non-water equivalence of the detector's materials and its volume averaging effect [16]. The detector material's effect includes the sensitive volume having a different density and atomic composition from liquid water, as well as the presence of the detector's other components [16]. These effects result in a change in the charged particle fluence that would be present in water in the absence of the detector [16]. The volume averaging effect is due to the finite size of the detector's sensitive volume. The effect of ionization chamber materials and the volume averaging effect of ionization chambers in the penumbra region of profiles are demonstrated in sections 2.2.1 and 2.2.2, respectively.

For these reasons, detector models were included in Monte Carlo simulations of dose to water calculations using the *egs\_chamber* user code of the EGSnrc package [34,35]. Using detector models improves accuracy in the build-up region of PDDs and the penumbra region of profiles. For this reason, using ionization chamber models led to improved accuracy in the determination of the source parameters of the Varian CL21EX model described in Chapter 3. Detector models used in Monte Carlo simulations could additionally be used to determine correction factors that could be applied to water tank measurements.

The PTW microLion liquid ionization chamber (Freiburg, Germany) was modeled in *egs\_chamber* to commission the source parameters of the CL21EX model (Figure 2.1). Exradin A1SL and Exradin A12 (Standard Imaging, Inc., Middleton, WI) air-filled ionization chambers were modeled to validate the CL21EX model against measurements with each respective detector (Figure 2.1). In addition, the IBA CC13 and PTW microDiamond detectors were modeled to validate the FalseBEAM model of the Varian TrueBeam.

The Exradin A1SL and A12 models were supplied by Dr. Frédéric Tessier of the National Research Council of Canada (NRC). The PTW microLion and microDiamond models were supplied by Dr. Pavlos Papaconstadopoulos. All detectors were modeled according to proprietary vendor specifications.

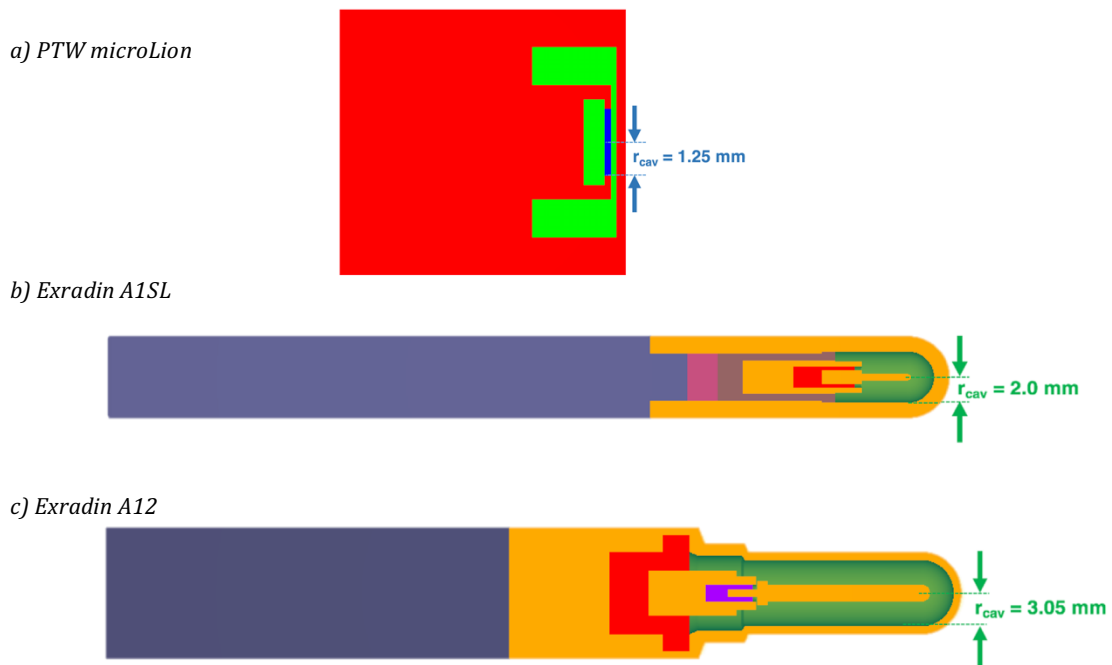


Figure 2.1: Chamber model cross sections created in *egs\_view* of a) the PTW microLion liquid ionization chamber, b) the Exradin A1SL air-filled ionization chamber, and c) the Exradin A12 air-filled ionization chamber. The nominal cavity radius,  $r_{cav}$ , is included for each chamber. All displayed component dimensions in this figure were modified to protect the confidentiality of the chamber designs. The chamber stem of the Exradin models is not displayed in the figure, but was included in the A1SL and A12 models. No chamber stem was included in the microLion model.

## 2.1 *egs\_chamber* simulations

The C++ *egs\_chamber* user code of the EGSnrc Monte Carlo system was used to model detectors and to score dose to their cavities for simulation of PDDs and profiles [32,33]. In addition, it was used to compute perturbation effects in the form of dose ratios of the dose scored by a full detector model to the dose scored to a region of interest, including a point in water modeled as a small water voxel. The *egs\_chamber* code was used as a shared library with BEAMnrc to transport particles beyond the end-point of the CL21EX simulations; a phase space plane at 100 cm SSD (Figure 2.2) for profiles and at 95 cm SSD for PDDs to account for air-filled chambers being partially submerged near the water surface.

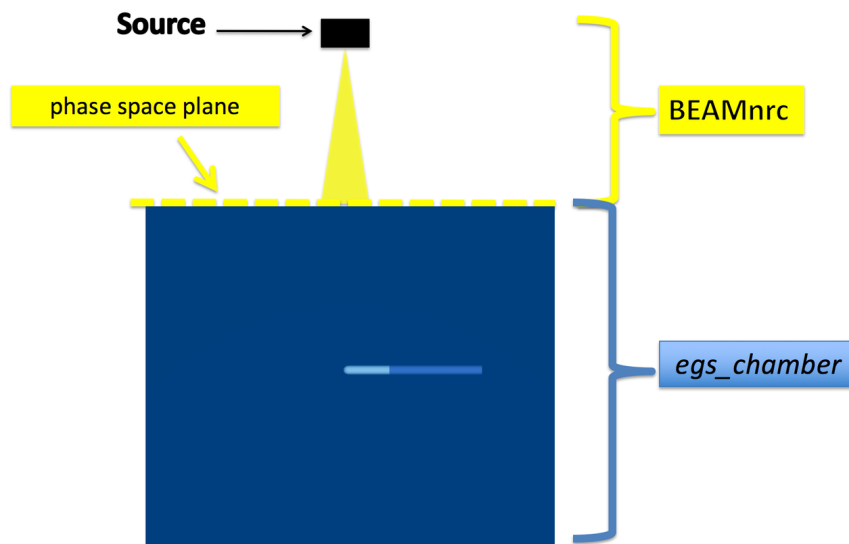


Figure 2.2: BEAMnrc/*egs\_chamber* shared library simulation

### 2.1.1 Variance reduction techniques in *egs\_chamber*

Variance reduction techniques (VRTs) are used in Monte Carlo simulations to improve efficiency, thereby reducing simulation time. VRTs decrease the variance for a given number of histories without affecting the physics of the simulation [7]. VRTs were used in all BEAMnrc simulations in addition to the *egs\_chamber* component of the simulations. BEAMnrc VRTs are discussed in section 3.2.1.

A number of variance reduction techniques described by Wulff et al. [35] were implemented in *egs\_chamber* to improve efficiency, including photon cross-section enhancement (XCSE), intermediate phase space storage and correlated sampling. The aim of XCSE is to decrease the mean free path of photons by increasing their cross section by a free parameter  $b$  on a region-by-region basis, thus increasing the number of electrons generated along the photon's path. XCSE introduces fictitious photon interactions that do not alter the path or energy of the photon, while increasing the number of generated electrons. For more information on XCSE, consult the article by Wulff et al. [35].

Intermediate phase space storage (IPSS) stores particle information at a user-defined region around a volume of interest that encompasses all detector locations, eliminating the need to repeat the location-independent components of the simulation. Correlated sampling (CS) is similar to IPSS, but the region of interest is around each individual position. Correlated sampling will pause transport at the boundary of this region of interest and continue from this point for any number of desired perturbation factor calculations. For example, CS could be used to calculate the dose to a detector's cavity and the dose to a small water voxel from this same starting point.

### 2.1.2 Depth dose and profile calculations

Percentage depth dose curves and profiles at 10 cm depth were calculated for beams at 100 cm SSD. BEAMnrc was used for particle transport up to or near the surface of a 40 x 40 x 40 cm<sup>3</sup> water phantom, and *egs\_chamber* was used for all in-phantom computations. All simulations had 1 mm resolution with uncertainties in all scoring regions below 0.5%, with the exception of profile umbra, which were below 1.0%.

XCSE was used with an enhancement factor of 2048 in all detector cavity regions and regions surrounding the cavity; enhancement factors of 256 were used in all other detector regions. As recommended in the *egs\_chamber* manual, a 1 cm thick XCSE shell with an enhancement factor of 256 was used to surround the detector. The shell was composed of water for all positions, with the exception of positions close to the phantom surface, where

portions of the XCSE shell were in air (Figure 2.3). An intermediate phase space storage (IPSS) volume surrounding the XCSE shell was used.

Electron and photon cutoff energies (ECUT and PCUT), the energies below which particles are stopped and their energy is deposited locally, were set to 0.7 MeV and 0.01 MeV, respectively. The EGSnrc cutoff energies include rest mass, so a 0.7 MeV electron cutoff corresponds to 0.189 MeV kinetic energy. All EGSnrc physics options used in *egs\_chamber* simulations were based on recommendations in the EGSnrc manual [10].



Figure 2.3: Exradin A12 at 1 cm depth with an air/water XCSE shell.

## 2.2 Ionization chamber perturbations

This section will demonstrate ionization chamber perturbation effects in the form of dose ratios that were evident in the profile penumbra of a commissioned 18 MV Varian CL21EX BEAMnrc model. Chamber material and volume averaging perturbation effects were calculated for the Exradin A1SL, Exradin A12, and PTW microLion chambers. Correlated sampling was used to compute all dose ratios. Profiles of the ratio of absorbed dose to water to dose to the detector,  $D_w/D_{det}$ , are shown in sections 2.2.1 and 2.2.2. Dose ratios are not normalized to the central axis; this would be necessary to apply a correction to a normalized measurement.

### 2.2.1 Chamber material perturbations

The chamber material's effect is due to the sensitive volume having a different density and atomic composition from water, as well as the non-water equivalence of the detector's other components. Correlated sampling was used to compare full ionization chamber models to identical geometries with all components filled with water (Figure 2.4). The volume

averaging effect was not a contributing factor because dose was scored to identical cavity geometries. Dose ratio profiles in 1 mm steps for 5 x 5 cm<sup>2</sup> fields of the PTW microLion and Exradin A1SL are shown in Figure 2.5 and Figure 2.6, respectively. To first order, one would expect the IBA CC13 to have a similar material perturbation effect as the Exradin A1SL due to it also having an air-filled cavity (neglecting differences in the other chamber components).

The unnormalized dose ratios in the central region are consistent with the mass collision stopping-power ratio of water to its detector's medium; iso-octane ( $\approx 0.94$ ) and air ( $\approx 1.06$ ) for the microLion and A1SL, respectively. The change in ratios at the field edge is due to a combination of effects. The most influential is the density of the detector's active volume; the low density of air ( $1.20 \times 10^{-3} \text{ g/cm}^3$ ) relative to water for the A1SL results in a larger change at the field edge when compared to the microLion, which has an iso-octane cavity with a density near that of water ( $0.69 \text{ g/cm}^3$ ). Additionally, there is a combined effect of all other detector components, such as the chamber walls and electrode. Finally, the change in the secondary electron spectrum at the field edge results in a change in the stopping-power ratio of water to detector material. The change in dose ratios in the profile umbra are due to changes in the electron and photon spectra, which are substantially lower in energy.

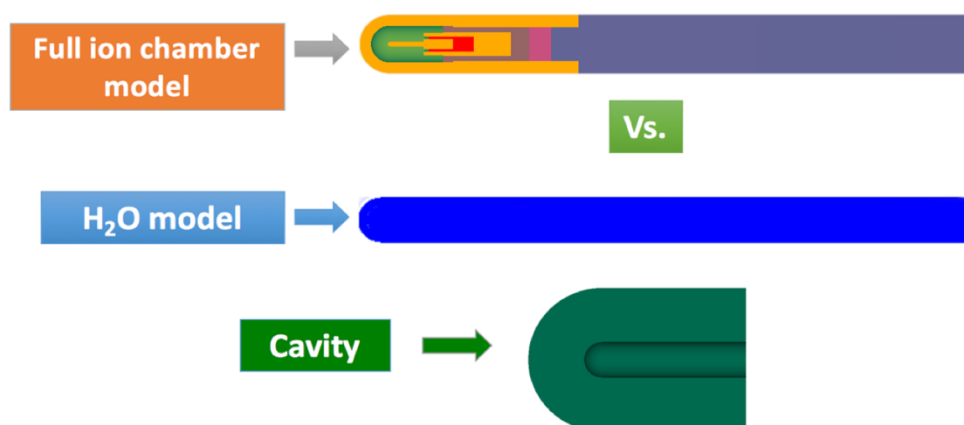


Figure 2.4: Correlated sampling was used to calculate dose ratio profiles comparing a full ionization chamber model to the same chamber model with all components made up of water. Cavity geometries were identical to exclude the volume averaging effect. The A1SL chamber component dimensions in this figure were modified to protect the confidentiality of the chamber design. The chamber stem is not displayed in the figure, but was included in the A1SL model.

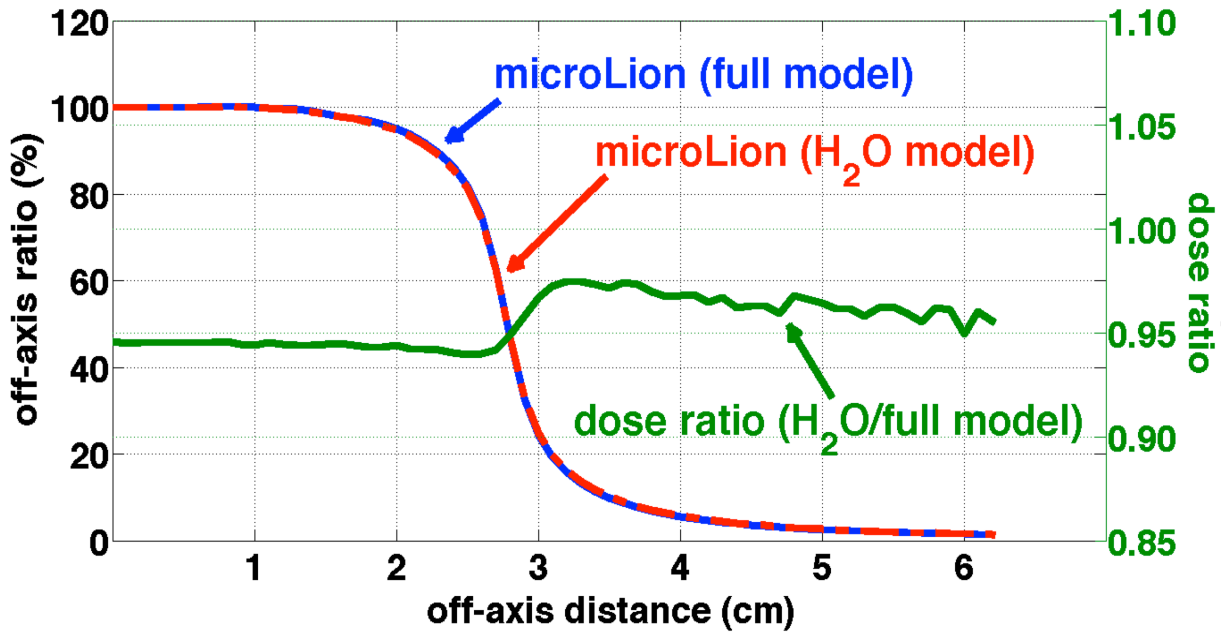


Figure 2.5: Dose ratio profile of a  $5 \times 5 \text{ cm}^2$  18 MV beam using the PTW microLion liquid ion chamber demonstrating the chamber material perturbation effect. Dose ratios are not normalized to the central axis; this would be necessary to apply a correction to a normalized measurement.

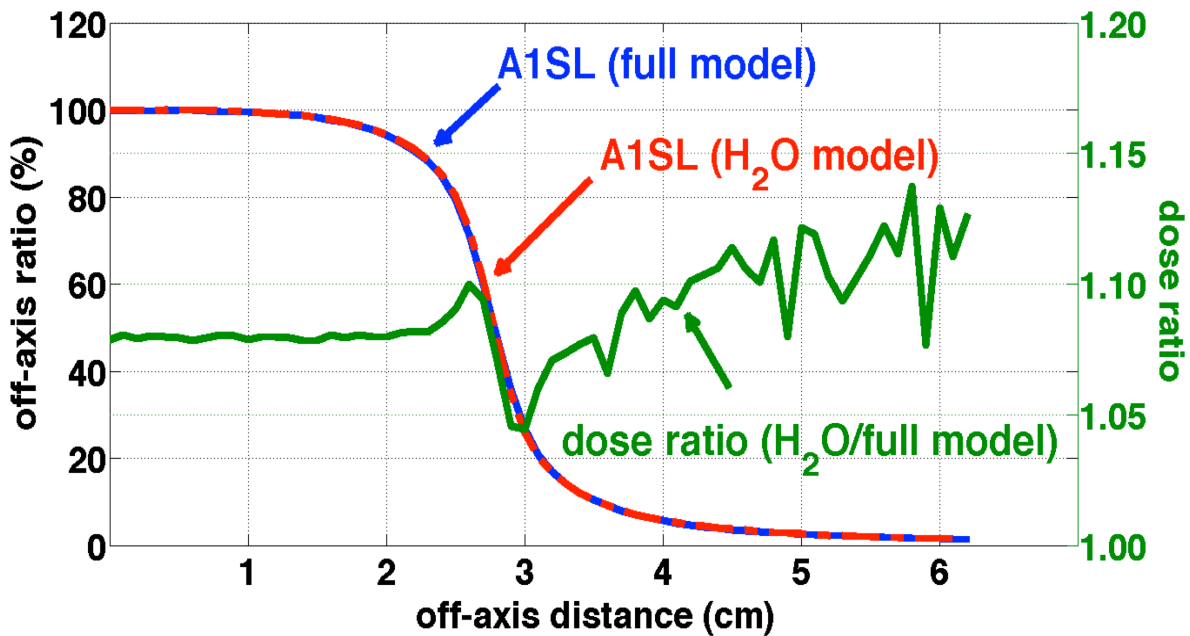


Figure 2.6: Dose ratio profile of a  $5 \times 5 \text{ cm}^2$  18 MV beam using the Exradin A1SL air-filled ion chamber demonstrating the chamber material perturbation effect. Dose ratios are not normalized to the central axis; this would be necessary to apply a correction to a normalized measurement.

### 2.2.2 Volume averaging perturbations

The volume averaging effect is due to the finite size of the detector's sensitive volume. This is undesirable in the penumbra region of profiles, where this will cause a blurring effect. The effect of volume averaging was added to the perturbation of the previous section by comparing the full chamber model to an idealized "point" detector; a  $0.3 \times 1.0 \times 0.3 \text{ mm}^3$  water voxel (Figure 2.7). The water voxel was longer in the direction perpendicular to the calculated profile to improve simulation efficiency.

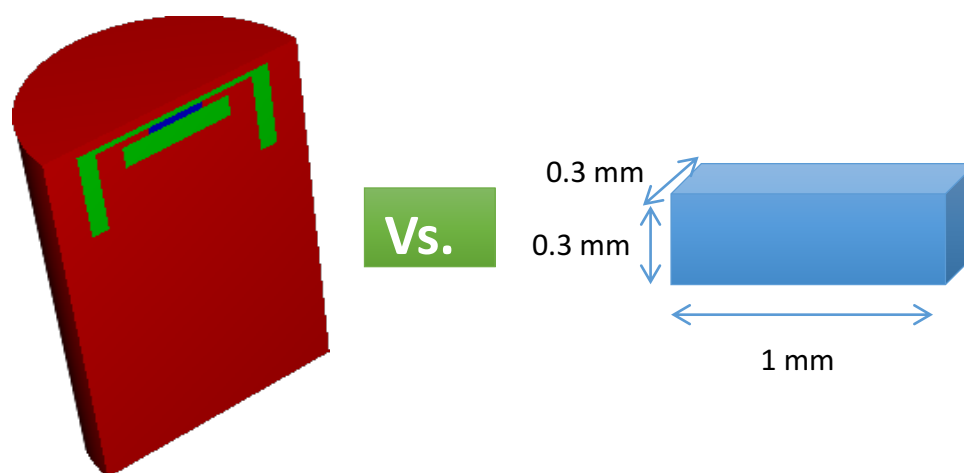


Figure 2.7: Correlated sampling was used to calculate dose ratio profiles comparing a full ionization chamber model to a  $0.3 \times 0.3 \times 1.0 \text{ mm}^3$  water voxel. The chamber component dimensions of the PTW microLion in this figure were modified to protect the confidentiality of the chamber design.

Dose ratio profiles for  $5 \times 5 \text{ cm}^2$  fields for the PTW microLion and Exradin A12 are shown in Figure 2.8 and Figure 2.9, respectively. For the microLion, the addition of volume averaging overcompensates for the increase in dose ratio at the field edge, causing a net decrease. Having a 2.5 mm cavity diameter, this is a minor effect when compared to the lengthwise perturbation of the 24.7 mm long A12 air cavity. The A12 volume averaging perturbation would be less severe, but still significant, if scanned along the cavity's radial dimension, with a cavity diameter of 6.1 mm. With a 6.0 mm cavity diameter, one would expect the IBA CC13 to have a similar volume averaging effect along the chamber's radial direction as the A12.

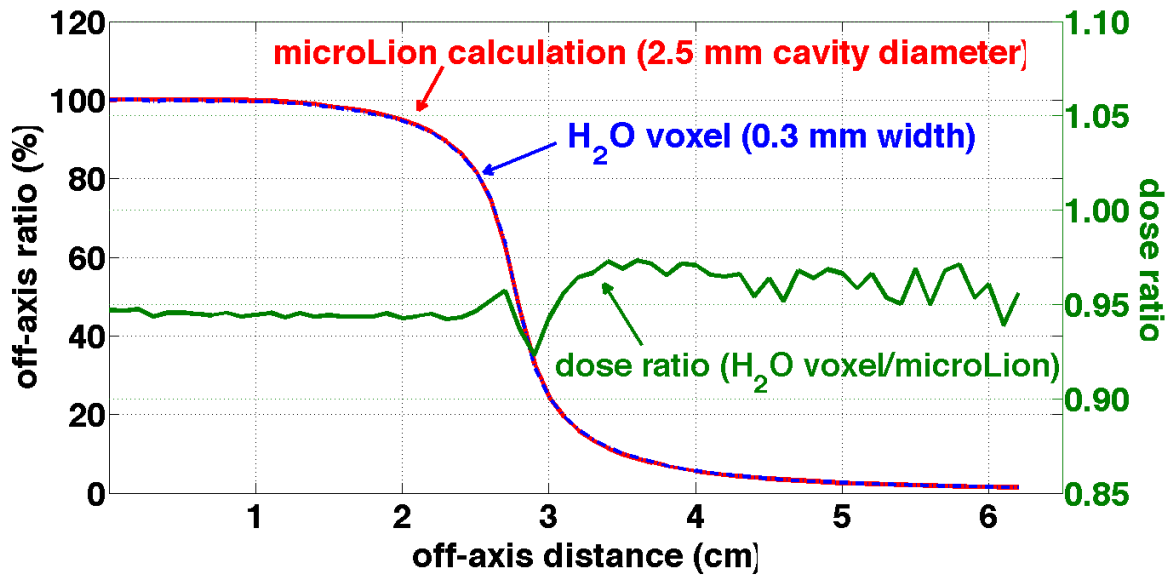


Figure 2.8: Volume averaging effect of the PTW microLion liquid ion chamber profile compared to a 0.3 mm long water voxel.

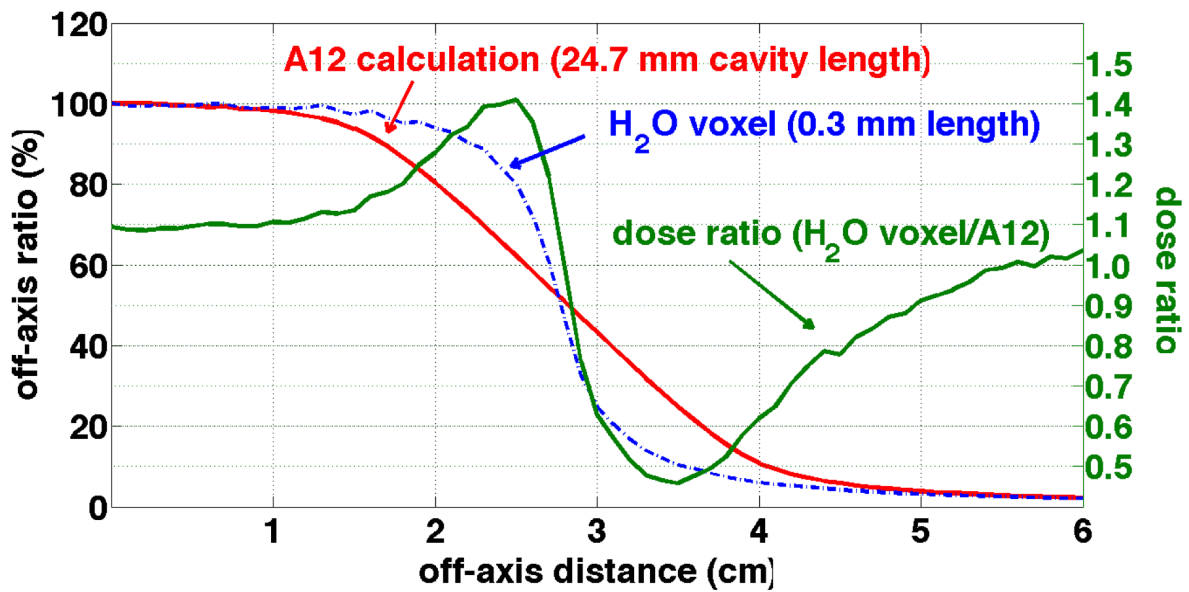


Figure 2.9: Volume averaging effect of the Exradin A12 farmer chamber profile scanned length-wise shows significant blurring of the penumbra when compared to a 0.3 mm long water voxel.

## 2.3 Diode and synthetic diamond detector perturbation effects

Silicon diodes have relatively small active volumes with high radiosensitivity, making them particularly useful in small fields and electron fields [36]. They are known to over-respond in small fields [37], and over-respond to the low energy component of large radiation fields [38]. Synthetic diamond detectors have active volumes nearly as small as silicon diodes, high sensitivity, low leakage, and high radiation hardness [39]. As is the case with ionization chambers, diodes and synthetic diamond detectors are susceptible to the same detector effects of non-water equivalence and volume averaging [40].

The PTW microDiamond detector used in this work is a synthetic diamond detector. It has an active volume embedded in a diamond crystal with a radius of 1.1 mm and length of 1  $\mu\text{m}$ . The combination of its material perturbation and volume averaging effect has been shown to require smaller off-axis perturbation corrections than the PTW microLion liquid ionization chamber [40]. In this case, the high density of materials surrounding the active volume partially compensated the over-response due to the volume averaging effect [40].

## 2.4 Summary of Chapter 2

As demonstrated in this chapter, effects caused by the presence of detectors perturb water tank measurements that attempt to measure dose to a point in water. Specifically, the effects caused by the non-water equivalence of the detector's material and its volume averaging effect were demonstrated in sections 2.2.1 and 2.2.2, respectively, for ionization chambers. The *egs\_chamber* user code was used to model several detectors in dose to water simulations, including the PTW microLion and microDiamond, Exradin A1SL and A12, and the IBA CC13, with technical details discussed in section 2.1.

Including detector models improves accuracy with measurements in the build-up region of PDDs and the penumbra region of profiles. This allows for improved accuracy in the determination of a beam model's source parameters, considering that the shape of PDDs and the penumbra region of profiles are highly dependent on a model's incident electron

energy and spot size, respectively [12]. For these reasons, detector models were included when tuning the source parameters for the Varian CL21EX model described in Chapter 3 and the FalseBEAM model of the Varian TrueBeam, described in Chapter 4.

## **Chapter 3**

# **Commissioning the source parameters of a Varian CL21EX Monte Carlo beam model**

In this chapter, the level of agreement that can be attained between dose to water measurements and Monte Carlo calculations for a Varian CL21EX linear accelerator will be demonstrated. The CL21EX was modeled in BEAMnrc of the EGSnrc Monte Carlo package [10,29]. This model was later modified to create a Varian TrueBeam model, as discussed in Chapter 4. The geometrical and material specifications for the CL21EX model were provided by Varian and included the modification to the primary collimator radii by Chibani et al. [19]. The original source parameters of this beam model (electron beam energy, spot size, and angular divergence) were not properly validated against in-house water tank data.

In order to optimally tune the beam parameters to measured water tank data, the benchmarking procedure by Almberg et al. was followed [15]. The three main steps of the procedure are to:

- 1) Tweak the incident electron beam energy to match measured and calculated 5 x 5 cm<sup>2</sup> PDDs;
- 2) Adjust the electron radial intensity (spot size) to match measured and calculated 5 x 5 cm<sup>2</sup> profiles at 10 cm depth;
- 3) Tune the mean angular spread of the incident electron beam to match measured and calculated profiles of a 30 x 30 cm<sup>2</sup> field at 10 cm depth.

Less importance was placed on matching the build-up region of PDDs and the umbra region of profiles. These regions tend to be inaccurate in commercial treatment planning systems, and are not considered clinically relevant [41,42].

### 3.1 Ionization chamber measurements

The Monte Carlo calculations were benchmarked to measurements obtained with the PTW microLion (SN 31018) liquid ionization chamber in an IBA BluePhantom<sup>2</sup> 3D water tank using the OmniPro-Accept software. The microLion was selected as a basis for tuning due to its high spatial resolution (2.5 mm diameter, 0.35 mm thick cylindrical collecting volume) and having an isooctane sensitive volume with a density near that of water, which minimizes detector perturbations. This particularly improves accuracy in the penumbra region of profiles, where sensitivity to changes in the spot size is high.

The microLion measurements were obtained with a polarizing voltage of +800V. Output factors, PDDs and profiles at 10 cm depth were taken for field sizes of 2 x 2 cm<sup>2</sup>, 3 x 3 cm<sup>2</sup>, 5 x 5 cm<sup>2</sup>, 10 x 10 cm<sup>2</sup>, 20 x 20 cm<sup>2</sup>, and 30 x 30 cm<sup>2</sup> at 100 cm SSD. All data was left unsmoothed, since smoothing was found to have a non-negligible effect on the penumbra of profiles.

Data recorded with the PTW microLion chamber was corrected for ion recombination effects following the method of Chung et al. [43], as described in equation ( 3.1 ):

$$f(Q_M) = 1 - a_{X,U}Q_M , \quad (3.1)$$

where  $f(Q_M)$  is the collection efficiency of the microLion,  $a_{X,U}$  is the coefficient of collection efficiency,  $X$  is the repetition rate,  $U$  is the polarization voltage, and  $Q_M$  is the microLion reading in nC/100 MU.

Operating at  $U = 800$  V and with a dose rate of  $X = 400$  MU/min, the coefficient of collection efficiency is  $a_{400,800} = 4.83 \times 10^{-4}$ . Coefficient of collection efficiencies were obtained by Chung et al. [43] from linear fits of measured general collection efficiency to experimental microLion readings for different dose rates and polarization voltages. The data were acquired at  $U = 800$  V because higher potentials require a smaller correction.

To apply the correction, the following steps were taken:

- i) Each output factor was corrected by computing  $f(Q_M)$  and multiplying by its inverse;
- ii) PDDs of raw experimental data were normalized to the  $10 \times 10$  cm<sup>2</sup> PDD measurement at 5 cm depth;
- iii) PDDs were then converted to absolute dose: all normalized PDDs were multiplied by the measured charge for 100 MU from a  $10 \times 10$  cm<sup>2</sup> field at 5 cm depth (7.941 nC/100 MU) and by the corrected output factor (OF) from i) for that field;
- iv) Profiles were converted to absolute dose by multiplying their raw values by the absolute depth dose values at 10 cm depth;
- vi) Each absolute depth dose and profile value was corrected by computing  $f(Q_M)$  and multiplying by its inverse;
- vii) Each PDD was renormalized to 10 cm depth and each profile was normalized to its center.

The ion recombination correction was validated by comparing corrected microLion measurements obtained using +400 V and +800 V polarizations for the 18 MV photon beam. Corrected data obtained at different polarization voltages should converge to the same values. An improvement in agreement was observed for  $10 \times 10$  cm<sup>2</sup> PDDs and  $30 \times 30$  cm<sup>2</sup> profiles (Figure 3.1).

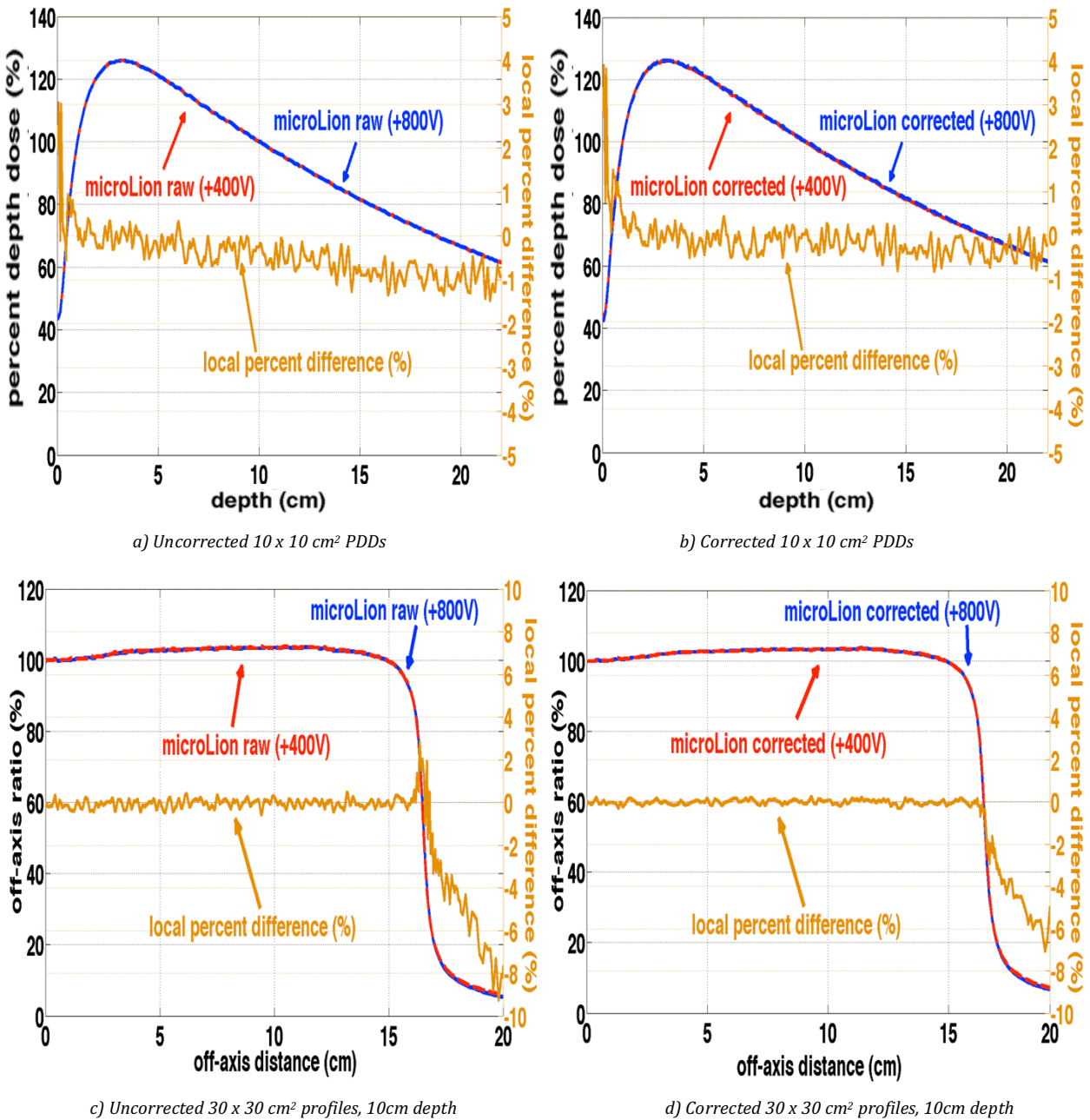


Figure 3.1: Comparisons of microLion data obtained with +400 V and +800 V potentials before and after ion recombination corrections in an 18 MV beam for a), b) 10 x 10 cm<sup>2</sup> PDDs and c), d) 30 x 30 cm<sup>2</sup> profiles at 10 cm depth.

In addition, the model was validated by comparing dose calculations to Exradin A1SL (SN XW090177) and Exradin A12 (SN 307) measurements. The same measurements were obtained as for the microLion chamber. The long axis of the collecting region was positioned in the in-plane direction.

All scans were made in continuous mode with a scan speed of 0.30 cm/s and step width of 0.5 mm. An IBA CC13 (SN 11774) was used as a reference detector for all measurements. All scans were made with the dose servo turned off in order to decrease reliance on the reference detector for mitigating short term variations in the dose rate. The linac was warmed up with 1000 MU prior to scanning.

Profiles for all chambers were centered so that 50% of the central axis (CAX) dose was equidistant on each side. All profiles were then mirrored; the average of data points equidistant on each side of the central axis were calculated and used to represent both sides of the profile. While Tessier et al. had recommended appropriate effective point of measurement PDD shifts for a number of individual chambers [44], there were no shifts made for chambers to the effective point of measurement because the comparison of dose was made to equivalent positions modeled in *egs\_chamber*.

## 3.2 BEAMnrc simulations

The Varian CL21EX BEAMnrc model was tuned to the microLion measurements described in the previous section due to its high accuracy in gradient regions. Technical details of the phantom and ionization chamber component of the simulations are outlined in section 2.1. Ion chambers were included in simulations to account for chamber perturbations discussed in section 2.2. All PDDs and profiles had 1 mm resolution with uncertainties in all scoring regions below 0.50%, with the exception of profile umbra, which were below 1.0%.

All EGSnrc physics options and regional electron and photon cutoffs (ECUT and PCUT) used in the BEAMnrc model were selected based on recommendations in the BEAMnrc manual [30]. The Koch-Motz (KM) bremsstrahlung angular sampling mode was used with NRC bremsstrahlung cross sections. Pair production angular sampling was set to “simple” with NRC pair production cross sections. Spin effects were turned on. Global ECUT and PCUT were set to 0.7 MeV and 0.01 MeV, respectively. A phase space plane normal to the beam axis was scored at 95 cm from the source for PDDs and at 100 cm for profiles. Phase space planes at 95 cm were used for PDDs to remove overlap of chambers and their XCSE shells near the surface of the water.

A 5 x 5 cm<sup>2</sup> field was used for determination of the incident electron beam energy and radial intensity. The radial intensity, or spot size, was assumed to be Gaussian using source 19 of BEAMnrc. The full-width-half-maximum (FWHM) of the distribution was used to describe the spot size in both the x and y directions. The electron beam was assumed to be monoenergetic. Using monoenergetic beams in place of an energy spectrum has been demonstrated to have little impact on PDDs and profiles [14]. A 30 x 30 cm<sup>2</sup> field was used in determination of the angular spread of the beam.

### 3.2.1 Variance reduction techniques in BEAMnrc

The variance reduction techniques (VRTs) used in BEAMnrc included directional bremsstrahlung splitting (DBS) and Russian roulette. In treatment head simulations, bremsstrahlung splitting greatly improves efficiency by creating  $N$  photons of weight  $1/N$  every time an electron has a bremsstrahlung event. In DBS, this only occurs if the bremsstrahlung photon is directed into the field of interest [26]. If the photon is not directed into the field of interest, the photon is subject to a game of Russian roulette. In Russian roulette, a random number between 0 and 1 is compared to  $1/N$ . If the random number is less than  $1/N$ , the photon is kept and its weight is multiplied by  $N$ . Otherwise, the photon is discarded. Russian roulette is also used for low interest particles, such as low energy secondary electrons.

DBS was used in all BEAMnrc simulations with a splitting number of 1000 and splitting field radii of 7 cm, 11 cm and 31 cm at 100 cm from the source for 5 x 5 cm<sup>2</sup>, 10 x 10 cm<sup>2</sup> and 30 x 30 cm<sup>2</sup> fields, respectively. An electron Russian roulette splitting plane was used below the flattening filter.

### 3.2.2 Incident electron energy

The default source parameters were an incident electron energy of 6.3 MeV, a spot size of (0.05 cm, 0 cm), and angular spread of 0°. These parameters had been used for linac Monte Carlo calculations for several years in the McGill Medical Physics Unit, but the basis for these

specific choices of parameters was unclear. As previously discussed, the procedure described by Almgren et al. first tunes the incident electron energy, followed by the spot size and angular spread [15]. The incident electron energy of the 6 MV CL21EX beam model was tuned until the agreement between calculated and measured microLion 5 x 5 cm<sup>2</sup> PDDs was optimized. The incident electron energy was varied from 5.8 MeV to 6.3 MeV in steps of 0.1 MeV, and was assumed to be monoenergetic.

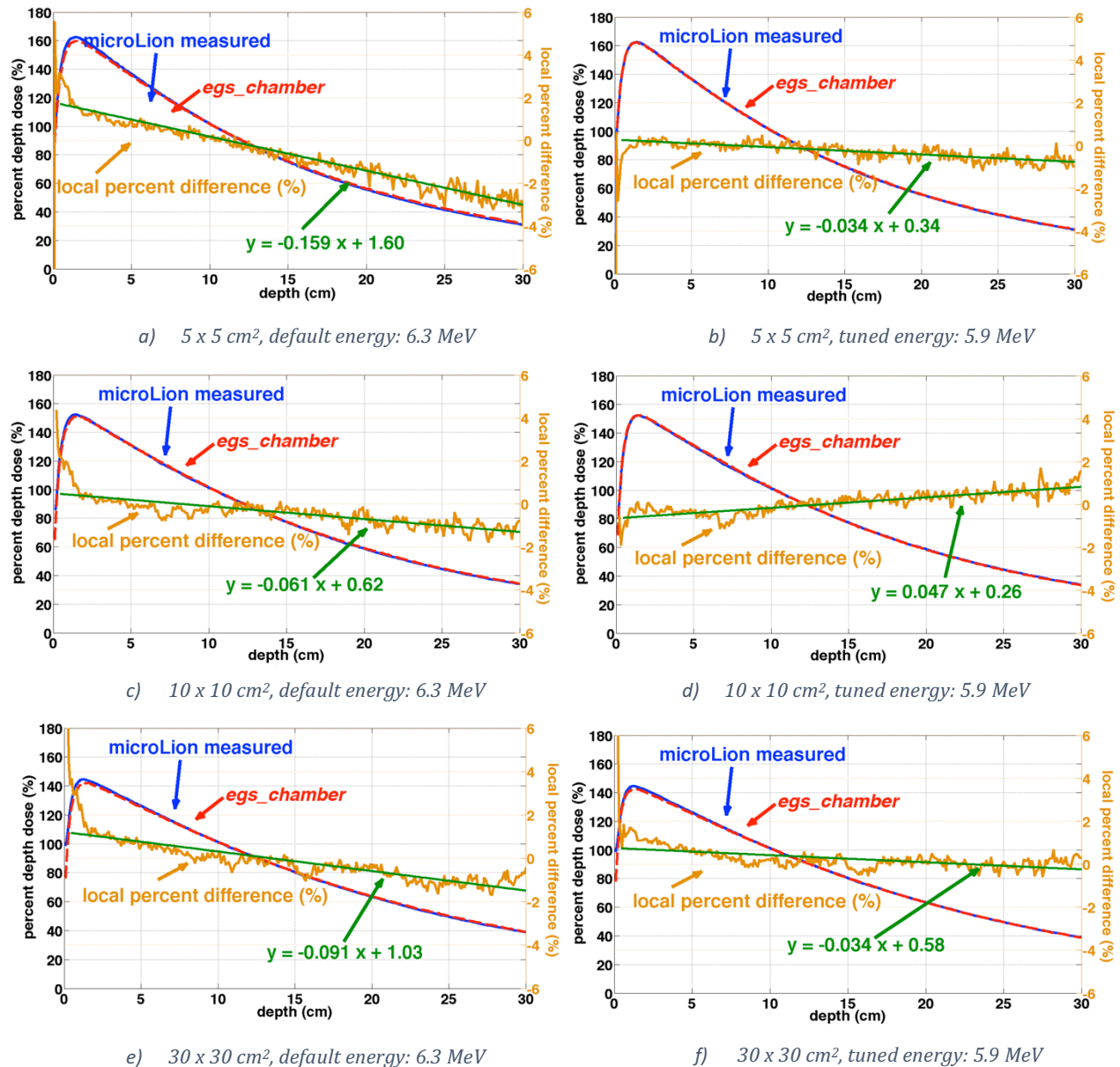


Figure 3.2: PDD comparison between the default and tuned energies of 6.3 MeV and 5.9 MeV, respectively, for a)-b) 5 x 5 cm<sup>2</sup>, c)-d) 10 x 10 cm<sup>2</sup> and e)-f) 30 x 30 cm<sup>2</sup> fields

The optimal energy was that which minimized the slope of a line of best fit of the local percent difference curve. The local percent difference between measured (Exp.) and Monte Carlo (MC) was calculated ( $= 100 \cdot (\text{Exp.} - \text{MC}) / \text{Exp.}$ ) and plotted, and a line of best fit was fitted to it in MATLAB (The MathWorks, Inc., Natick, MA). A perfect match between measured and calculated PDDs would result in a line of best fit with zero slope. Only depths beyond 0.5 cm were considered for the line of best fit. The spot size and angular spread were kept to the default values of (0.05 cm, 0 cm) and  $0^\circ$  as the incident electron energy was tuned.

A PDD comparison between the default and tuned energies of 6.3 MeV and 5.9 MeV, respectively, are shown in Figure 3.2 for  $5 \times 5 \text{ cm}^2$ ,  $10 \times 10 \text{ cm}^2$ , and  $30 \times 30 \text{ cm}^2$  fields. An incident electron energy of 5.9 MeV minimized the slope of the line of best fit for the  $5 \times 5 \text{ cm}^2$  field. The agreement was within 1.0% for depths beyond 0.5 cm, and within 2.5% between 0.1 cm and 0.5 cm depths. The tuned energy also shows an improvement over the default energy for the larger field sizes in the figure. The agreement for the tuned  $10 \times 10 \text{ cm}^2$  is within 2.0% for the first 0.2 cm and depths beyond 25 cm, and within 1.0% for all other depths. The agreement for the tuned  $30 \times 30 \text{ cm}^2$  field is within 2.0% between 0.2 cm and 2.0 cm and within 1.0% for larger depths. The agreement of the tuned PDDs is clinically acceptable because all high-dose, low-gradient regions are within 2.0% [17], and the build-up regions are within 20% [3].

### 3.2.3 Spot size

The next step in the benchmarking procedure was to tune the spot size until the best match was found between simulations and microLion data for  $5 \times 5 \text{ cm}^2$  profiles at 10 cm depth. The spot dimension along y was held fixed as the spot dimension along x was tuned and vice versa to tune the spot dimension along y. The spot size was varied in increments of 0.025 cm from 0 cm up to 0.175 cm in each direction. The optimal spot size was that which minimized the root mean square (RMS) difference between 100% and 20% off-axis ratio (%).

The profile umbra was not included in the RMS difference calculation due to the high variation of agreement in this area. Before varying the spot size, the jaw positions in BEAMnrc were incremented in steps of 0.1 mm until the calculated and measured profiles

intersected at 50% of the central axis dose to account for uncertainty in the jaw positions of the measured profiles.

To analyze profile data, three regions were defined by off-axis ratio percentage: the central region (100%-90%), penumbra region (90%-20%), and the umbra region (less than 20% to 5.0 cm off-axis). While traditionally the penumbra region is defined from 80% to 20% off-axis ratio percentage, the definition was widened to 90% in this work to allow the central region to describe only the flat region of profiles. Including 90% to 80% off-axis ratio percentage in the definition of central region would have skewed the maximum local percent difference upwards, inaccurately reflecting the agreement in the flat region of profiles.

A cross-plane comparison between the default and tuned spot size along x of 0.05 cm and 0.125 cm, respectively, is shown in Figure 3.3 for a 5 x 5 cm<sup>2</sup> field. The analogous in-plane comparison between the default and tuned spot sizes along y of 0 cm and 0.10 cm, respectively, is shown in Figure 3.4.

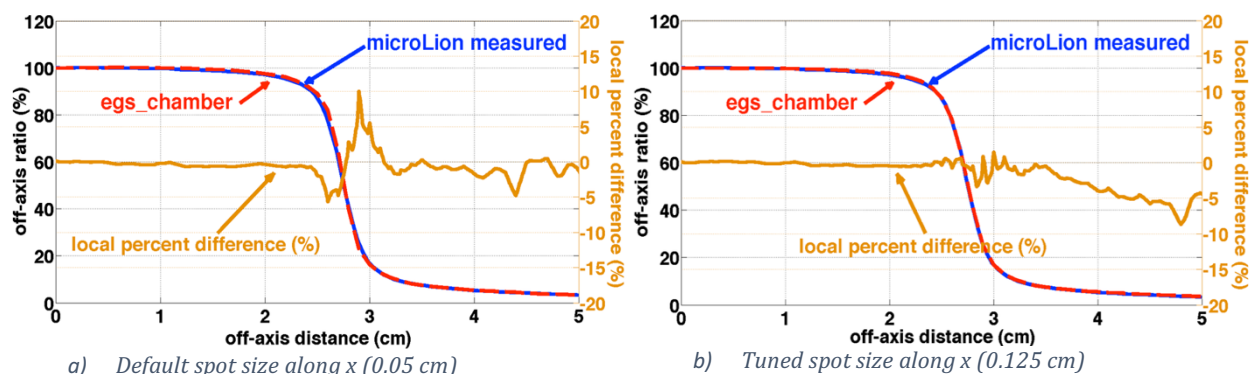


Figure 3.3: Cross-plane 5 x 5 cm<sup>2</sup> microLion measured and microLion calculated profile comparisons at 10 cm depth for a) default and b) tuned spot sizes along x.

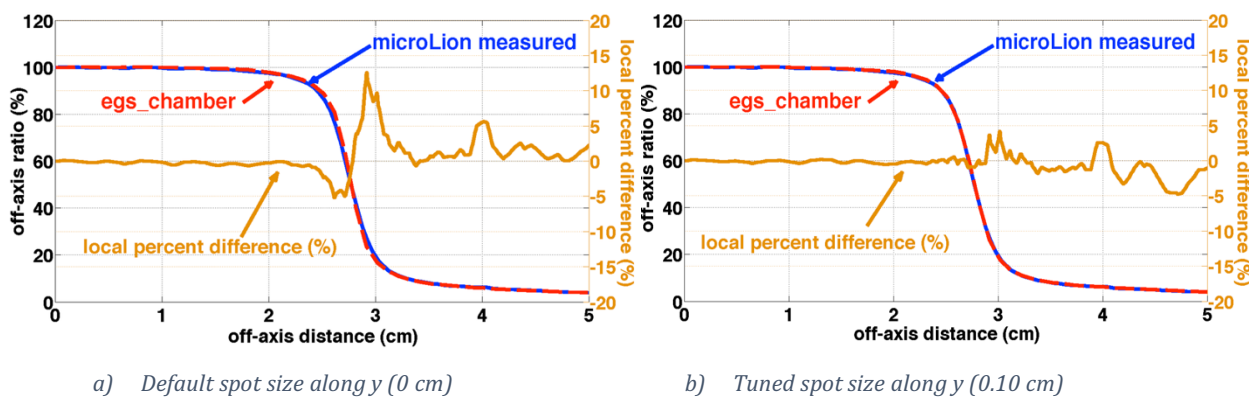


Figure 3.4: In-plane 5 x 5 cm<sup>2</sup> microLion measured and microLion calculated profile comparisons at 10 cm depth for a) default and b) tuned spot sizes along y.

As shown in Table 1, there was an improvement in agreement in the central region to within 0.6% from 1.0% for each profile direction. The agreement in the penumbra region of each profile showed improvement to within 4.9% from 13.9% in each direction. The umbra agreement decreased to within 8.6% from 6.1% local percent difference for the cross-plane profile, and improved to within 5.3% from 10.6% local percent difference for the in-plane profile. Relative to the maximum field dose, both tuned profile directions had umbra regions within 1.0%. In addition, the mean absolute local percentage differences improved for all regions in both profile directions, with the exception of the cross-plane umbra region (Table 2). Sources of discrepancy in the umbra regions are discussed in section 3.3.

The distance-to-agreement (DTA) in the penumbra region for the untuned and tuned profiles in each direction is summarized in Table 3. The maximum DTA in each profile improved from within 0.4 mm to within 0.1 mm for the untuned and tuned models, respectively.

The tuned spot size profile agreement is considered clinically acceptable because the high-dose, low gradient (central) region is within 2.0% local percent difference, the penumbra DTA is within 3 mm, and the umbra region is within 3.0% of the maximum dose.

### **3.2.4 Angular spread**

The final step in the benchmarking procedure was to tune the angular spread until the best match was found between simulations and microLion data for 30 x 30 cm<sup>2</sup> profiles at 10 cm depth. The angular spread was varied in increments of 0.025° until agreement was optimized. The optimal angular spread was that which minimized the RMS difference between 100% and 20% off-axis ratio (%), with the goal to optimize agreement in the profile shoulder, which is included in the central region. The central region, penumbra region, and umbra region are defined the same as in section 3.2.3, with the exception that the umbra region extends to 20 cm off-axis. The profile umbra was not included in the RMS difference calculation due to the high variation of agreement in this area. The jaw positions were adjusted as in the previous section before varying the angular spread.

Table 1: The maximum percent local difference in each region of  $5 \times 5 \text{ cm}^2$  profiles at 10 cm depth, with a default spot size of (0.05 cm, 0 cm) and tuned spot size (0.125 cm, 0.10 cm).

Region by off-axis ratio (%)	Cross-plane		In-plane	
	Default (0.05 cm)	Tuned (0.125 cm)	Default (0 cm)	Tuned (0.10 cm)
<b>Central</b> (100%-90%)	0.7%	0.6%	1.0%	0.6%
<b>Penumbra</b> (90%-20%)	10.8%	2.0%	13.9%	4.9%
<b>Umbra</b> (less than 20% to 5.0 cm off-axis)	6.1%	8.6%	10.6%	5.3%

Table 2: The average absolute local percent difference in each region of  $5 \times 5 \text{ cm}^2$  profiles at 10 cm depth, with a default spot size of (0.05 cm, 0 cm) and tuned spot size (0.125 cm, 0.10 cm).

Region by off-axis ratio (%)	Cross-plane		In-plane	
	Default (0.05 cm)	Tuned (0.125 cm)	Default (0 cm)	Tuned (0.10 cm)
<b>Central</b> (100%-90%)	0.4%	0.3%	0.3%	0.2%
<b>Penumbra</b> (90%-20%)	3.7%	0.7%	4.9%	1.0%
<b>Umbra</b> (less than 20% to 5.0 cm off-axis)	1.0%	3.3%	1.9%	1.8%

Table 3: Distance-to-agreement in the penumbra region (90% to 20% off-axis ratio) of  $5 \times 5 \text{ cm}^2$  profiles at 10 cm depth, with a default spot size of (0.05 cm, 0 cm) and tuned spot size (0.125 cm, 0.10 cm).

	Cross-plane		In-plane	
	Default (0.05 cm)	Tuned (0.125 cm)	Default (0 cm)	Tuned (0.10 cm)
<b>Distance-to-agreement</b>	0.3 mm	0.1 mm	0.4 mm	0.1 mm

The optimal angular spread was the same for both cross-plane and in-plane profiles. A cross-plane comparison between the default and tuned angular spread of  $0.0^\circ$  and  $0.15^\circ$ , respectively, is shown in Figure 3.5. The analogous in-plane comparison is shown in Figure 3.6. As shown in Table 4, the agreement in the central region improved from within 2.9% to within 1.2% for both profile directions, and the agreement within the penumbra improved from within 15.0% to within 8.1%. The cross-plane profile umbra agreement decreased from 3.5% with the default settings to within 6.2%, while the in-plane profile umbra agreement improved to within 3.4% from 3.7%. Relative to the maximum field dose, both tuned profile directions had umbra regions within 0.5%. In addition, the mean absolute local percentage differences improved for all regions in both profile directions, with the exception of umbra regions (Table 5). Sources of discrepancy in the umbra regions are discussed in section 3.3. The distance-to-agreement in the penumbra improved from 2.9 mm to 0.6 mm for the untuned and tuned model, respectively (Table 6). The tuned  $30 \times 30 \text{ cm}^2$  profile agreement is well within clinically recommended tolerances [17].

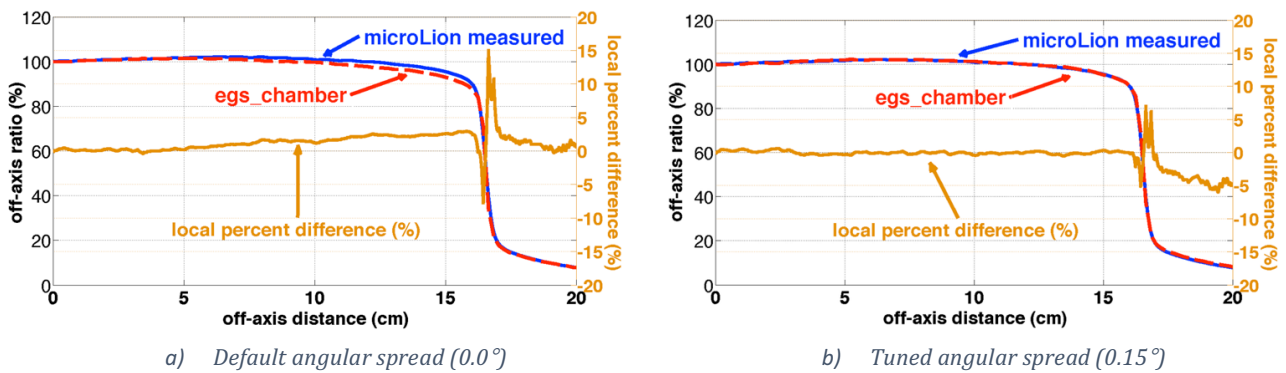


Figure 3.5: Cross-plane  $30 \times 30 \text{ cm}^2$  microLion measured and microLion calculated profile comparisons at 10 cm depth for a) default and b) tuned angular spread.

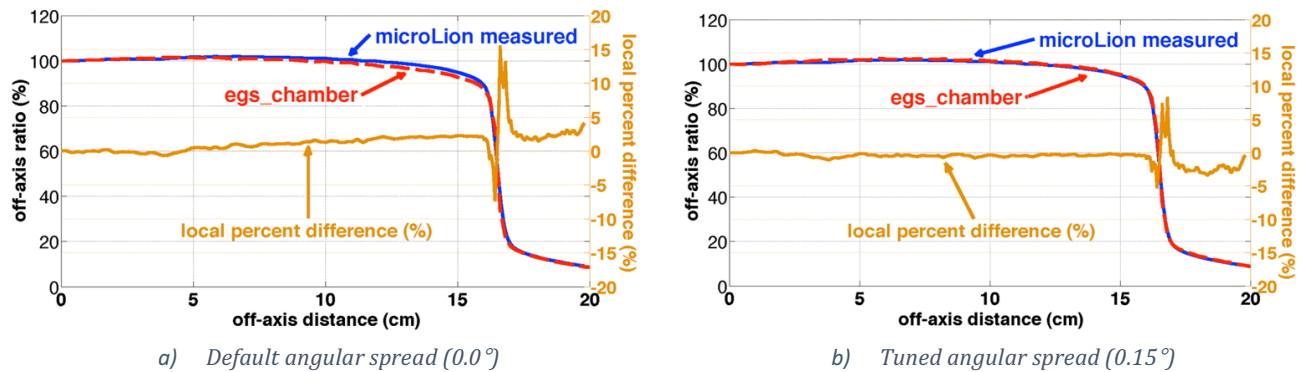


Figure 3.6: In-plane  $30 \times 30 \text{ cm}^2$  microLion measured and microLion calculated profile comparisons at 10 cm depth for a) default and b) tuned angular spread.

Table 4: The maximum percent local difference in each region of  $30 \times 30 \text{ cm}^2$  profiles at 10 cm depth, with a default and tuned angular spread of  $0.0^\circ$  and  $0.15^\circ$ , respectively.

Region	Cross-plane		In-plane	
	Default ( $0.0^\circ$ )	Tuned ( $0.15^\circ$ )	Default ( $0.0^\circ$ )	Tuned ( $0.15^\circ$ )
<b>Central</b> (100%-90%)	2.9%	0.6%	2.2%	1.2%
<b>Penumbra</b> (90%-20%)	15.0%	6.2%	13.0%	8.1%
<b>Umbra</b> (less than 20% to 20 cm off-axis)	3.5%	6.2%	3.7%	3.4%

Table 5: The average absolute local percent difference in each region of  $30 \times 30 \text{ cm}^2$  profiles at 10 cm depth, with a default and tuned angular spread of  $0.0^\circ$  and  $0.15^\circ$ , respectively.

Region by off-axis ratio (%)	Cross-plane		In-plane	
	Default ( $0.0^\circ$ )	Tuned ( $0.15^\circ$ )	Default ( $0.0^\circ$ )	Tuned ( $0.15^\circ$ )
<b>Central</b> (100%-90%)	1.2%	0.2%	1.0%	0.5%
<b>Penumbra</b> (90%-20%)	4.8%	1.9%	4.8%	2.4%
<b>Umbra</b> (less than 20% to 5.0 cm off-axis)	1.0%	4.2%	2.1%	2.7%

Table 6: Distance-to-agreement from 90% to 20% off-axis ratio of  $30 \times 30 \text{ cm}^2$  profiles at 10 cm depth, with a default and tuned angular spread of  $0.0^\circ$  and  $0.15^\circ$ , respectively.

Distance-to-agreement	Cross-plane		In-plane	
	Default ( $0.0^\circ$ )	Tuned ( $0.15^\circ$ )	Default ( $0.0^\circ$ )	Tuned ( $0.15^\circ$ )
	2.9 mm	0.4 mm	2.3 mm	0.6 mm

### 3.2.5 Validation of the tuned 6 MV CL21EX model using air-filled ionization chambers

The tuned 6 MV CL21EX model was validated with two other datasets by comparing Exradin A1SL and Exradin A12 air-filled ionization chamber measurements with calculations including their respective models. Figure 3.7 shows 5 x 5 cm<sup>2</sup> PDDs of both chambers.

The PDD agreement was within 1.0% beyond 0.4 cm and within 4.1% overall for the A1SL. The PDD agreement was within 1.0% for depths beyond 1.0 cm and within 12.6% overall for the A12. Sources of discrepancies in the buildup region are discussed in section 3.3. The agreement for both PDDs is considered clinically acceptable [3,17].

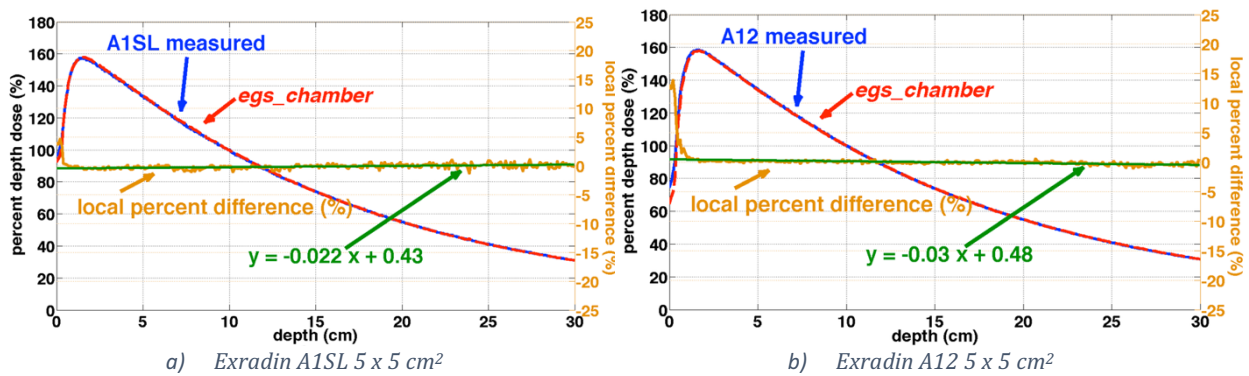


Figure 3.7: Comparison between calculated and measured 5 x 5 cm<sup>2</sup> PDDs for the a) Exradin A1SL and b) Exradin A12 air-filled ionization chambers

Figure 3.8 shows 5 x 5 cm<sup>2</sup> profiles at 10 cm depth for each chamber. The central region, penumbra region, and umbra region were defined as in section 3.2.3, with the umbra region extending to 5 cm or 20 cm off-axis for 5 x 5 cm<sup>2</sup> and 30 x 30 cm<sup>2</sup> fields, respectively.

As shown in Table 7, the agreement in the central region for both 5 x 5 cm<sup>2</sup> profile directions was within 1.1% and 1.4% for the A1SL and A12, respectively. The penumbra agreement was within 3.8% and 5.3% for the A1SL and A12 profiles, respectively. The umbra agreement was within 12.1% and 8.8% for the A1SL and A12 profiles, respectively. Relative to the maximum field dose, the A1SL and A12 had umbra regions within 1.0% and 1.1%, respectively, in both profile directions. In addition, the mean absolute local percentage differences for the A1SL and A12 in each region are shown in Table 8. Sources of discrepancy in the umbra regions are discussed in section 3.3.

The distance-to-agreement (DTA) in the penumbra region for each chamber in each direction is summarized in Table 9. The maximum DTA for both chambers was within 0.1 mm and 0.4 mm for cross-plane and in-plane  $5 \times 5 \text{ cm}^2$  profiles, respectively.

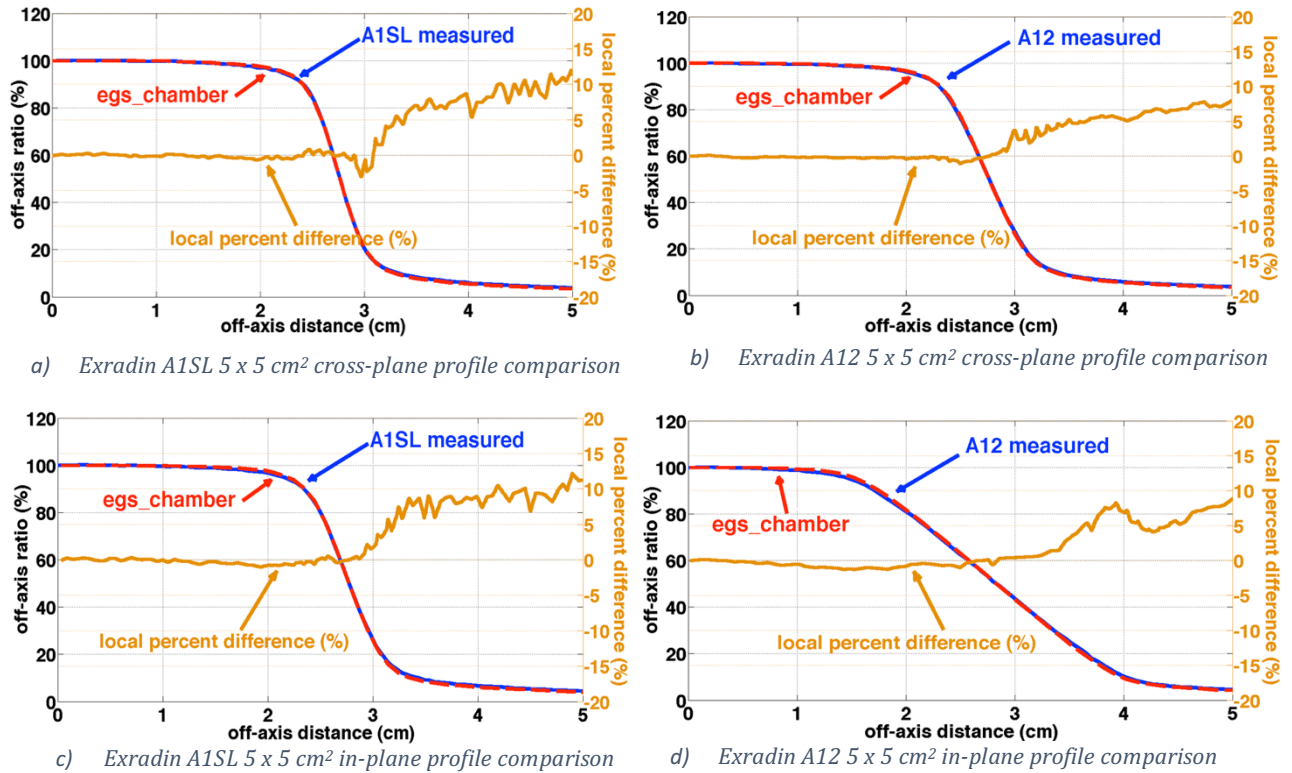


Figure 3.8: Comparison between calculated and measured  $5 \times 5 \text{ cm}^2$  a)-b) cross-plane and c)-d) in-plane profiles for the Exradin A1SL and Exradin A12 air-filled ionization chambers.

Table 7: The maximum percent local difference in each region of  $5 \times 5 \text{ cm}^2$  profiles at 10 cm depth for the Exradin A1SL and Exradin A12 air-filled ionization chambers.

Region by off-axis ratio (%)	Cross-plane		In-plane	
	Exradin A1SL	Exradin A12	Exradin A1SL	Exradin A12
Central (100%-90%)	0.7%	0.5%	1.1%	1.4%
Penumbra (90%-20%)	2.8%	3.8%	3.5%	5.3%
Umbra (less than 20%)	11.9%	7.9%	12.1%	8.8%

Table 8: The average absolute local percent difference in each region of 5 x 5 cm<sup>2</sup> profiles at 10 cm depth for the Exradin A1SL and Exradin A12 air-filled ionization chambers.

Region by off-axis ratio (%)	Cross-plane		In-plane	
	Exradin A1SL	Exradin A12	Exradin A1SL	Exradin A12
<b>Central (100%-90%)</b>	0.2%	0.2%	0.4%	0.6%
<b>Penumbra (90%-20%)</b>	0.6%	1.0%	0.7%	1.0%
<b>Umbra (less than 20%)</b>	7.4%	5.7%	8.4%	6.2%

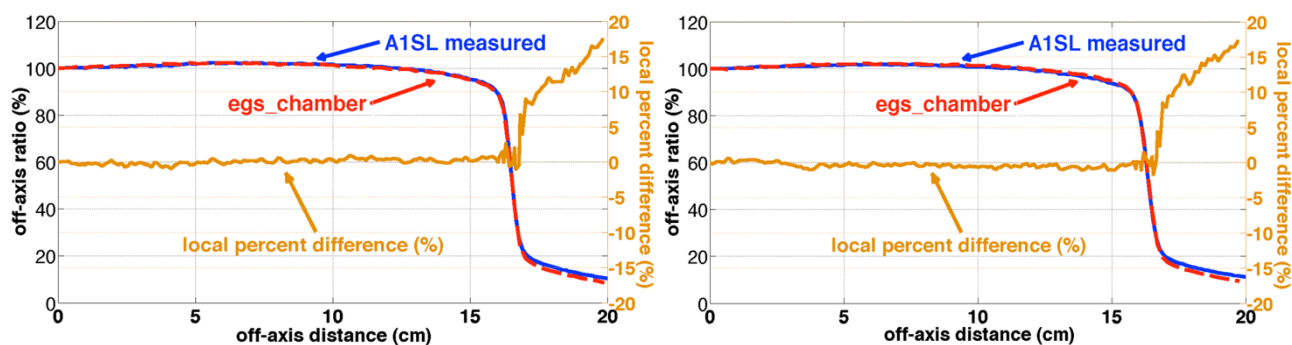
Table 9: Distance-to-agreement in the penumbra region (90% to 20% off-axis ratio) of 5 x 5 cm<sup>2</sup> and 30 x 30 cm<sup>2</sup> profiles at 10 cm depth for the Exradin A1SL and Exradin A12 air-filled ionization chambers.

Distance-to-agreement	Cross-plane		In-plane	
	Exradin A1SL	Exradin A12	Exradin A1SL	Exradin A12
<b>5 x 5 cm<sup>2</sup></b>	0.1 mm	0.4 mm	0.1 mm	0.4 mm
<b>30 x 30 cm<sup>2</sup></b>	0.5 mm	N/A*	0.4 mm	N/A*

\*30 x 30 cm<sup>2</sup> profile data for the Exradin A12 were not obtained prior to the decommissioning of the Varian CL21EX linear accelerators at the Montreal General Hospital in 2014.

Finally, Figure 3.9 shows 30 x 30 cm<sup>2</sup> profiles at 10 cm depth for the A1SL. The central region, penumbra region, and umbra region were within 1.3%, 8.9%, and 17.5%, respectively (Table 10). Relative to the maximum field dose, the umbra region was within 1.9% in both profile directions. In addition, the mean absolute local percentage differences for the A1SL and A12 in each region are shown in Table 11. Sources of discrepancy in the umbra regions are discussed in section 3.3. The distance-to-agreement from 90% to 20% off-axis ratio (%) is

within 0.5 mm for the Exradin A1SL (Table 9). The agreement for all 5 x 5 cm<sup>2</sup> and 30 x 30 cm<sup>2</sup> profiles is considered clinically acceptable.



a) Exradin A1SL 30 x 30 cm<sup>2</sup> cross-plane profile comparison      b) Exradin A1SL 30 x 30 cm<sup>2</sup> in-plane profile comparison

Figure 3.9: Comparison between calculated and measured 30 x 30 cm<sup>2</sup> a) cross-plane and b) in-plane profiles for the Exradin A1SL air-filled ionization chamber.

Table 10: The maximum percent local difference in each region of 30 x 30 cm<sup>2</sup> profiles at 10 cm depth for the Exradin A1SL air-filled ionization chamber.

Region	Cross-plane	In-plane
<b>Central</b> (100%-90%)	1.0%	1.3%
<b>Penumbra</b> (90%-20%)	8.9%	8.1%
<b>Umbr</b> (less than 20% to 5 cm off-axis)	17.5%	17.1%

Table 11: The average absolute local percent difference in each region of 30 x 30 cm<sup>2</sup> profiles at 10 cm depth for the Exradin A1SL air-filled ionization chamber.

Region	Cross-plane	In-plane
<b>Central</b> (100%-90%)	0.3%	0.6%
<b>Penumbra</b> (90%-20%)	2.4%	1.7%
<b>Umbr</b> (less than 20% to 5 cm off-axis)	12.7%	13.1%

### 3.3 The final tuned 6 MV CL21EX model

The source parameters of the 6 MV Varian CL21EX model were tuned to optimize agreement with PTW microLion water tank measurements. A microLion model was included in all dose to water simulations. The final tuned model has an incident electron energy of 5.9 MeV, spot size FWHMs of (0.125 cm, 0.10 cm), and an angular spread of  $0.15^\circ$ . The source parameters of this model were validated with two other datasets by comparing Exradin A1SL and Exradin A12 air-filled ionization chamber measurements with calculations including their respective models.

Agreement with measurements in all PDDs and profiles were well within clinically recommended tolerances [3,17]: high-dose, low-gradient regions in PDDs and profiles were within 2% local percent difference, penumbrae were within 3 mm distance-to-agreement, and profile umbra were within 3% of the maximum dose.

While overall the agreement was excellent, in some cases the local percent differences were higher in the build-up region of PDDs and the umbra region of profiles. These discrepancies could be a result of small inaccuracies in the linear accelerator model, deficiencies in the detector models, or a combination of both. These regions also tend to be inaccurate in commercial treatment planning systems, so they were not considered clinically relevant [41,42].

# Chapter 4

## Materials and methods for modeling the Varian TrueBeam

In this chapter, the materials and methods used to create a Varian TrueBeam model of the 6 MV FFF mode are described. The first method that was investigated, described in section 4.1, was to reproduce an existing PENELOPE TrueBeam model, called FakeBeam [32], in BEAMnrc. The second method that was investigated was to modify the final CL21EX model described in the previous chapter to match TrueBeam phase space data provided by Varian with identical source parameters. This model has been named FalseBEAM. Once FalseBEAM was successfully matched to Varian's phase space data, the source parameters were tuned to in-house measurements following the methods of Chapter 3.

### 4.1 FakeBeam: reproducing the work by Rodriguez et al. in BEAMnrc

The main change made by the FakeBeam authors from a 6 MV Clinac model was to swap in a bronze filter (70% copper, 30% zinc,  $\rho = 8.412 \text{ g/cm}^3$ ) in place of the 6 MV flattening filter [31]. The exact dimensions described by Rodriguez et al. were used for the 6 MV FFF filter (Figure 1.8). The FakeBeam authors were generous enough to share the exact input file,

allowing all other components of the PENELOPE FakeBeam geometry to be reproduced in BEAMnrc.

A minor approximation was made in shifting the mirror from within the shielding hole in PENELOPE to directly above it for the BEAMnrc model. Placing the mirror within the shielding hole is not currently implemented in BEAMnrc for a shielding hole above the jaws, however the presence of the mirror itself is a near-negligible effect [7]. In fact, due to design differences in the TrueBeam versus the Clinac series linacs, the mirror is no longer in the beam path during linac operation for the TrueBeam. Due to differences between Monte Carlo codes, a minor approximation was made in reproducing the exact shielding geometry above the jaws from the PENELOPE FakeBeam model.

PENELOPE FakeBeam simulations were carried out using the PRIMO Monte Carlo software [45]. PRIMO is a graphical user interface for PENELOPE simulations that includes various linac models, including the FakeBeam model for 6 MV FFF and 10 MV FFF. All default PRIMO settings for the FakeBeam model were used, which are consistent with those used in the article by Rodriguez et al. [32].

The transport parameters  $C1$  and  $C2$  in the target were set to 0.001, as recently recommended in another article by Rodriguez et al. [46].  $C1$  and  $C2$  are important parameters for the mixed condensed history technique proposed by Berger and used by PENELOPE, where a large number of collisions are combined into a single probable step to save computation time [47]. The technique classifies events into *hard* and *soft* categories based on an angular deflection cutoff angle in elastic collisions and a fractional energy loss of the step. Hard events are simulated interaction by interaction, while soft events are randomly selected at a position between hard collisions or boundaries to approximate the combined effect of multiple soft collisions.  $C1$  is interpreted as a parameter that determines the mean free path between hard elastic collisions, and consequentially, the cutoff angle that classifies hard and soft events.  $C2$  is the maximum fractional energy loss per step. Detailed simulations with  $C1$  and  $C2$  not greater than 0.001 in the linac target were recommended due to variations in dose being observed with larger values [46]. The splitting-roulette variance reduction technique was used with the largest splitting field.

To evaluate agreement between the PENELOPE FakeBeam model and the BEAMnrc FakeBeam model, the fluence and spectra of the phase spaces output at 26.7 cm from the target entrance plane were compared (section 4.2). This required transporting the FakeBeam phase space from  $Z = 26.0$  cm through 7 mm of air in BEAMnrc using an ECUT and PCUT of 0.512 MeV and 0.01 MeV, respectively. The FakeBeam phase space was generated in PRIMO with a Gaussian mean electron energy of 5.8 MeV and a FWHM of 0.058 MeV. The spot size FWHM was 0.15 cm in each direction, with an angular spread of  $0^\circ$ . The source parameters, including the Gaussian spectrum, were reproduced in the BEAMnrc version.

## 4.2 Analyzing phase spaces with BEAMDP

Phase space files were compared using BEAMDP of the EGSnrc system, which is compatible with both IAEA and EGSnrc formats [48]. To generate fluence or spectra profiles, an annulus was taken radially from 0 cm to 7 cm. The fluence per incident electron was calculated in 200 bins, including all particle types. The phase space spectra, in fluence per MeV per incident electron, was plotted for energies from 0 MeV to 6 MeV in 200 energy bins, including all particle types. An additional spectral distribution was plotted between 0 MeV and 1 MeV with 200 energy bins to compare lower energies.

## 4.3 FalseBEAM

FalseBEAM was the second method investigated to model the Varian TrueBeam, created by reproducing generic phase space data (available on myvarian.com) released by Varian for the 6 MV FFF energy model. The generic phase space data were used over phase space data generated by the Virtualinac since the generic phase space data have been validated independently from Varian to have good agreement in dose to water [32]. As discussed in section 1.4, phase spaces generated on the Virtualinac require validation with each update, and fluence profile differences were observed between generic phase spaces and phase

spaces generated on the VirtuaLinac with the same source parameters and updated recommended settings (Figure 1.5).

The TrueBeam phase space data were generated using source parameters that were tuned by Varian to match the TrueBeam representative dataset, which was an average of measured data from three linear accelerators obtained with the IBA CC13 ionization chamber [22,23]. The Geant4 model used by Varian had a Gaussian mean electron energy of 5.9 MeV with a sigma of 0.051 MeV, a Gaussian spot size with sigmas of 0.6645 mm and 0.7274 mm in the cross-plane and in-plane directions, respectively, and an angular divergence given by a Gaussian with a sigma of 1 mrad. In Varian's tuning process, the spot size was measured [24].

Varian's phase space data were generated with a range cut of 10  $\mu\text{m}$  using Geant4 version geant4-09-04-patch-02 with the QGSP\_BIC\_EMY physics list. Of the 54 TrueBeam phase space files of 940 MB for 6 MV FFF currently available on myvarian.com, 42 were combined to create one 40 GB phase space. This large phase space required 27.3 billion original histories to produce approximately 2.0 billion particles at the phase space plane above the jaws. No variance reduction techniques were used. The Varian phase space data was in IAEA format [49].

FalseBEAM was matched to the TrueBeam phase space using the same source parameters that Varian had used in their model. As in Varian's TrueBeam model, the spot size in BEAMnrc was characterized by Gaussians with sigmas in the cross-plane and in-plane direction.

The 6 MV Varian CL21EX BEAMnrc model from Chapter 3 was used as a starting point for the geometrical and material variations. The field mirror was removed, as it is not in the TrueBeam's path, and the monitor chamber was kept constant due to its negligible attenuation in photon beams [7]. A back-scatter filter was added above the shielding hole. The dimensions and materials of the flattening filter, back-scatter filter, and target layers, as well as the primary collimator radii and target position were varied in a trial and error process to match the fluence and spectra at 26.7 cm from the entrance surface of the target. The phase space was output by BEAMnrc in EGSnrc format [30]. The details of how the phase spaces were compared and analyzed is found in section 4.2.

The electron cutoff ECUT and photon cutoff PCUT were set to 0.512 MeV and 0.01 MeV, respectively. No electron Russian roulette splitting plane was used. Otherwise, all BEAMnrc physics options and variance reduction techniques used for FalseBEAM simulations are identical to those used in section 3.2.

### 4.3.1 Dose to water calculations including detector models

Once the phase spaces were considered matched, dose to water calculations including detector models were made using *egs\_chamber*. Technical parameters of all *egs\_chamber* simulations were previously discussed in section 2.1. In an ideal scenario where FalseBEAM could perfectly reproduce the TrueBeam phase space, it would have equivalent agreement with the TrueBeam representative data in dose to water calculations, considering that was the basis for Varian's TrueBeam model optimization. For this reason, the matched FalseBEAM model was verified to have good agreement in dose to water calculations compared with the TrueBeam representative data.

A CC13 model was included in *egs\_chamber* calculations to validate the untuned FalseBEAM model since the representative beam data were obtained using the IBA CC13. With no 5 x 5 cm<sup>2</sup> fields available in the representative beam data, 10 x 10 cm<sup>2</sup> PDDs and profiles were used.

Once good agreement was shown in dose to water calculations for the TrueBeam representative data, the source parameters of FalseBEAM were tuned to in-house 6 MV FFF measurements following the methods of section 3.2. Measurements from a PTW microDiamond diamond detector were used as basis for tuning due to its high spatial resolution, and consequently microDiamond models were included in all *egs\_chamber* calculations. Once the model was tuned, it was validated with calculations including the CC13 model against in-house CC13 measurements.

The FalseBEAM BEAMnrc model required the addition of several components for the dose to water calculations, including: jaws, baseplate, MLCs, and a thin Mylar film. These components were modeled according to the Varian Monte Carlo Data Package distributed

for the Varian TrueBeam. For the tuning process, the spot size was characterized by cross-plane and in-plane FWHMs. This initially required a conversion from sigma using

$$FWHM = 2\sqrt{2\ln 2}\sigma. \quad (4.1)$$

The spot size was then tuned in steps of 0.25 mm in each direction.

### 4.3.2 Water tank measurements for 6 MV FFF

PTW microDiamond (SN 122378) and IBA CC13 (SN 12704) measurements were made in an IBA Blue Phantom<sup>2</sup> 3D water tank. The microDiamond was selected as a basis for tuning the source parameters due to its high spatial resolution (2.2 mm diameter, 0.001 mm long cylindrical collecting volume). This improves accuracy in the penumbra region of profiles, where sensitivity to changes in the spot size is high. The microDiamond is a synthetic diamond diode detector; no voltage is required. Its low energy dependence adds reliability in the profile umbra. The CC13 air-filled ionization chamber was used for validation of the beam model.

PDDs and profiles at 10 cm depth were taken for each detector with field sizes of 5 x 5 cm<sup>2</sup>, 10 x 10 cm<sup>2</sup> and 30 x 30 cm<sup>2</sup> at 100 cm SSD. All data were left unsmoothed, since smoothing was found to have a non-negligible effect on the penumbra of profiles. There were no shifts made to the effective point of measurement because the comparison of dose was made to equivalent positions modeled in *egs\_chamber*.

The OmniPro-Accept water tank software was used for all scanning measurements. For the microDiamond 5 x 5 cm<sup>2</sup> fields, the gradient mode scanning technique was used in the build-up region of PDDs and profile penumbra to create smoother profiles without the need for artificial smoothing. The in-scan positioning speed was 0.10 cm/s. A small step size of 0.2 mm was used. The measurement time for each step was set to 5.0 s. All other scans were made in continuous mode with a scan speed of 0.30 cm/s and step width of 0.5 mm. All scans were made with the dose servo turned off. A CC13 (SN 12705) chamber was used as a reference detector for all measurements.

In addition, output factors were measured using both the microDiamond and the CC13 at 5 cm depth. Integrated charge readings were recorded for 200 MU irradiations for field sizes of 2 x 2 cm<sup>2</sup>, 3 x 3 cm<sup>2</sup>, 5 x 5 cm<sup>2</sup>, 10 x 10 cm<sup>2</sup>, 20 x 20 cm<sup>2</sup> and 30 x 30 cm<sup>2</sup>.

# Chapter 5

## Results from Varian TrueBeam models

### 5.1 FakeBeam

An unnormalized and normalized fluence comparison between the PENELOPE and BEAMnrc FakeBeam phase spaces alongside generic TrueBeam phase spaces above the jaws is shown in Figure 5.1. The non-zero location of the first bin, and subsequent uneven bin sizes as a function of radial off-axis distance, is implemented to keep the area of the concentric rings constant for each bin. The normalized plot shows that the relative agreement between the PENELOPE version of FakeBeam and the TrueBeam phase space is excellent, as one would expect, but that the BEAMnrc implementation has discrepancies.

The unnormalized plots show reasonable overall agreement between the PENELOPE and BEAMnrc implementations of FakeBeam, but with disagreements along the central region and at the field edge. The latter discrepancy is a result of slight differences in the shielding implementations. The agreement at the field edge of the fluence profile is considered of minor importance in this work considering that the jaws will attenuate this region, with the exception of very large fields.

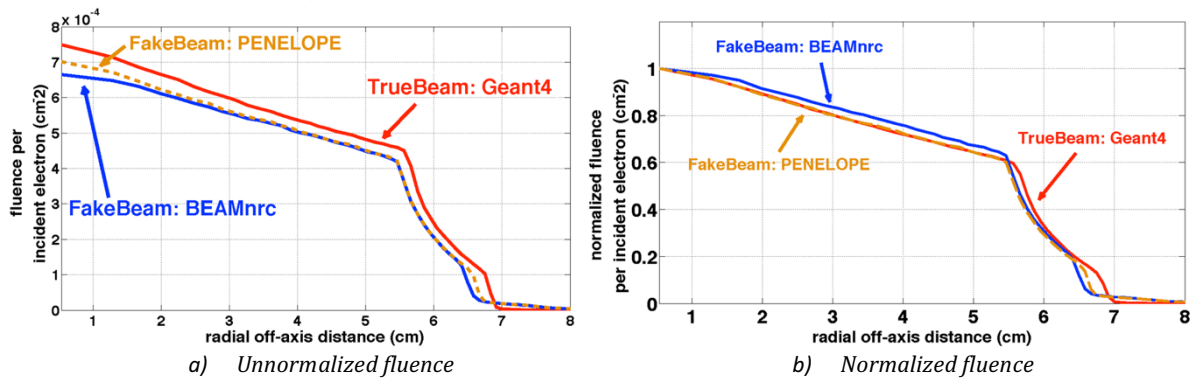


Figure 5.1: Comparison of a) unnormalized and b) normalized phase space fluence (relative to maximum) above the jaws between the EGSnrc and PENELOPE implementations of FakeBeam, in addition to the generic Varian TrueBeam Geant4 phase space.

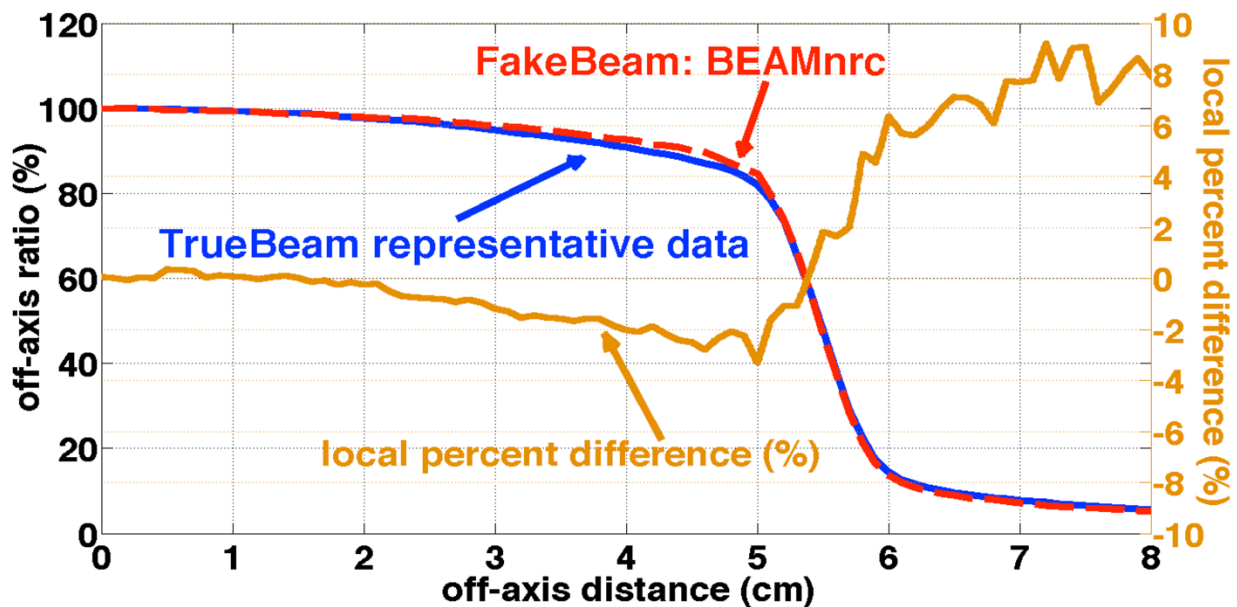


Figure 5.2: An *egs\_chamber* CC13 simulation of a  $10 \times 10 \text{ cm}^2$  profile at 10 cm depth, using the BEAMnrc FakeBeam model. Differences in fluence between implementations of FakeBeam propagates to a discrepancy in dose to water.

The disagreement in fluence in the central region was of primary concern, considering that it propagated to a dose to water discrepancy in the shoulder of a  $10 \times 10 \text{ cm}^2$  profile at 10 cm depth between the TrueBeam representative data and an *egs\_chamber* simulation that included a CC13 model (Figure 5.2). The PENELOPE FakeBeam implementation has been demonstrated to have excellent agreement with the TrueBeam representative data [32]. The difference in fluence along the central region is explained by differences between the EGSnrc and PENELOPE Monte Carlo codes, specifically the bremsstrahlung angular sampling algorithms.

As discussed in section 4.1, it is critical to have set the proper transport parameters in the target for PENELOPE simulations to accurately simulate bremsstrahlung production. The PENELOPE simulations from the fluence comparison in Figure 5.1 used the detailed transport parameters  $C1 = C2 = 0.001$ , as recommended [46]. The agreement between BEAMnrc and PENELOPE was much greater if the PENELOPE simulation is less detailed, as shown in Figure 5.3 with  $C1 = C2 = 0.1$ . Rodriguez et al. demonstrated that less detailed settings, i.e. larger values of  $C1$  and  $C2$ , create a small bias on the angular distribution of bremsstrahlung photons after observing differences in dose to water profiles from a simple tungsten target setup when varying these transport parameters [46].

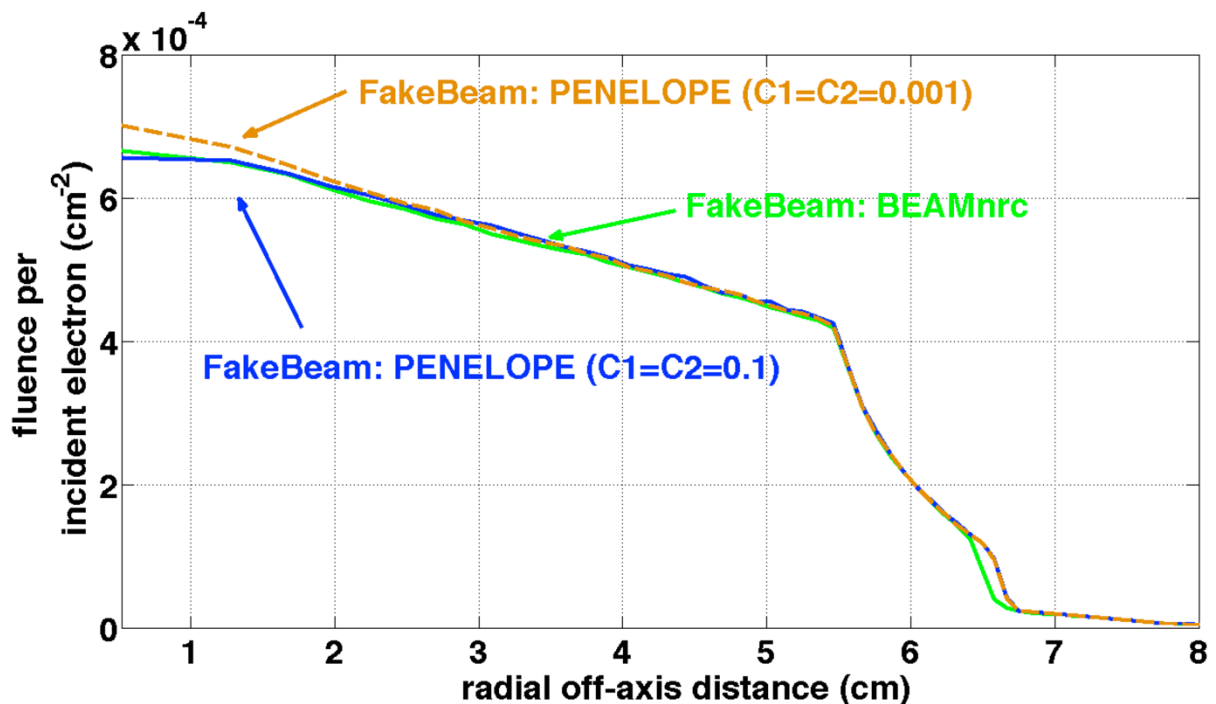


Figure 5.3: Comparison of unnormalized phase space fluence above the jaws between the PENELOPE FakeBeam model simulated using the recommended detailed transport parameters  $C1=C2=0.001$  and the less detailed  $C1=C2=0.1$  in the target, plotted alongside the BEAMnrc implementation of FakeBeam.

There are no direct equivalents of  $C1$  and  $C2$  in EGSnrc, because the manner in which EGSnrc implements multiple scattering theory differs from that of PENELOPE. By default, the EGSnrc parameter “skin depth for boundary crossing algorithm (BCA)” is 3. This indicates that when an electron is at a default distance of three elastic mean free paths from a boundary, the algorithm switches into single-scattering mode, making the simulation

independent of electron step length. For this reason, the detailed PENELOPE fluence with  $C1=C2=0.001$  cannot be reproduced in EGSnrc by modifying the step length. To demonstrate this, the fluence comparing FakeBeam run in single-scattering mode compared to FakeBeam with default settings is shown in Figure 5.4. BEAMnrc was run in single-scattering mode by setting “skin depth for BCA” to  $10^{10}$ .

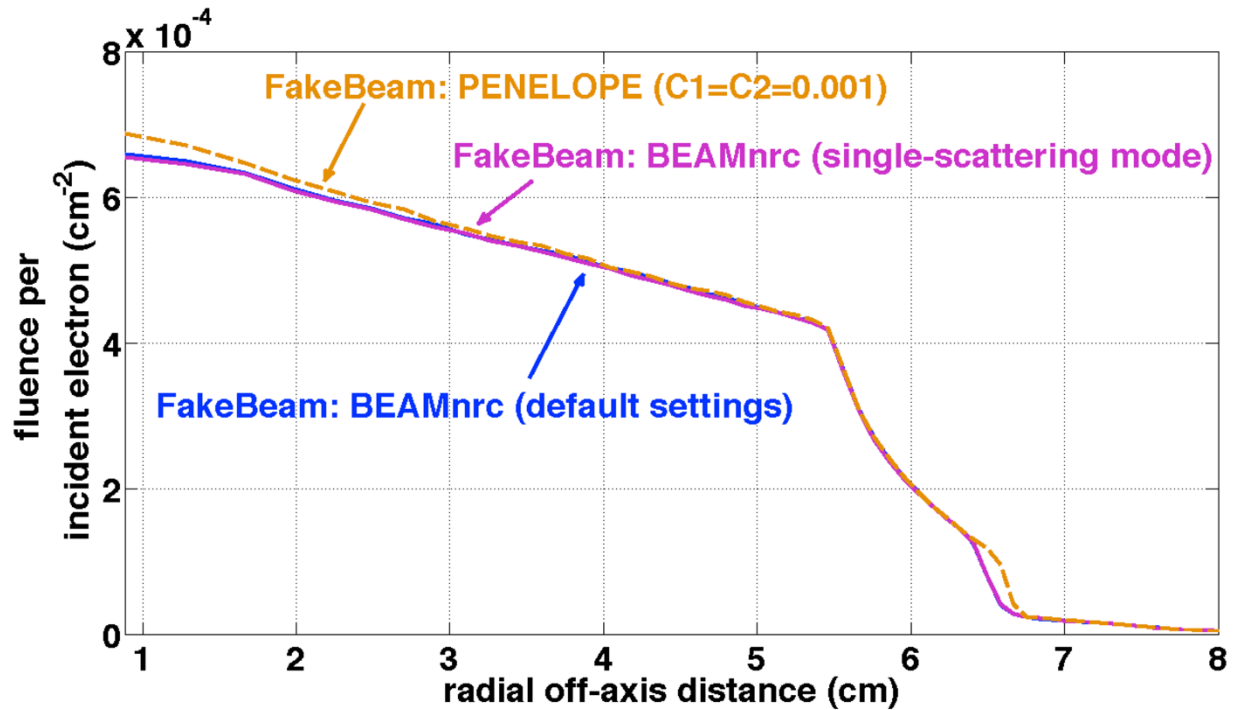


Figure 5.4: Comparison of unnormalized phase space fluence above the jaws between the BEAMnrc FakeBeam model simulated with default transport parameters and in single-scattering mode, plotted alongside the PENELOPE implementation of FakeBeam with transport parameters  $C1=C2=0.001$ .

To verify that the source of the discrepancy was due to differences between codes, the aforementioned radial dose profiles from the simple tungsten target setup described by Rodriguez et al. [46] were reproduced using BEAMnrc as a shared library source with DOSRZnrc. A 0.05 cm thick cylindrical tungsten target ( $\rho = 18.0 \text{ g/cm}^3$ ) with a radius of 0.25 cm was separated from the surface of a 20 cm thick water phantom by an air gap of 99.95 cm. The cylindrical air gap and cylindrical water phantom had a radius of 30 cm. The source consisted of a monoenergetic pencil beam with an incident electron energy of 6.26 MeV. The tungsten target and air gap were simulated in BEAMnrc; the water phantom was simulated in DOSRZnrc. To eliminate any electrons emerging from the target, an electron ECUT of 10.511 MeV (including rest mass) was used in the air gap. The electron cutoff ECUT

in the target and water phantom were set to 611 keV. The photon cutoff PCUT was set to 20 keV in the target, air slab, and water phantom.

Rodriguez et al. [46] observed that the radial dose profiles at 1.5 cm depth in this setup were dependent on choice of the transport parameters  $C1$  and  $C2$  in the target, and recommended values of  $C1=C2=0.001$  based on where the radial dose profiles converged with the most detailed simulation in the study, which used  $C1=C2=0$  with interaction forcing (IF) equal to 100. Interaction forcing is a variance reduction technique used in PENELOPE that increases radiative interactions by artificially increasing the cross section and compensating with a decreased statistical weight [46]. In terms of accuracy, it has the same effect as decreasing the step size.

Using the profile data from this study that was graciously provided by Rodriguez et al., a comparison of the equivalent setup in BEAMnrc is shown in Figure 5.5. The figure includes BEAMnrc simulations run with default settings, in single-scattering mode by setting “skin depth for BCA” to  $10^{10}$ , and by changing the bremsstrahlung angular sampling algorithm from “KM” to “simple.” The latter simulation was the only setting to have a significant impact on the dose profiles, and while it does not reproduce the PENELOPE result, it adds to suspicions that the discrepancies are a result of differences in the bremsstrahlung angular sampling algorithms between codes. The approximately 5% discrepancy between the default EGSnrc profile and the detailed ( $C1=C2=0$ , IF=100) PENELOPE profile has a similar magnitude to the discrepancy in fluence along the central axis between default BEAMnrc and PENELOPE FakeBeam implementations (Figure 5.4).

Factors that did not significantly affect the BEAMnrc dose profile included: using other available bremsstrahlung cross sections, setting the “analogous”  $C1$  and  $C2$  parameters ESTEPE and XIMAX to their lower limits, and changing the pair production angular sampling algorithm. As seen in the figure, running BEAMnrc in single-scattering mode also did not have a significant effect on the dose profile.

Determining which bremsstrahlung angular sampling algorithm is more correct is beyond the scope of this work. While it may be surprising that PENELOPE and BEAMnrc have significant differences in dose to water calculations despite having equivalent beam geometries with equivalent source parameters, it is reasonable to suggest that these

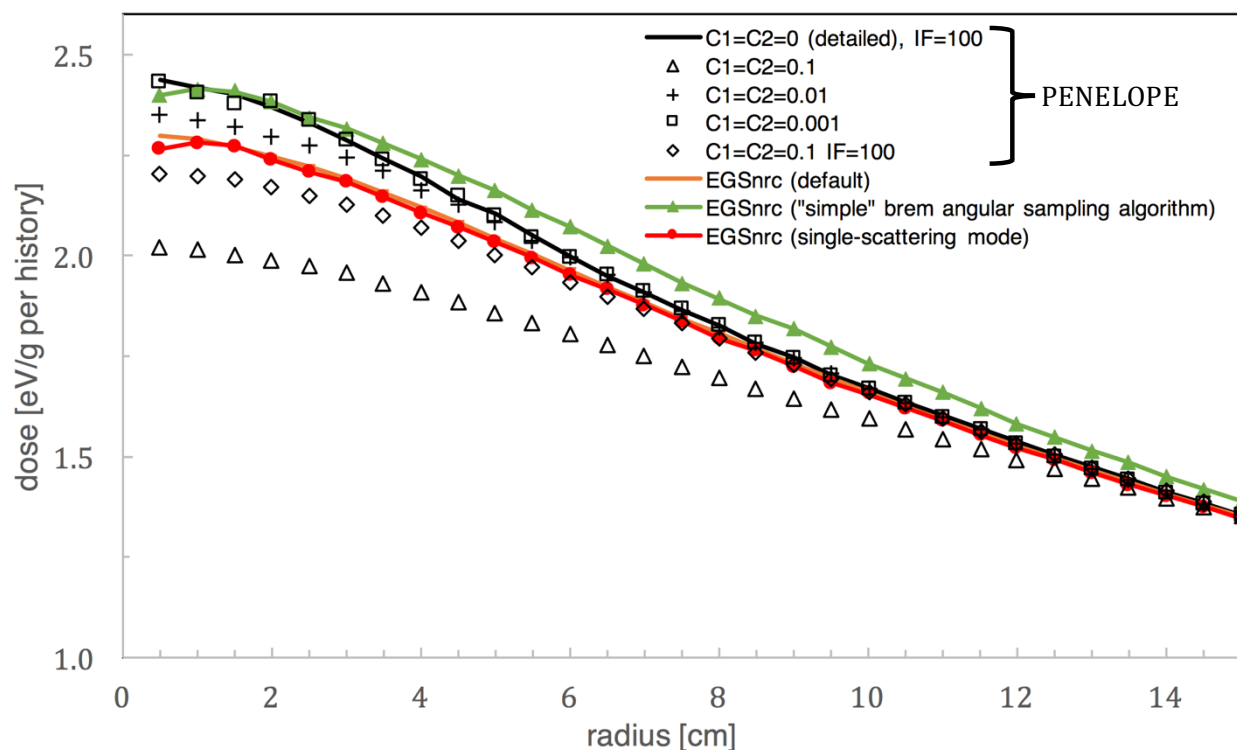


Figure 5.5: Comparison of radial dose profiles at 1.5 cm depth as PENELOPE transport parameters  $C1$  and  $C2$  were varied, and for various EGSnrc transport parameters. IF stands for interaction forcing. PENELOPE simulation data was reproduced from the work by Rodriguez et al. [46] with permission.

differences are not usually detected because a user's choice of source parameters can easily blur out the problem.

From this point, FakeBeam was abandoned as a method for modeling the Varian TrueBeam in favour of the method used to create FalseBeam (section 4.3). However, in principle one could likely achieve good agreement in dose to water with the BEAMnrc implementation of FakeBeam either by varying the source parameters or the thicknesses of the brass filter layers.

## 5.2 FalseBEAM: phase space matching

The FalseBEAM BEAMnrc model matched to phase space data is shown in Figure 5.6. The main differences compared to the Varian CL21EX model are a flat brass filter in place of the

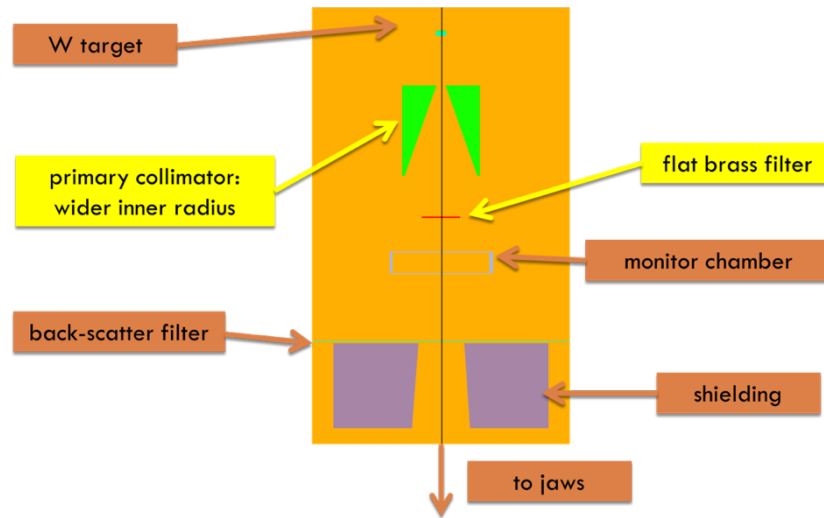


Figure 5.6: FalseBEAM model in BEAMnrc. The dimensions in the figure are not to scale.

6 MV flattening filter and the primary collimator having wider entrance and exit radii. The location of the target was shifted, removed from vacuum, and minor adjustments were made to the thickness of tungsten and its heat dissipation layer. A thin copper back-scatter filter was placed above the shielding hole. The monitor chamber and shielding was kept constant in the model.

The FalseBEAM phase space was matched to normalized TrueBeam fluence and spectra plots. Matching to the unnormalized phase space led to unrealistic geometries, and differences in the magnitude of fluence could be explained by differences between Geant4 and EGSnrc. Additionally, a change in the magnitude of fluence was observed between Varian's TrueBeam models using different versions of Geant4. As previously shown in Figure 1.7, the magnitude of the fluence in TrueBeam phase spaces was significantly lower when generated on the VirtuaLinac compared to the phase spaces distributed by Varian. This discrepancy was previously explained by the changed bremsstrahlung cross sections in the newer version of Geant4 that was used to generate the VirtuaLinac phase space [27]. This variability in the magnitude of fluence was an additional reason that the FalseBEAM phase space was matched to normalized fluence and spectra plots.

A comparison of unnormalized and normalized fluence between TrueBeam and FalseBEAM phase spaces above the jaws is shown in Figure 5.7. A comparison of the spectra between TrueBeam and FalseBEAM phase spaces is shown in Figure 5.8 and Figure 5.9 in

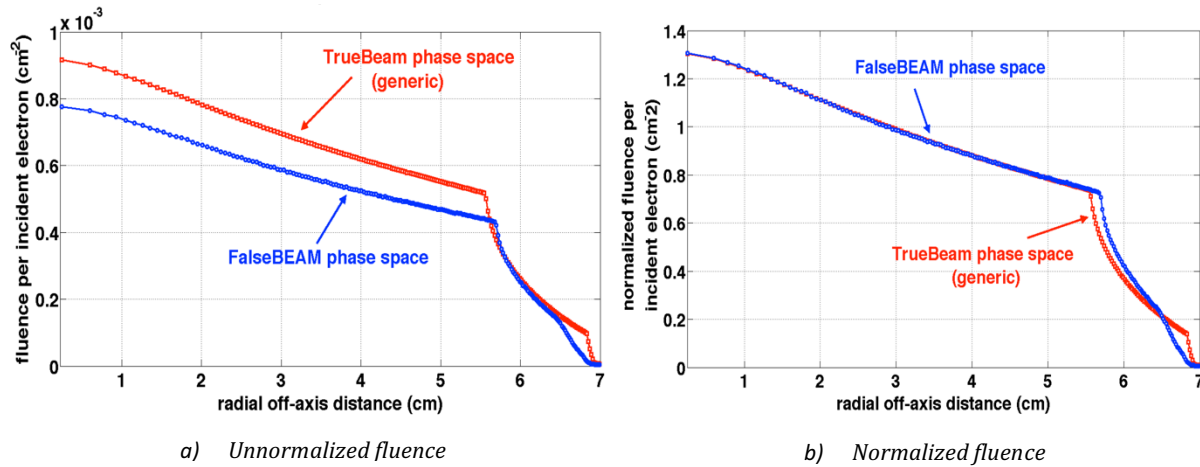


Figure 5.7: FalseBEAM vs. TrueBeam comparison of phase space a) unnormalized and b) normalized fluence, relative to approximately 3 cm radial off-axis distance, above the jaws.

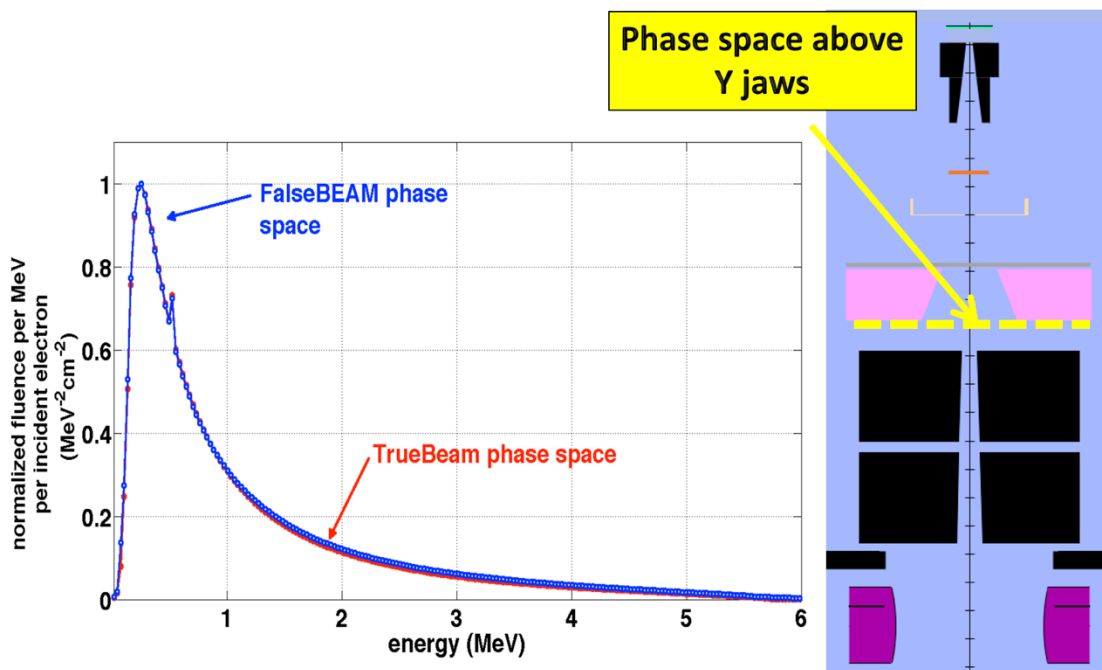


Figure 5.8: FalseBEAM vs. TrueBeam comparison of normalized phase space spectra, relative to the maximum fluence, above the jaws from 0 MeV to 6 MeV. The dimensions in the FalseBEAM figure are not to scale.

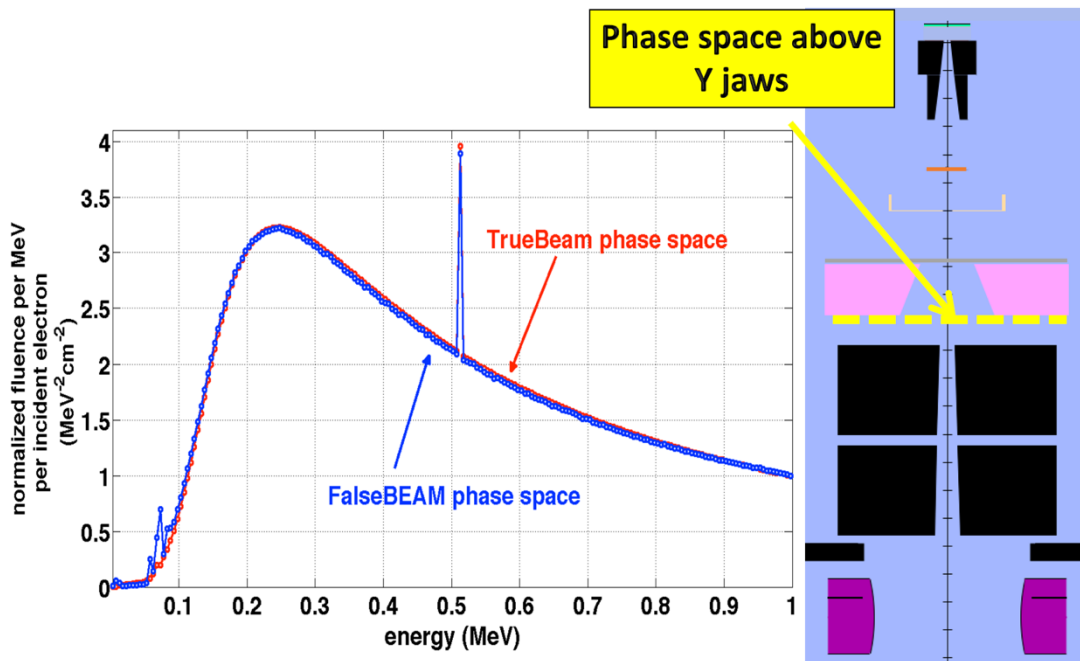


Figure 5.9: FalseBEAM vs. TrueBeam comparison of normalized phase space spectra, relative to the fluence at 1 MeV, above the jaws from 0 MeV to 1 MeV. The dimensions in the FalseBEAM figure are not to scale.

the range of 0 MeV to 6 MeV and 0 MeV to 1 MeV, respectively. For all fluence and spectra plots, the normalization points were selected in an arbitrary fashion.

Overall, normalized fluence agreement is excellent, with a discrepancy in the shoulder of the profile close to 5.5 cm off-axis. Considering that the jaws will attenuate most of this region, it is considered a minor discrepancy, with the exception of very large fields (e.g. 40 x 40 cm<sup>2</sup>). Although changes in the shielding geometry could correct the profile edge, it was not changed because the rest of the fluence profile was observed to be very sensitive to even minor changes in the model.

The overall normalized spectra phase space agreement was good at energies above 1 MeV, and excellent at energies below 1 MeV. Characteristic peaks below 100 keV were only observed in the FalseBEAM phase space due to Varian's model having higher energy cutoffs.

## 5.3 FalseBEAM: dose to water calculations

With the FalseBEAM model able to reasonably reproduce the TrueBeam phase space with generic source parameters, it is expected to have excellent agreement in dose to water calculations with the TrueBeam representative dataset that the source parameters of Varian's TrueBeam model were tuned to. The TrueBeam representative dataset was measured with the IBA CC13 ionization chamber. Once this agreement is verified, the tuning results with the PTW microDiamond will be shown, followed by validation of the tuned model with in-house CC13 measurements.

### 5.3.1 Agreement of the untuned FalseBEAM model with TrueBeam representative data

Measurements are compared to 10 x 10 cm<sup>2</sup> PDD and profile calculations that include a CC13 model in the simulation in Figure 5.10. Past the first 2 mm, the PDD agreement is within 1.7%. For depths up to 2 mm, where the chamber is not fully submerged, the agreement is within 7.6%.

As in section 3.2.3, 3 regions were defined by off-axis ratio percentage: the central region (100%-90%), penumbra region (90%-20%), and the umbra region (less than 20% to 10.0 cm off-axis). The maximum local percent difference in the central, penumbra, and umbra regions is within 0.5%, 2.6%, and 6.4%, respectively. Sources of discrepancy in the

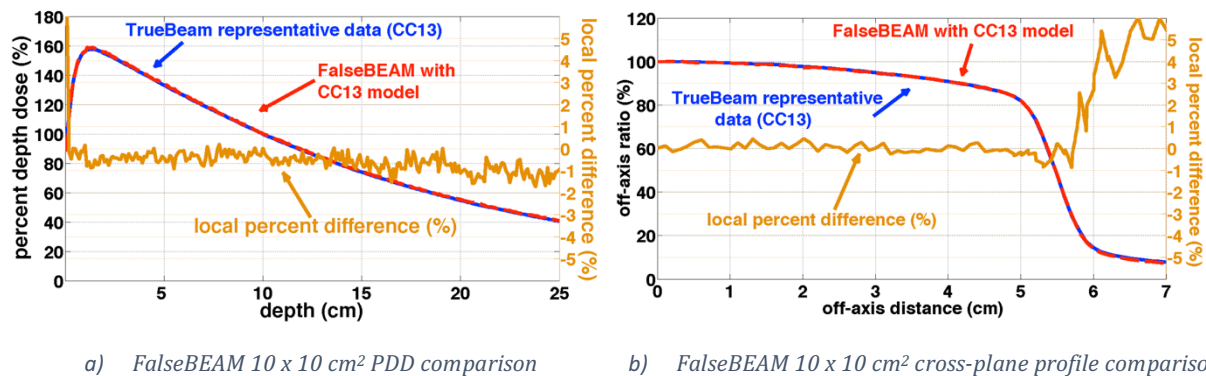


Figure 5.10: Comparison between a calculated and measured 10 x 10 cm<sup>2</sup> a) PDD and b) profile at 10 cm depth using the FalseBEAM model for the IBA CC13 TrueBeam representative data.

umbra region are discussed in section 5.3.4. Relative to the maximum field dose, the umbra region is within 0.7%. The distance-to-agreement in the penumbra region is within 0.4 mm.

### 5.3.2 FalseBEAM model tuning simulations benchmarked by PTW microDiamond measurements

Following the methods of section 3.2, the source parameters were then tuned to in-house PTW microDiamond measurements. The incident electron energy was tuned to a monoenergetic 5.8 MeV beam from a Gaussian spectrum with an average energy of 5.9 MeV and sigma of 0.051 MeV to match the measured 5 x 5 cm<sup>2</sup> PDD (Figure 5.11) by minimizing the slope of a line of best fit that begins beyond 5 mm depth. Beyond 2 mm, the agreement is within 1.1%. The overall agreement, including the surface dose, is within 7.6%.

The PDD agreement for 10 x 10 cm<sup>2</sup> and 30 x 30 cm<sup>2</sup> fields with the tuned incident electron energy are shown in Figure 5.12. For the 10 x 10 cm<sup>2</sup> field, the agreement is within 1.0% beyond the first 3 mm, and within 10.1% overall. For the 30 x 30 cm<sup>2</sup> field, the agreement is within 1.8% beyond 1 mm, and within 10.0% at the surface.

The spot size was tuned to match 5 x 5 cm<sup>2</sup> profiles at 10 cm depth (Figure 5.13). FWHM spot dimensions of 1.31 mm and 1.21 mm were selected in the cross-plane and in-

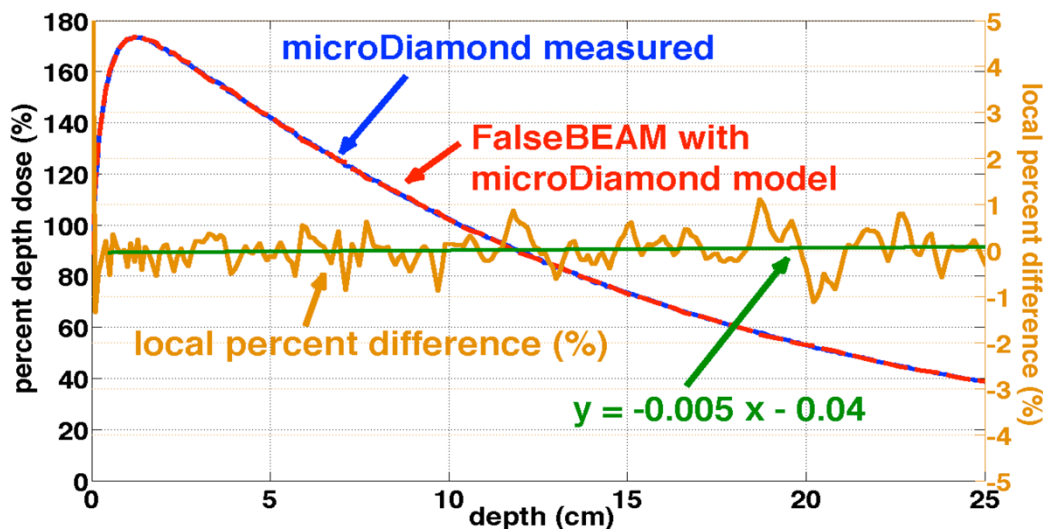


Figure 5.11: PDD comparison for 5 x 5 cm<sup>2</sup> fields with a tuned FalseBEAM incident electron energy of 5.8 MeV against microDiamond measurements. A microDiamond model was included in the dose to water calculation.

plane directions, respectively, from the respective untuned sigma spot dimensions of 0.6645 mm (FWHM = 1.56 mm) and 0.7274 mm (FWHM = 1.71 mm).

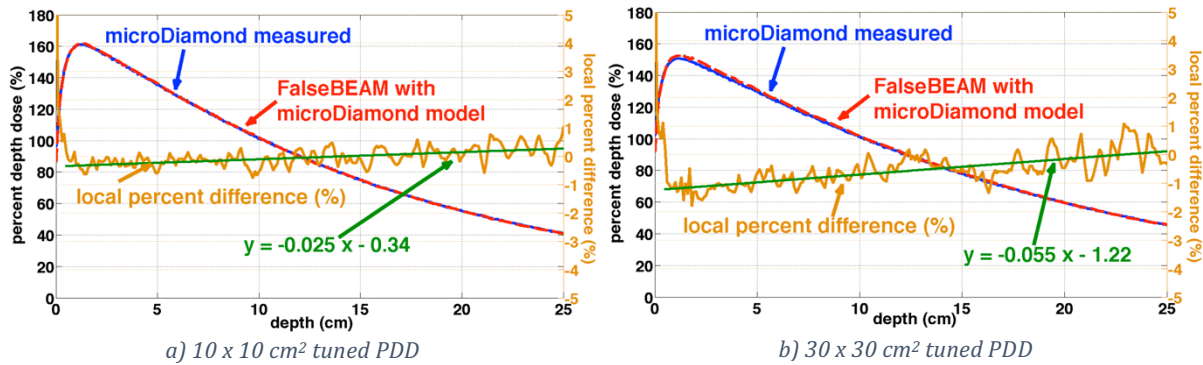


Figure 5.12: PDD comparison for a)  $10 \times 10 \text{ cm}^2$  and b)  $30 \times 30 \text{ cm}^2$  fields with a tuned FalseBEAM incident electron energy of 5.8 MeV against microDiamond measurements. A microDiamond model was included in the calculation.

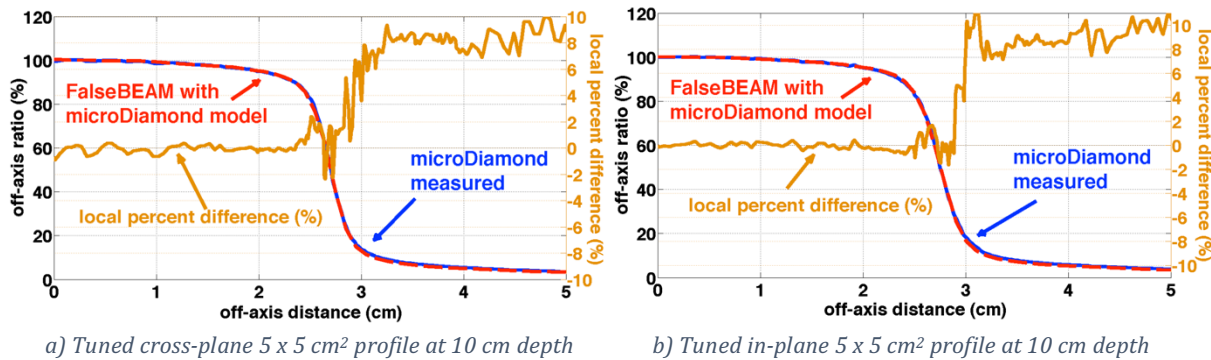


Figure 5.13: Tuned comparison of a) cross-plane and b) in-plane  $5 \times 5 \text{ cm}^2$  microDiamond measured and microDiamond calculated profiles at 10 cm depth for FalseBEAM with a tuned spot size FWHM of (1.31 mm, 1.21 mm).

To evaluate the  $5 \times 5 \text{ cm}^2$  profiles, the same definitions of central region, penumbra region, and umbra region as the previous section apply, with the exception that the umbra region now extends to 5 cm off-axis. As shown in Table 12, the agreement in the central region with microDiamond measurements for both  $5 \times 5 \text{ cm}^2$  profile directions was within 0.9%. The penumbra and umbra regions were within 4.6% and 11.7%, respectively. In addition, the mean absolute local percentage differences in each region are shown in Table 13. Sources of discrepancy in the umbra region are discussed in section 5.3.4. Relative to the maximum field dose, the umbra region in both profile directions is within 1.8%. The DTA in the penumbra region in each profile direction was within 0.4 mm (Table 14).

Table 12: The maximum percent local difference in each region of 5 x 5 cm<sup>2</sup> profiles at 10 cm depth for the PTW microDiamond detector..

Region by off-axis ratio (%)	Cross-plane	In-plane
<b>Central (100%-90%)</b>	0.9%	0.6%
<b>Penumbra (90%-20%)</b>	4.4%	4.6%
<b>Umbra (less than 20%)</b>	10.0%	11.7%

Table 13: The mean absolute percent local difference in each region of 5 x 5 cm<sup>2</sup> profiles at 10 cm depth for the PTW microDiamond detector..

Region by off-axis ratio (%)	Cross-plane	In-plane
<b>Central (100%-90%)</b>	0.2%	0.2%
<b>Penumbra (90%-20%)</b>	1.2%	1.2%
<b>Umbra (less than 20%)</b>	7.9%	8.9%

Table 14: Distance-to-agreement in the penumbra region (90% to 20% off-axis ratio) of 5 x 5 cm<sup>2</sup> profiles at 10 cm depth for the PTW microDiamond detector..

	Cross-plane	In-plane
<b>Distance-to-agreement</b>	0.4 mm	0.4 mm

An angular spread of 1 mrad was found to optimize agreement between measured and calculated 30 x 30 cm<sup>2</sup> profiles at 10 cm depth (Figure 5.14). This angular spread was in agreement with the angular divergence used in Varian's TrueBeam model. Separate region

definitions were given to evaluate the  $30 \times 30 \text{ cm}^2$  profiles due to the unique shape of large flattening filter free profiles; the central region was defined as from 100% to 60% off-axis ratio (%), the penumbra region from 60% to 20% off-axis ratio (%), and the umbra region was defined as having less than 20% off-axis ratio (%) to 20 cm off-axis.

As shown in Table 15, the agreement in the central region with microDiamond measurements for both  $30 \times 30 \text{ cm}^2$  profile directions was within 0.9%. The penumbra and umbra regions were within 5.2% and 24.7%, respectively. In addition, the mean absolute local percentage differences in each region are shown in Table 16. Sources of discrepancy in the umbra region are discussed in section 5.3.4. Relative to the maximum field dose, the umbra region in both profile directions is within 1.9%. The DTA in the penumbra region in each profile direction was within 0.6 mm (Table 17).

The final tuned 6 MV FFF FalseBEAM model of the Varian TrueBeam has an incident electron energy of 5.8 MeV, spot size FWHMs of (1.31 mm, 1.21 mm), and an angular spread of 1 mrad. All microDiamond PDDs and profiles were within clinically recommended tolerances [3,17].

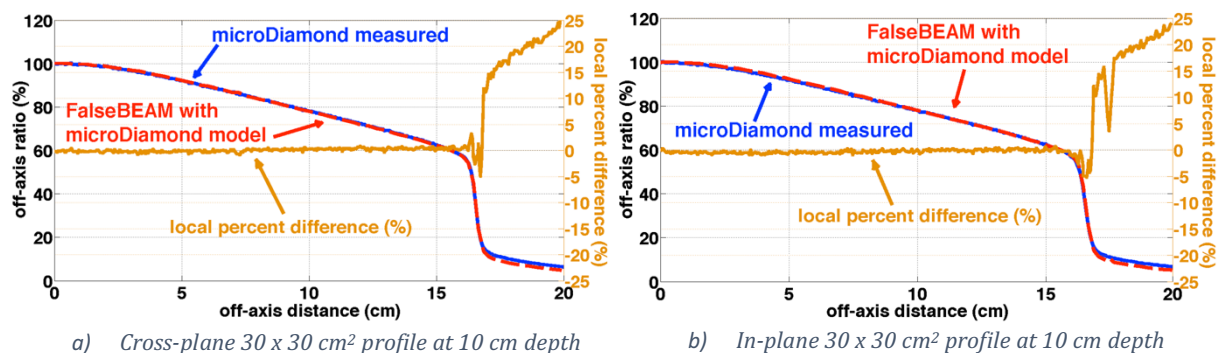


Figure 5.14: Tuned comparison of a) cross-plane and b) in-plane  $30 \times 30 \text{ cm}^2$  microDiamond measured and microDiamond calculated profiles at 10 cm depth for FalseBEAM with a tuned angular spread.

Table 15: The maximum percent local difference in each region of 30 x 30 cm<sup>2</sup> profiles at 10 cm depth for the PTW microDiamond detector..

Region by off-axis ratio (%)	Cross-plane	In-plane
<b>Central</b> <b>(100%-60%)</b>	0.9%	0.9%
<b>Penumbra</b> <b>(60%-20%)</b>	4.0%	5.2%
<b>Umbra</b> <b>(less than 20% to 20 cm off-axis)</b>	24.7%	23.9%

Table 16: The mean absolute local percent difference in each region of 30 x 30 cm<sup>2</sup> profiles at 10 cm depth for the PTW microDiamond detector..

Region by off-axis ratio (%)	Cross-plane	In-plane
<b>Central</b> <b>(100%-60%)</b>	0.3%	0.3%
<b>Penumbra</b> <b>(60%-20%)</b>	1.1%	1.7%
<b>Umbra</b> <b>(less than 20% to 20 cm off-axis)</b>	18.5%	17.4%

Table 17: Distance-to-agreement in the penumbra region (60% to 20% off-axis ratio) of 30 x 30 cm<sup>2</sup> profiles at 10 cm depth for the PTW microDiamond detector..

	Cross-plane	In-plane
<b>Distance-to-agreement</b>	0.5 mm	0.6 mm

### 5.3.3 Validation of tuned FalseBEAM with in-house CC13 measurements

The tuned FalseBEAM model was validated by comparing in-house CC13 measurements with FalseBEAM calculations that include a CC13 model. Figure 5.15 shows a  $5 \times 5 \text{ cm}^2$  comparison of measured and calculated PDDs. The agreement is within 1.8% beyond the first 5 mm, with only two points greater than 1.0%. The agreement at the surface was 7.0%.

The disagreement at depths less than 5 mm is relatively large compared to the microDiamond agreement. The likely source of error lies with the measurement; the CC13 was observed to have strange behaviour as it emerged from the water after taking several measurements. A possible explanation for this behaviour is the effect of the chamber holder also coming out of the water, which was not included in the chamber model. Further investigation would be required to confirm the source of the discrepancy.

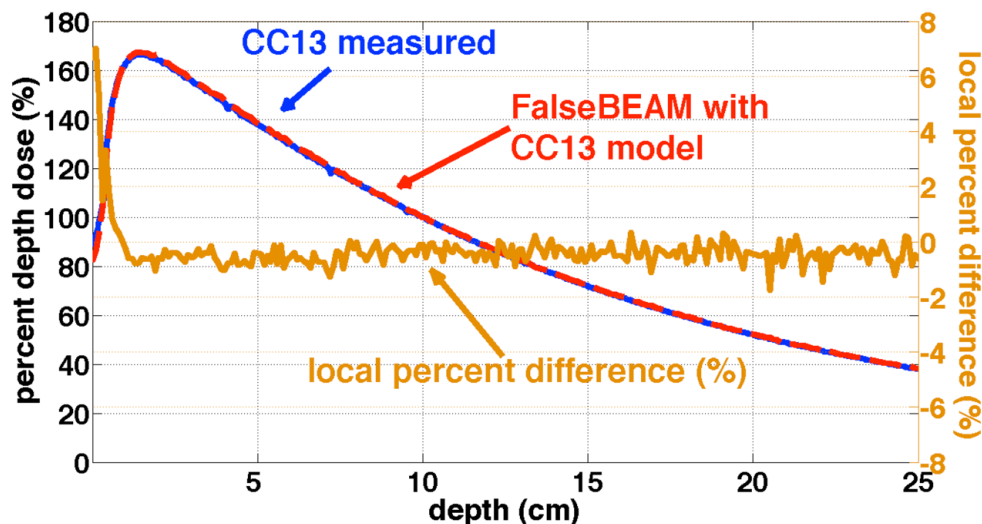


Figure 5.15:  $5 \times 5 \text{ cm}^2$  PDD comparison of measured CC13 data with a tuned FalseBEAM simulation that includes a CC13 model.

Figure 5.16 shows cross-plane and in-plane  $5 \times 5 \text{ cm}^2$  profiles at 10 cm depth. As shown in Table 19, the agreement in the central region with CC13 measurements for both  $5 \times 5 \text{ cm}^2$  profile directions was within 0.6%. The penumbra and umbra regions were within 4.5% and 6.4%, respectively. Sources of discrepancy in the umbra region are discussed in section 5.3.4. Relative to the maximum field dose, the umbra region in both profile directions is within 0.7%. In addition, the mean absolute local percentage differences in each region are

shown in Table 19. The DTA in the penumbra region in each profile direction was within 0.2 mm (Table 20).

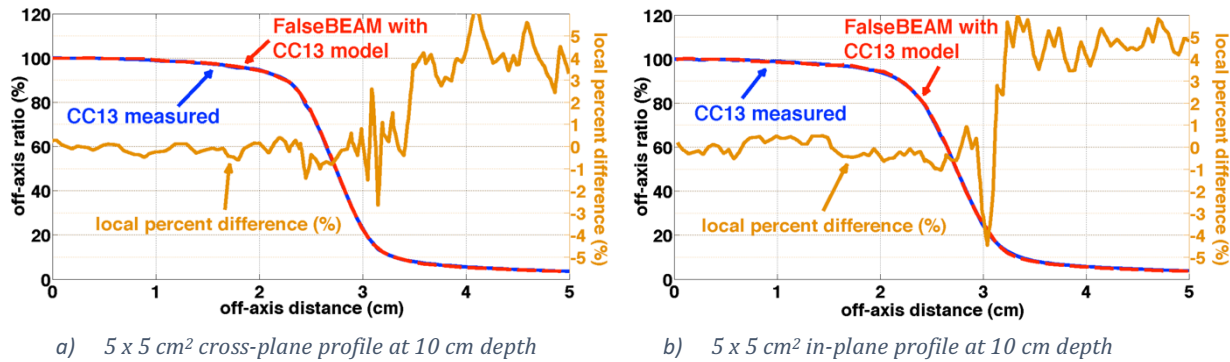


Figure 5.16: 5 x 5 cm<sup>2</sup> a) cross-plane and b) in-plane profile comparison at 10 cm depth of measured CC13 data with a tuned FalseBEAM simulation that includes a CC13 model.

Table 19: The maximum percent local difference in each region of 5 x 5 cm<sup>2</sup> profiles at 10 cm depth for the IBA CC13 air-filled ionization chamber.

Region by off-axis ratio (%)	Cross-plane	In-plane
<b>Central (100%-90%)</b>	0.6%	0.6%
<b>Penumbra (90%-20%)</b>	1.4%	4.5%
<b>Umbra (less than 20%)</b>	6.4%	6.0%

Table 18: The mean absolute local percent difference in each region of 5 x 5 cm<sup>2</sup> profiles at 10 cm depth for the IBA CC13 air-filled ionization chamber.

Region by off-axis ratio (%)	Cross-plane	In-plane
<b>Central (100%-90%)</b>	0.2%	0.2%
<b>Penumbra (90%-20%)</b>	0.7%	0.8%
<b>Umbra (less than 20%)</b>	4.3%	4.6%

Table 20: Distance-to-agreement in the penumbra region (90% to 20% off-axis ratio) of  $5 \times 5 \text{ cm}^2$  profiles at 10 cm depth for the IBA CC13 air-filled ionization chamber.

	Cross-plane	In-plane
<b>Distance-to-agreement</b>	0.2 mm	0.2 mm

Finally, Figure 5.17 shows  $30 \times 30 \text{ cm}^2$  profiles at 10 cm depth. As shown in Table 21, the agreement in the central region with CC13 measurements for both  $30 \times 30 \text{ cm}^2$  profile directions was within 1.8%. The penumbra and umbra regions were within 2.6% and 10.8%, respectively. Sources of discrepancy in the umbra region are discussed in section 5.3.4. Relative to the maximum field dose, the umbra region in both profile directions is within 0.9%. In addition, the mean absolute local percentage differences in each region are shown in Table 22. The DTA in the penumbra region in each profile direction was within 0.3 mm (Table 23).

Overall, the FalseBEAM agreement with CC13 measurements was excellent. All CC13 PDDs and profiles were within clinically recommended tolerances [3,17].

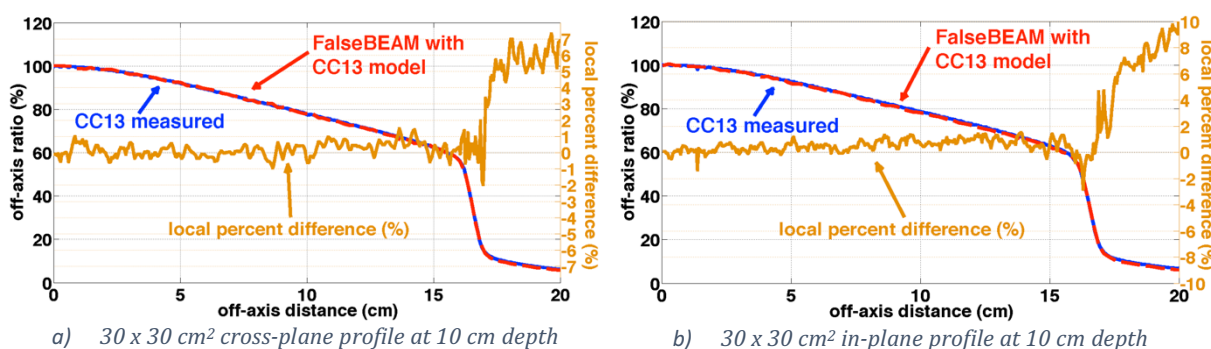


Figure 5.17:  $30 \times 30 \text{ cm}^2$  a) cross-plane and b) in-plane profile comparison at 10 cm depth of measured CC13 data with a tuned FalseBEAM simulation that includes a CC13 model.

Table 21: The maximum percent local difference in each region of 30 x 30 cm<sup>2</sup> profiles at 10 cm depth for the IBA CC13 ionization chamber.

Region by off-axis ratio (%)	Cross-plane	In-plane
<b>Central (100%-60%)</b>	1.8%	1.5%
<b>Penumbra (60%-20%)</b>	1.5%	2.6%
<b>Umbra (less than 20% to 20 cm off-axis)</b>	7.3%	10.8%

Table 22: The mean absolute local percent difference in each region of 30 x 30 cm<sup>2</sup> profiles at 10 cm depth for the IBA CC13 ionization chamber.

Region by off-axis ratio (%)	Cross-plane	In-plane
<b>Central (100%-60%)</b>	0.4%	0.6%
<b>Penumbra (60%-20%)</b>	0.4%	0.5%
<b>Umbra (less than 20% to 20 cm off-axis)</b>	5.3%	6.7%

Table 23: Distance-to-agreement in the penumbra region (60% to 20% off-axis ratio) of 30 x 30 cm<sup>2</sup> profiles at 10 cm depth for the IBA CC13 ionization chamber.

	Cross-plane	In-plane
<b>Distance-to-agreement</b>	0.3 mm	0.3 mm

### 5.3.4 The final tuned FalseBEAM model

The final tuned 6 MV FFF FalseBEAM model of the Varian TrueBeam has an incident electron energy of 5.8 MeV, spot size FWHMs of (1.31 mm, 1.21 mm), and an angular spread of 1 mrad. The source parameters of this model were validated with CC13 air-filled ionization chamber measurements using calculations that included detector models.

Agreement with both microDiamond and CC13 measurements in all PDDs and profiles were well within clinically recommended tolerances [3,17]: high-dose, low-gradient regions in PDDs and profiles were within 2% local percent difference, penumbra were within 3 mm distance-to-agreement, profile umbra were within 3% of the maximum dose, and the build-up regions were within 20% local percent difference.

While overall the agreement was excellent, in some cases the local percent differences were higher in the build-up region of PDDs and the umbra region of profiles. These discrepancies could be a result of small inaccuracies in the linear accelerator model, deficiencies in the detector models, or a combination of both. These regions also tend to be inaccurate in commercial treatment planning systems, so they were not considered clinically relevant [41,42].

The larger discrepancy in the umbra region of 30 x 30 cm<sup>2</sup> profiles compared to 5 x 5 cm<sup>2</sup> profiles could have a contribution from the discrepancy at the edge of the fluence profile when matching the TrueBeam phase space (Figure 5.7). This is only a problem for large fields because this area is otherwise collimated by the jaws. Additional possible sources of error are inaccuracies in the FalseBEAM model, the CC13 model not properly modeling the chamber's energy dependence, or a combination of both. We do not have any feasible method to independently verify the geometric accuracy of the FalseBEAM model since that information is confidential.

Inaccuracies in either or both of the CC13 or microDiamond detectors are possible, given the large difference in maximum umbra region disagreement for 30 x 30 cm<sup>2</sup> profiles: 10.8% vs. 24.7% local percent difference, respectively. This difference is much smaller in the case of 5 x 5 cm<sup>2</sup> fields, with a maximum local percent difference of 6.4% vs. 4.6% for the CC13 and microDiamond, respectively.

Another source of error in the umbra is the approximation made with the jaw orientation of jaw movement. In the FalseBEAM model, the jaws open perpendicular to the beam axis, while in reality, the jaws swing open on an arc. This feature is not easily implemented in BEAMnrc. To improve agreement in the umbra region, the thickness of the jaws in the FalseBEAM model could be decreased to a lower thickness than the specifications of the TrueBeam Monte Carlo data package in order to increase the out-of-field dose. However, this may affect agreement in the profile penumbra.

# Chapter 6

## Conclusion

FalseBEAM, a Monte Carlo TrueBeam 6 MV FFF model that is independent of the Varian phase space solution, has been created with source parameters that have been tuned to in-house measurements. To create FalseBEAM, the components above the jaws of an existing Varian CL21EX model were modified in order to match Varian TrueBeam phase space data defined at a plane above the jaws. The components below the phase space plane were modeled according to the Varian TrueBeam Monte Carlo data package. The source parameters were then tuned to in-house PTW microDiamond measurements following the method of Almberg et al [15].

In addition to FalseBEAM, another method of creating a TrueBeam Monte Carlo beam model was investigated by creating a BEAMnrc implementation of an existing PENELOPE TrueBeam model known as FakeBeam [32]. The PENELOPE FakeBeam model was shown to have excellent agreement in dose to water calculations with measurement [32]. However, as shown in section 5.1, directly reproducing the FakeBeam geometry in BEAMnrc does not give good agreement in dose to water. The reason for this disagreement comes from non-negligible differences between the PENELOPE and EGSnrc codes. In particular, the bremsstrahlung angular sampling algorithms are a possible source of the discrepancy. While it's possible that one could make small changes to the geometries in the BEAMnrc FakeBeam

model to mitigate the differences between Monte Carlo codes, particularly by modifying the brass filter, this method was abandoned in favour of the FalseBEAM model.

FalseBEAM could be extended to model other energies by repeating the process followed in this work. In principle, creating a 6 MV flattened model should only require substituting a cone-shaped flattening filter geometry in place of the flat brass filter used in the 6 MV flattening-filter-free FalseBEAM model. The dimensions of this flattening filter geometry would need to be tuned to match 6 MV TrueBeam phase space data. However, this straightforward solution is not guaranteed, because the rest of the components in the FalseBEAM model are not necessarily close to resembling the actual TrueBeam specifications.

The MLCs in the FalseBEAM model require validation before clinical use of MLC defined fields. In addition, further optimization would be needed for this work to be extended to the small fields used in stereotactic radiosurgery. Small field output factors are very sensitive to the choice of spot size, therefore FalseBEAM may require different source parameters in small fields [40].

In Chapter 2, detector effects were demonstrated to have a significant effect on dose to water measurements. For this reason, detector models were included in all dose to water simulations to include the effects of volume averaging and non-water equivalence of the detector materials.

In Chapter 3, the source parameters of a Varian CL21EX 6 MV flattened model were tuned to in-house PTW microLion measurements. This validated beam model was used as a starting point for the creation of FalseBEAM. Once the FalseBEAM parameters were tuned, the overall agreement in dose to water was excellent. FalseBEAM simulations that included a PTW microDiamond model for 5 x 5 cm<sup>2</sup>, 10 x 10 cm<sup>2</sup>, and 30 x 30 cm<sup>2</sup> PDDs were within 1.1%, 1.0%, and 1.8% with measurements beyond the first 3 mm. For 5 x 5 cm<sup>2</sup> and 30 x 30 cm<sup>2</sup> profiles, agreement was within 0.9% in the central region and within 5.2% in the penumbra region. The profile umbra was within 11.7% and 24.7% for the 5 x 5 cm<sup>2</sup> and 30 x 30 cm<sup>2</sup> fields, respectively. Relative to the maximum field dose, the umbra regions of all microDiamond profiles were within 1.9%.

All FalseBEAM PDDs and profiles agreed with measurements well within clinically recommended tolerances [3,17]: high-dose, low-gradient regions in PDDs and profiles were within 2% local percent difference, penumbra were within 3 mm distance-to-agreement, profile umbra were within 3% of the maximum dose, and the build-up region was within 20% local percent difference.

# References

- [1] International Atomic Energy Agency, *Radiation Oncology Physics: A Handbook for Teachers and Students*, E.B. Podgorsak, Ed. Vienna: IAEA, 2005.
- [2] R. Baskar, K.A. Lee, R. Yeo, and K.W. Yeoh, "Cancer and Radiation Therapy: Current Advances and Future Directions," *Int. J. Med. Sci.* **9**, 193-199 (2012).
- [3] B. Fraass et al., "American Association of Physicists in Medicine Radiation Therapy Committee Task Group 53: Quality assurance for clinical radiotherapy treatment planning," *Med. Phys.* **25**, 1773-1829 (1998).
- [4] A. Ahnesjö and M.M. Aspradakis, "Dose calculations for external photon beams in radiotherapy," *Phys. Med. Biol.* **44**, R99-R155 (1999).
- [5] D.W.O. Rogers, "Fifty years of Monte Carlo simulations for medical physics," *Phys. Med. Biol.* **51**, 287-301 (2006).
- [6] D.W.O. Rogers and A.F. Bielajew, *The Dosimetry of Ionizing Radiation*, B. Bjarngard, K. Kase, and F. Attix, Eds. New York: Academic, 1990, vol. III.
- [7] Indrin J. Chetty et al., "Report of the AAPM Task Group No. 105: Issues associated with clinical implementation of Monte Carlo-based photon and electron external beam treatment planning," American Association of Physicists in Medicine, 2007.
- [8] E. Soisson, A. Alexander, and J. Seuntjens, "OC-0468 Monte Carlo for Quality Assurance of dose calculation accuracy in seventy lung SBRT plans," *Radiotherapy and Oncology* **103**, S187-S188 May (2012).
- [9] B. Faddegon, C. M. Ma, and I. Chetty, "WE-B-213AB-03: AAPM TG-157: Commercial Implementation of Source Modeling and Beam Commissioning for Clinical Monte Carlo Dose Calculation," *Med. Phys.* **39**, 3941 (2012).
- [10] I. Kawrakow, E. Mainegra-Hing, D.W.O. Rogers, F. Tessier, and B.R.B. Walters, "NRCC Report PIRS-701: The EGSnrc Code System: Monte Carlo Simulation of Electron and Photon Transport," NRC, Ottawa, Canada, 2013.
- [11] F. Salvat, Fernández-Varea J.M., and J. Sempau, "PENELOPE—A Code System for Monte Carlo Simulation of Electron and Photon Transport," OECD Nuclear Energy Agency, 2011.
- [12] B.A. Faddegon, P O'Brien, and D.L. Mason, "The flatness of Siemens linear accelerator x-ray fields," *Med. Phys.* **26**, 220-228 (1999).
- [13] D. Sheikh-Bagheri and D.W.O. Rogers, "Sensitivity of megavoltage photon beam Monte Carlo simulations to electron beam and other parameters," *Med. Phys.* **29**, 379-390 (2002).

- [14] A. Tzedakis, J.E. Damilakis, M. Mazonakis, J. Stratakis, H. Varveris, and N. Gourtsoyiannis, "Influence of initial electron beam parameters on Monte Carlo calculated absorbed dose distributions for radiotherapy photon beams," *Med. Phys.* **31**, 907-913 (2004).
- [15] S. Almberg, J. Frengen, Kylling A., and T Lindmo, "Monte Carlo linear accelerator simulation of megavoltage photon beams: Independent determination of initial beam parameters," *Med. Phys.* **39**, 40-47 January (2012).
- [16] H. Bouchard, J. Seuntjens, J.F. Carrier, and I. Kawrakow, "Ionization chamber gradient effects in nonstandard beam configurations," *Med. Phys.* **36** (2009).
- [17] J.B. Smilowitz et al., "AAPM Medical Physics Practice Guideline 5.a.: Commissioning and QA of Treatment Planning Dose Calculations — Megavoltage Photon and Electron Beams," *Journal of Applied Clinical Medical Physics* **17**, no. 1 (2016).
- [18] Varian Medical Systems. (2013, February) Simulated Randomness: Varian's Monte Carlo Community Newsletter.
- [19] Omar Chibani and C.-M. Charlie Ma, "On the discrepancies between Monte Carlo dose calculations and measurements for the 18MV Varian photon beam," *Med. Phys.* **34**, 1206-1216 (2007).
- [20] Agostinelli S. et al., "Geant4—a simulation toolkit," *Nucl. Instrum. Meth. A* **506**, no. 3, 250-303 (2003).
- [21] M. Constantin et al., "Modeling the TrueBeam linac using a CAD to Geant4 geometry implementation: Dose and IAEA-compliant phase space calculations," *Med. Phys.* **38** (2011).
- [22] M Constantin, D Sawkey, and M Svatos, "SU-E-T-504: Electron Beam Tuning Methodology for TrueBeam Phase-Space Library Generation," *Med. Phys.* **40**, 321 (2013).
- [23] Z. Chang et al., "Commissioning and dosimetric characteristics of TrueBeam system: Composite data of three TrueBeam machines," *Med. Phys.* **39**, 6981-7018 (2012).
- [24] D. Sawkey et al., "SU-E-T-553: Measurement of electron spots on TrueBeam," *Med. Phys.* **40**, 332 (2013).
- [25] D. Sawkey, M. Constantin, and M. Svatos, "A Web Interface to Cloud-Based Treatment Head Simulations," *Med. Phys.* **40** (2013).
- [26] I. Kawrakow, D.W.O. Rogers, and B.R.B. Walters, "Large efficiency improvements in BEAMnrc using directional bremsstrahlung splitting," *Med. Phys.* **31**, 2883-2898 (2004).
- [27] J. Allison et al., "Geant4 electromagnetic physics for high statistic simulation of LHC experiments ," *Journal of Physics: Conference Series* **396**, 1-15 (2012).
- [28] B.R.B. Walters, D.W.O. Rogers, and I. Kawrakow, "History by history statistical estimators in the BEAM code system," *Med. Phys.* **29**, 2745-2752 (2002).
- [29] J. Sempau, A. Sanchez-Reyes, F. Salvat, H. Oulad ben Tahar, S. B. Jiang, and J. M. Fernández-Varea, "Monte Carlo simulation of electron beams from an accelerator head using PENELOPE," *Phys. Med. Biol.* **46**, 1163-1186 April (2001).

- [30] D.W.O. Rogers, B. Walters, and I. Kawrakow, "BEAMnrc Users Manual: NRCC Report PIRS-0509(A)revL," NRC, Ottawa, Canada, 2013.
- [31] B. Walters, I. Kawrakow, and D.W.O. Rogers, "NRCC Report PIRS-794revB: DOSXYZnrc Users Manual," Ionizing Radiation Standards National Research Council of Canada, Ottawa, Canada, 2013.
- [32] M. Rodriguez, J. Sempau, A. Fogliata, L. Cozzi, W. Sauerwein, and L. Brualla, "A geometrical model for the Monte Carlo simulation of the TrueBeam linac," *Phys. in Med. and Biol.* **60**, no. 11 (2015).
- [33] M. Rodriguez, J. Sempau, and L. Brualla, "PRIMO User's Manual," 2014.
- [34] I. Kawrakow, E. Mainegra-Hing, F. Tessier, and B.R.B. Walters, "The EGSnrc C++ class library, NRC Report PIRS-898 (rev A)," NRC, Ottawa, Canada, 2009.
- [35] J. Wulff, K. Zink, and I. Kawrakow, "Efficiency improvements for ion chamber calculations in high energy photon beams," *Med. Phys.* **35** (2008).
- [36] P.Z.Y. Liu, N. Suchowerska, and McKenzie D.R., "Can small field diode correction factors be applied universally?," *Radiotherapy and Oncology* **112**, 442-446 (2014).
- [37] A. Ralston, P. Liu, K. Warrenner, D. McKenzie, and N. Suchowerska, "Small field diode correction factors derived using an air core fibre optic scintillation dosimeter and EBT2 film," *Phys. Med. Biol.* **57** (2012).
- [38] E. Yorke et al., "Diode in Vivo Dosimetry for Patients Receiving External Beam Radiation Therapy. Report of Task Group 62.," American Association of Physicists in Medicine,.
- [39] C.D. Venanzio et al., "Characterization of a synthetic single crystal diamond Schottky diode for radiotherapy electron beam dosimetry," *Medical Physics* **40** (2013).
- [40] P. Papaconstadopoulos, F. Tessier, and J. Seuntjens, "On the correction, perturbation and modification of small field detectors in relative dosimetry," *Phys. Med. Biol.* **59**, 5937-5952 (2014).
- [41] R.M. Howell, S.B. Scarboro, S.F. Kry, and D.Z. Yaldo, "Accuracy of out-of-field dose calculations by a commercial treatment planning system," *Phys. Med. Biol.* **55**, no. 23, 6999-7008 (2010).
- [42] V. Panettieri, P. Barsoum, M. Westermark, Brualla L., and I. Lax, "AAA and PBC calculation accuracy in the surface build-up region in tangential beam treatments. Phantom and breast case study with the Monte Carlo code PENELOPE," *Radiotherapy and Oncology* **93**, 94-101 (2009).
- [43] E. Chung, S.D. Davis, and J. Seuntjens, "Experimental analysis of general ion recombination in a liquid-filled ionization chamber in high-energy photon beams," *Med. Phys.* **40** (2013).
- [44] F. Tessier and I. Kawrawkow, "Effective point of measurement of thimble ion chambers in megavoltage photon beams," *Med. Phys.* **37**, 96-107 January (2010).
- [45] M. Rodriguez, J. Sempau, and Brualla L., "PRIMO: A graphical environment for the Monte Carlo simulation of Varian and Elekta linacs," *Journal of Radiation Oncology, Biology, Physics* **189**, no. 10, 881-886 (2013).

- [46] M. Rodriguez, J. Sempau, and L. Brualla, "Technical Note: Study of the electron transport parameters used in PENELOPE for the Monte Carlo simulation of Linac targets," *Med. Phys.* **42**, 2877-2881 (2015).
- [47] M.J. Berger, *Monte Carlo calculation of the penetration and diffusion of fast charged particles*, B. Alder, S. Fernbach, and M. Rotenberg, Eds. New York, NY: Academic, 1963, vol. 1.
- [48] C.-M. Ma and D.W.O. Rogers, "NRCC Report PIRS-0509(C)revA: BEAMDP User's Manual," Ionizing Radiation Standards, National Research Council of Canada, Ottawa, Canada, 2013.
- [49] R. Capote et al., "Phase-Space Database for External Beam Radiotherapy: Summary Report of a Consultants' Meeting," IAEA INDC International Nuclear Data Committee, Vienna, Austria, 2006.